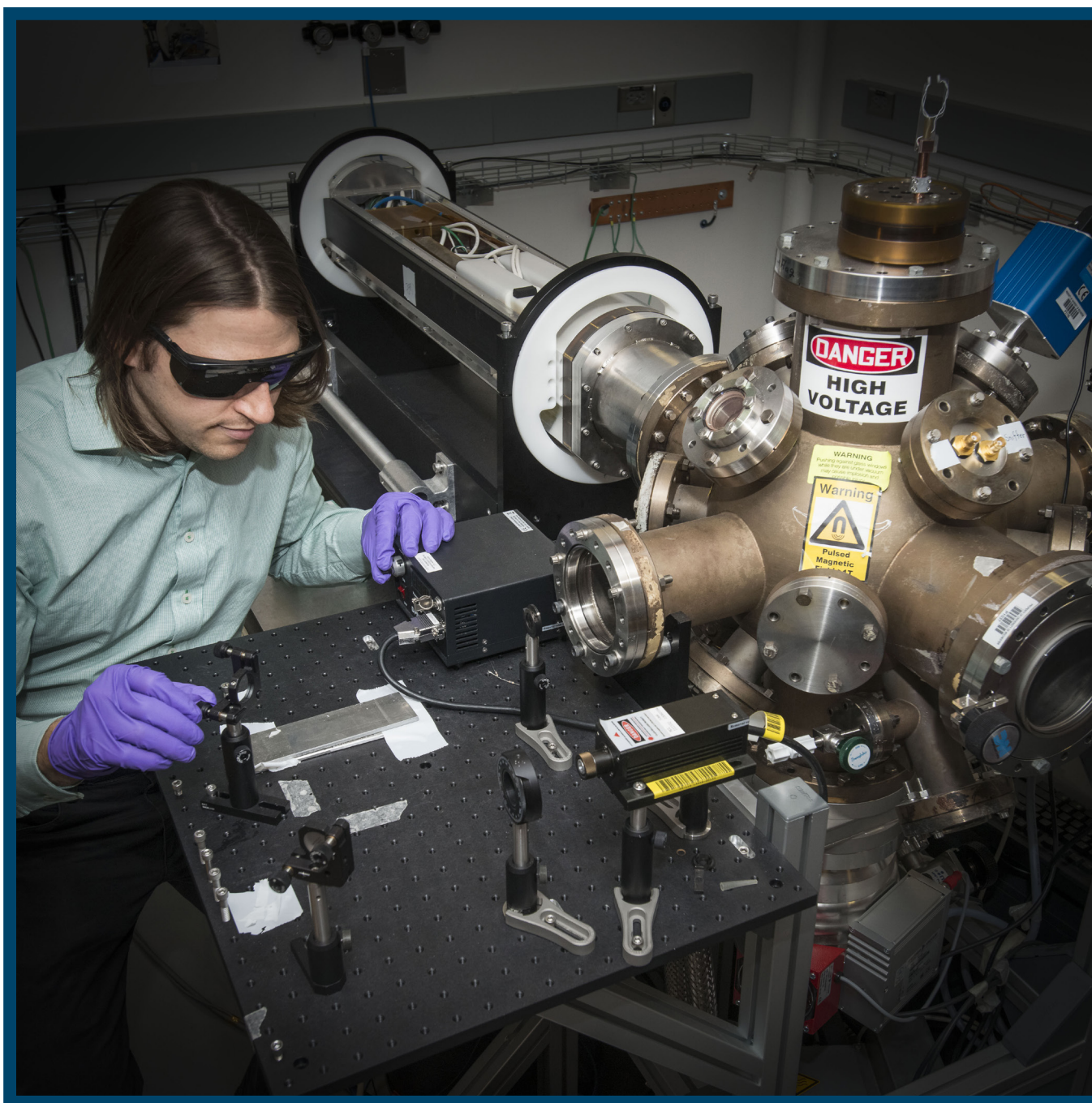


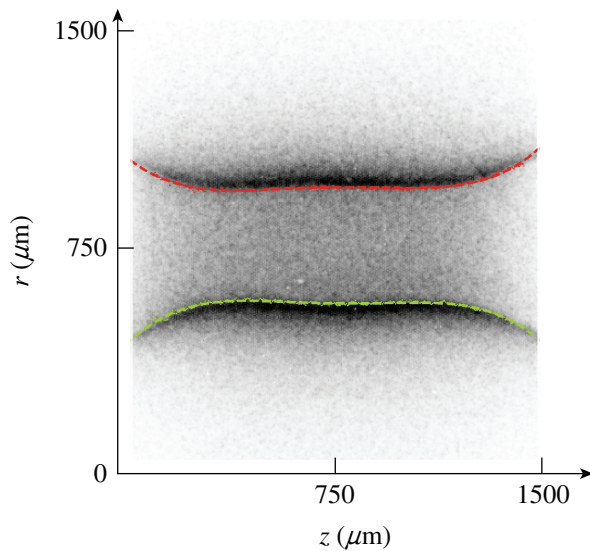
# LLE Review

## Quarterly Report



## About the Cover:

The photo on the cover shows graduate student Daniel Barnak working on the Faraday rotation system outside the vacuum chamber of the MIFEDS (magneto-inertial fusion electrical discharge system) laboratory, which is used to measure the magnetic field inside



TC13145JR

the wide variety of coils used in experiments with MIFEDS. The MIFEDS development unit (with the cover removed) can be seen in the background. Daniel reports on the development of a laser-driven MagLIF (magnetized liner inertial fusion) platform on OMEGA, which uses MIFEDS to provide an axial magnetic field in cylindrical implosions using laser-preheated fuel. The MagLIF fusion scheme was developed at Sandia National Laboratories, where the Z pulsed-power machine is used to implode a cylindrical target (liner) and the Z-Beamlet laser is used to preheat the fuel. MagLIF is now being considered by the National Nuclear Security Administration as one of three possible routes to fusion ignition in the laboratory, alongside indirect drive and spherical direct drive. OMEGA MagLIF experiments use targets that are  $10\times$  smaller in linear dimensions than Z targets and will provide the first experimental data on MagLIF scaling to test theories and simulations. The photo to the left shows an x-ray framing-camera image of a cylindrical implosion resulting from an experimental campaign to optimize axial uniformity.

This report was prepared as an account of work conducted by the Laboratory for Laser Energetics and sponsored by New York State Energy Research and Development Authority, the University of Rochester, the U.S. Department of Energy, and other agencies. Neither the above named sponsors nor any of their employees makes any warranty, expressed or implied, or assumes any legal liability or responsibility for the accuracy, completeness, or usefulness of any information, apparatus, product, or process disclosed, or represents that its use would not infringe privately owned rights. Reference herein to any specific commercial product, process, or service by trade name, mark, manufacturer, or otherwise, does not necessarily constitute or imply its endorsement, recommendation, or favoring

by the United States Government or any agency thereof or any other sponsor. Results reported in the LLE Review should not be taken as necessarily final results as they represent active research. The views and opinions of authors expressed herein do not necessarily state or reflect those of any of the above sponsoring entities.

The work described in this volume includes current research at the Laboratory for Laser Energetics, which is supported by New York State Energy Research and Development Authority, the University of Rochester, the U.S. Department of Energy Office of Inertial Confinement Fusion under Cooperative Agreement No. DE-NA0001944, and other agencies.

Printed in the United States of America

Available from

National Technical Information Services

U.S. Department of Commerce

5285 Port Royal Road

Springfield, VA 22161

Price codes: Printed Copy A04

Microfiche A01

For questions or comments, contact Jonathan Davies, Editor, Laboratory for Laser Energetics, 250 East River Road, Rochester, NY 14623-1299, (585) 273-4679.

Worldwide-Web Home Page: <http://www.lle.rochester.edu/>  
(Color online)

# LLE Review

## Quarterly Report



### Contents

In Brief .....	iii
Laser-Driven Magnetized Liner Inertial Fusion on OMEGA.....	55
Mitigation of Cross-Beam Energy Transfer in Symmetric Implosions on OMEGA Using Wavelength Detuning.....	61
Picosecond Time-Resolved Measurements of Dense Plasma Line Shifts .....	73
A Framed, 16-Image Kirkpatrick–Baez X-Ray Microscope .....	79
Modeling Tritium Interactions with Metals .....	87
Three-Dimensional Modeling of Neutron-Based Diagnostics to Infer Plasma Conditions in Cryogenic Inertial Confinement Fusion Implosions.....	100
Publications and Conference Presentations	



## In Brief

This volume of the LLE Review, covering January–March 2017, features “Laser-Driven Magnetized Liner Inertial Fusion on OMEGA” by D. H. Barnak, J. R. Davies, R. Betti, M. J. Bonino, E. M. Campbell, V. Yu. Glebov, D. R. Harding, J. P. Knauer, S. P. Regan, and A. B. Sefkow (LLE); A. J. Harvey-Thompson, K. J. Peterson, D. B. Sinars, S. A. Slutz, and M. R. Weis (SNL); and P.-Y. Chang (National Cheng Kung University). This article (p. 55) provides a brief overview of the development of a laser-driven MagLIF (magnetized liner inertial fusion) platform on the OMEGA laser. MagLIF was developed at the Z Pulsed Power Facility at Sandia National Laboratories and is a key target concept in the U.S. Inertial Confinement Fusion (ICF) Program. Laser-driven MagLIF on OMEGA is being developed to provide the first data on scaling and to allow for more shots with better diagnostic access than Z, facilitating basic physics studies.

Additional research highlights presented in this issue include the following:

- D. H. Edgell, R. K. Follett, I. V. Igumenshchev, J. F. Myatt, J. Shaw, and D. H. Froula consider mitigation of cross-beam energy transfer (CBET) in OMEGA direct-drive implosions by wavelength detuning the three separate legs of the system using a 3-D model (p. 61). CBET redistributes power from the ingoing central portion to the outgoing edge of OMEGA beams, increasing the root-mean-squared absorption nonuniformity by an order of magnitude and reducing total absorbed power. A wavelength shift of  $\pm 10 \text{ \AA}$  on two legs is found to be optimal for absorption and close to optimal for absorption uniformity.
- C. R. Stillman, P. M. Nilson, S. T. Ivancic, C. Mileham, I. A. Begishev, and D. H. Froula (LLE); and I. E. Golovkin (Prism Computational Sciences) report picosecond time-resolved measurements of the shift of the  $1s2p-1s^2$  line in He-like Al as a function of electron density (p. 73). Temperature and density are inferred from the Al  $\text{He}_\alpha$  complex using a nonlocal-thermodynamic-equilibrium model. The measurements are broadly consistent with an analytic line-shift model based on calculations of a self-consistent field ion-sphere model.
- F. J. Marshall, R. E. Bahr, V. N. Goncharov, V. Yu. Glebov, B. Peng, S. P. Regan, T. C. Sangster, and C. Stoeckl describe a 16-image Kirkpatrick–Baez–type x-ray microscope coupled to a high-speed framing camera (p. 79). A temporal resolution of  $\sim 30 \text{ ps}$  and a spatial resolution of  $\sim 6 \text{ }\mu\text{m}$  have been achieved. The new diagnostic has made it possible to accurately determine cryogenic implosion-core emission size and shape at the peak of stagnation, which has contributed to the determination of core pressures exceeding 50 Gbar.
- M. Sharpe and W. T. Shmayda present a model for tritium interaction with metals that treats a metal as a composite with a high-solubility surface layer bonded to a metal lattice (p. 87). Equilibrium is assumed so that the ratio of tritium concentration in the surface and in the lattice depends on the relative solubilities. The model can predict the temporal evolution of tritium concentration profiles during exposure to tritium gas, during storage and during successive decontamination efforts, and could be used to develop surfaces that are less prone to absorb tritium.

- F. Weilacher, P. B. Radha, and C. Forrest use 3-D modeling with the hydrodynamic code *HYDRA* and the neutron tracking code *IRIS3D* to interpret neutron emission measurements (p. 100). It is shown that background subtraction is important for inferring areal density from backscattered neutrons, but less important for forward-scattered neutrons, and is important for inferring ion temperature from DD neutrons, but is insignificant when inferring ion temperature from DT neutrons at the areal densities typical of OMEGA implosions. Asymmetries resulting in fluid flow in the core are shown to influence the absolute inferred ion temperatures from both reactions. Relative inferred temperatures reflect the underlying asymmetry of the implosion.

Jonathan R. Davies  
*Editor*

---

# Laser-Driven Magnetized Liner Inertial Fusion on OMEGA

## Introduction

Magnetized liner inertial fusion (MagLIF) is a concept that utilizes pulsed-power-driven Z pinches of metal liners to compress deuterium–tritium (DT) gas to fusion-relevant temperatures and pressures.<sup>1</sup> For cylindrical compression and pulsed-power time scales ( $\sim 100$  ns), it is required that the fuel be preheated to  $\sim 100$  eV and axially magnetized to suppress radial conduction losses to achieve near-adiabatic compression, reducing the radial convergence required to reach the temperatures and pressures needed for thermonuclear fusion. At stagnation, the axial magnetic field is compressed to the point where it is strong enough to magnetize alpha particles,<sup>2</sup> allowing self-heating to occur at low areal densities.

Cylindrical implosions can be achieved with 40 beams of the OMEGA Laser System, and in fact, magnetized cylindrical implosions have been carried out on OMEGA,<sup>3,4</sup> leaving only the laser preheating of the gas. A single beam has been redirected down a symmetry axis of OMEGA to heat the gas prior to compression.

MagLIF is being scaled down from a pulsed-power-driven device to a laser-driven device for several reasons: pulsed-power devices, like the Z machine at Sandia National Laboratories, are very violent environments in terms of debris and electromagnetic noise, making it very difficult to field diagnostics and maintain a high shot rate. Furthermore, diagnostic access around the target chamber in Z is limited by the installation of the axial magnetic field coils and the geometry of the current delivery system. OMEGA can perform roughly  $10\times$  more shots per day than Z and can provide better statistics and wider scans of the MagLIF parameter space. Furthermore, OMEGA has the capability to perform measurements that cannot be done on the Z machine, such as proton radiography of the compressed axial magnetic field, low-yield neutron measurements, and time-resolved x-ray measurements of the liner trajectory. Experiments at the OMEGA scale can provide another experimental data point for the energy scaling of the MagLIF concept and will ultimately give us the confidence in extrapolating MagLIF to ignition-scale designs.

This article is a brief overview of the work done to establish a science platform for studying the physics of MagLIF on OMEGA. Future more-detailed papers will describe the separate steps taken to achieve this goal. The following sections present (1) a review of 1-D magnetohydrodynamic (MHD) results that were used to design the platform; (2) preliminary results from experiments conducted to achieve the required preheat and uniform cylindrical compression; (3) the first results from a fully integrated MagLIF implosion on OMEGA; and (4) future projects to be explored using this recently established experimental platform.

## Point Design

The OMEGA point design<sup>5</sup> is energy scaled from the Z machine's 29-MA point design.<sup>1</sup> The conserved quantity is energy per unit volume, which mandates that the linear dimensions be scaled down by a factor of 10 to match the factor-of-1000 difference in driver energy between OMEGA and Z. Other factors such as fuel preheat and initial axial magnetic field can be the same. A higher implosion velocity will be needed at the OMEGA scale to compensate for increased thermal losses at the smaller scale. The preheat temperature, liner aspect ratio, and fuel density can be changed to achieve different implosion energetics for a complete scan of the MagLIF parameter space. An ensemble of 1-D MHD simulations that include electrothermal terms in Ohm's Law<sup>6</sup> was used to determine the optimal laser pulse length, taking into account the drop in on-target energy for pulses longer than 1 ns, and fuel density for shell thicknesses from  $20\ \mu\text{m}$  to  $50\ \mu\text{m}$  for a fixed 10-T initial axial magnetic field and 200-eV preheat temperature, the objective being to maximize neutron yield at a fuel convergence ratio close to the 25 chosen for the Z point design. Only a square-shaped laser pulse was considered. The optimal design for a  $30\text{-}\mu\text{m}$  shell is a 1.5-ns pulse length with an initial fuel density  $>1.5\ \text{mg}/\text{cm}^3$  as shown in Fig. 150.1. Thicker shells did not give adequate final fuel temperatures.

This optimal point is for a fixed magnetic field and preheat temperature, which is easily achievable. If the magnetic-field capabilities of OMEGA are expanded to values above 10 T,

the optimal point may change. Increasing magnetic field and preheat reduces convergence ratio and implosion speed, providing a more stable cylindrical implosion. Higher core pressures are achieved for higher magnetic fields because of the suppression of radial conduction losses (seen in Fig. 150.2). A higher preheat temperature leads to a lower final pressure for a fixed energy implosion, which is consistent with a simple model for adiabatic compression. For a given energy in a piston  $E$  and initial pressure  $P_0$  and volume  $V_0$ , the final pressure increase is

$$\frac{P_f}{P_0} = \left( \frac{E}{P_0 V_0} \right)^{\gamma / \gamma - 1} \quad (1)$$

and is therefore inversely proportional to the starting temperature for a fixed initial mass piston. Substituting this back into the energy balance equation and solving for the convergence ratio, we obtain

$$CR = \frac{R_0}{\sqrt{E/P_f \pi}}, \quad (2)$$

which is proportional to the final pressure or inversely proportional to the initial temperature. Higher starting temperatures, therefore, give a lower final pressure and lower convergence ratio, which is the trend highlighted in Fig. 150.2.

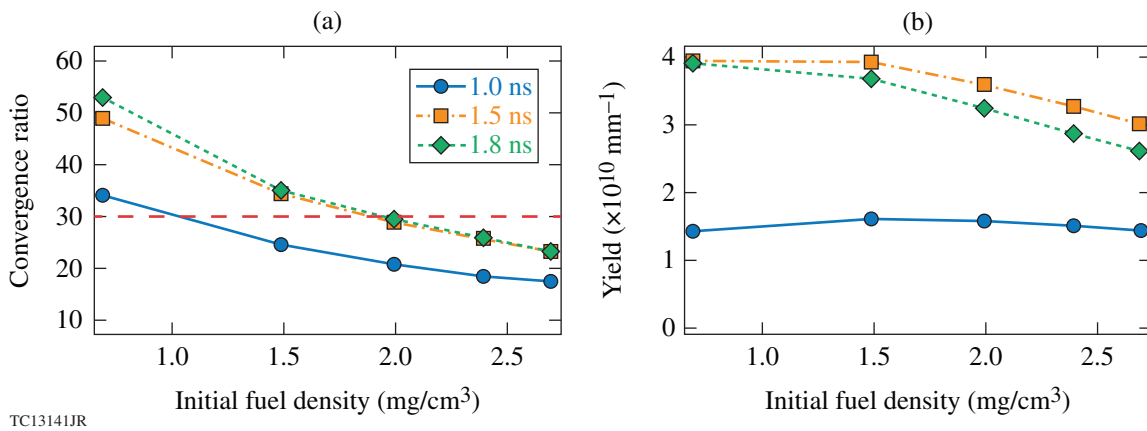


Figure 150.1

(a) The  $D_2$  fuel convergence ratio as a function of initial gas density for three different pulse lengths; (b) the neutron yields from each of these designs. These plots show that a 1.5-ns pulse is optimal and that the design requires an initial fuel density higher than that which optimizes neutron yield to maintain a fuel convergence ratio  $<30$ , indicated by the red dashed line.

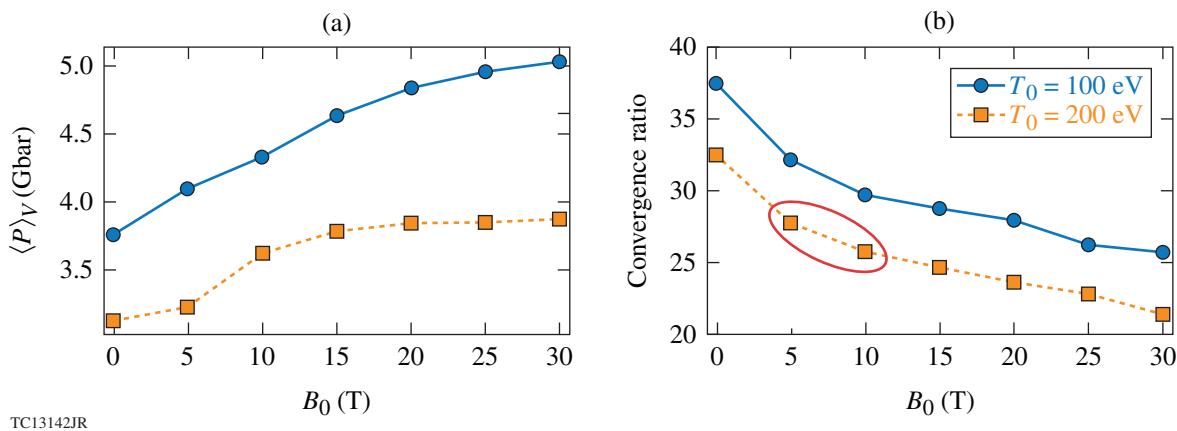


Figure 150.2

(a) As the magnetic field increases, the volume-averaged thermal pressure of the fuel increases, resulting in (b) a lower convergence ratio at the end of the implosion. This is mostly caused by the magnetic field suppressing radial conduction losses. The red circled region is the point design considering the capabilities of the OMEGA Laser System.

Regardless of the starting magnetic field or shell thickness, 1-D calculations show that a minimum preheat temperature of  $\sim 100$  eV is required for neutron yield increases larger than a factor of 2 from the magnetic field above the implosion-only baseline of  $\sim 10^{10}$  mm $^{-1}$ . Once above the threshold preheat, neutron yields and ion temperatures do not increase with initial temperature, but convergence ratio decreases, increasing the stability of the imploding shell. With a sufficient preheat temperature, increasing the initial magnetic field from 10 T to 30 T increases the neutron yield as shown in Fig. 150.3. Above 30 T, heat loss is ion diffusion dominated since radial electron conduction is essentially zero. Therefore, there is no further benefit from increasing the initial field. The magnetic field required to suppress ion heat flow introduces too much magnetic-field pressure, making it difficult to compress the target.

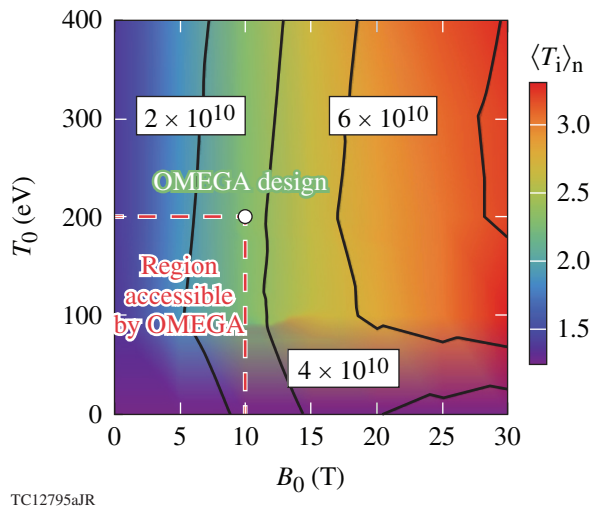


Figure 150.3 Neutron yields (contours) and neutron-averaged ion temperatures (colors) plotted as a function of initial axial magnetic field and preheat temperature. The region currently accessible by OMEGA is shown enclosed in the dashed lines.

### Preheat Experiments

The focused preheat experiments determined the laser entrance hole (LEH) window transmission, backscatter, and sidescatter; a gas-filled cylindrical target was illuminated with up to 200 J of  $3\omega$  light in a 2.5-ns square-shaped pulse to study gas preheating *in situ*. The beam was focused on the LEH window and a 200- $\mu$ m phase plate with smoothing by spectral dispersion and distributed polarization rotators were used. To study the window behavior in detail, window-only assemblies that consisted of the same 1.84- $\mu$ m-thick polyimide foils used for the gas cylinder targets were studied. Using calorimeters, Raman and Brillouin spectrometers in different ports around

the laser axis, soft x-ray emission from the LEH window and the gas, and optical emission from the surface of the gas-filled cylinder, we characterized the LEH window disassembly and the energy that propagates into the gas and determined a lower bound on the preheat temperature.

From the calorimeter measurements and backscatter diagnostics of the window-only shots, we determined that  $64.5 \pm 2.0\%$  of the laser energy incident on the LEH window is transmitted, with only  $0.72 \pm 0.22\%$  scattered outside of a  $28^\circ$  cone and  $0.59 \pm 0.16\%$  backscattered. It should be noted that the backscatter measurements herein are Brillouin measurements since the Raman measurement was below detectable threshold. We can then infer that  $34 \pm 2.0\%$  of the laser energy is absorbed in the window material as it disassembles. We have calculated the absorbed fraction using the 2-D hydrocodes *DRACO* and *FLASH*,<sup>7</sup> both of which give an absorbed energy of  $\sim 30\%$ . Furthermore, we can post-process the output from these hydrocodes to model the soft x-ray spectra of the LEH window disassembly. The results of this spectral analysis compared directly to measurements from an array of differentially filtered x-ray diodes are in good agreement, as illustrated in Fig. 150.4.

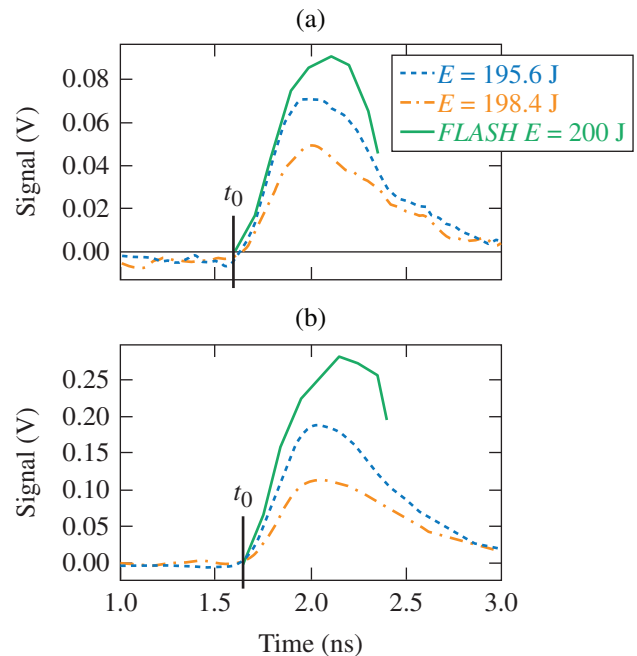


Figure 150.4 [(a), (b)] Two examples of the x-ray diode traces from experiments using a single laser beam and a laser entrance hole window assembly. The post-processed results from the *FLASH* hydrocode are in good agreement relative to the shot-to-shot variations.

Analysis of soft x rays from a diagnostic side window in the gas-filled cylindrical targets infer that a minimum possible gas temperature of 100 eV was achieved 1.3 ns into the laser pulse. This minimum value is determined from one shot, with other shots showing solutions above this minimum temperature. A parylene-AF4 fluorinated plastic cylinder was filled with 2-at. % neon-doped deuterium gas. The gas was then heated using the same laser beam that illuminated the LEH window assemblies. A side-on diagnostic window was imaged using a differentially filtered three-channel soft x-ray imager (SXR). Since the SXR is not absolutely calibrated and we have limited spectral information, the ratios of the spatially integrated channel signals are compared to a grid of possible temperatures and densities for the gas and the wall generated by a simulation. Comparing the channel ratios with this grid gives an infinite set of solutions, but if we constrain the solution space by insisting that the wall temperature cannot exceed the gas temperature, we establish the lowest possible value of the gas temperature to be 100 eV (shown in Fig. 150.5). Unfortunately, because of the limited dynamic range of the SXR and the quick increase in emission from increasing  $T_{\text{gas}}$ , temperatures above this 100-eV lower limit cannot be determined. We also obtain information about the gas heating from the x-ray diode array by looking at the LEH region. Much of the data is heavily encoded because of spectral integration, so we will rely primarily on comparison with hydrocodes to get a good idea of the heating process of the gas. A more-detailed paper on this experiment is expected to be submitted to Physics of Plasmas in the near future.

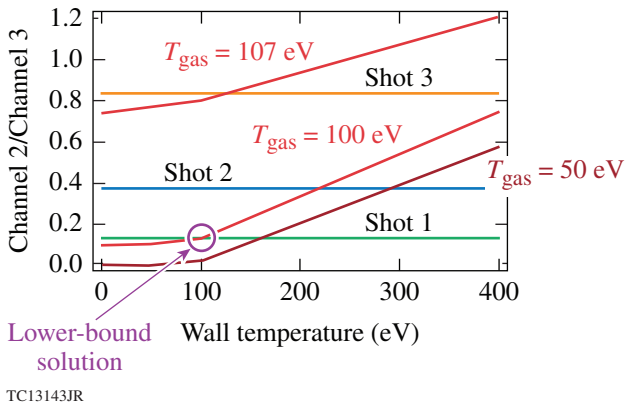


Figure 150.5 The ratio of Channel 2 to Channel 3 of the soft x-ray imager versus the wall temperature of the cylinder shows that the lower bound solution is 100 eV. Other solutions from different channel ratios either violate the condition of  $T_{\text{gas}} > T_{\text{wall}}$  or give higher values.

### Implosion Experiments

Implosion-only experiments were used to optimize the beam pointing and balance between normal and oblique beams; normal beams, referring to two rings of ten beams at an incidence angle of  $\pm 9^\circ$ , and oblique beams, referring to two rings of ten beams at an incidence angle of  $\pm 31^\circ$ . Both the separation and the intensity of the beams determine the uniformity and length of the cylindrical implosions. Using time-resolved x-ray images of the shell in flight, a shape can be determined by fitting the inner surface with a fourth-order polynomial function as shown in Fig. 150.6:

$$R(z) = a + b(z - z_0)^2 + c(z - z_0)^4. \quad (3)$$

The coefficients of this polynomial give a numerical measure that indicates if the shell has been overdriven at the ends or middle or uniformly imploded. Lineouts from time-integrated x-ray pinhole camera images also show the uniformity of the core and the length of the imploded region (as seen in Fig. 150.7). The illumination pattern that gives the most-uniform implosion empirically is an overlap of the oblique-angled beams at the center with the normal beams at the end and a reduction in energy of the normal beams to 83% of the maximum energy of the oblique beams. The result is the relatively uniform axial intensity profile shown in Fig. 150.8.

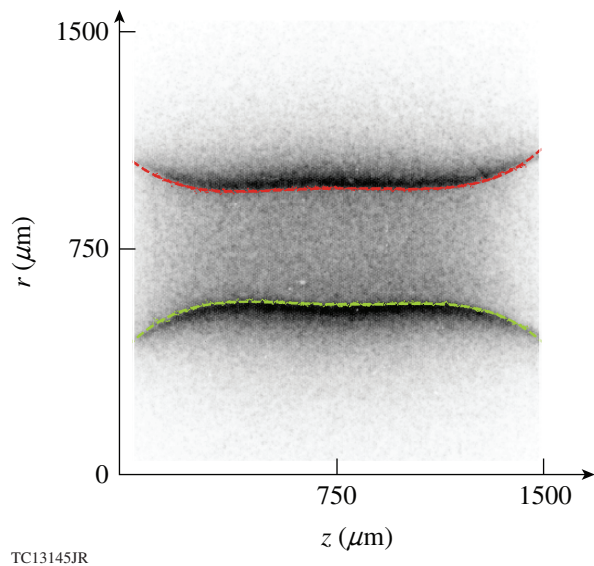
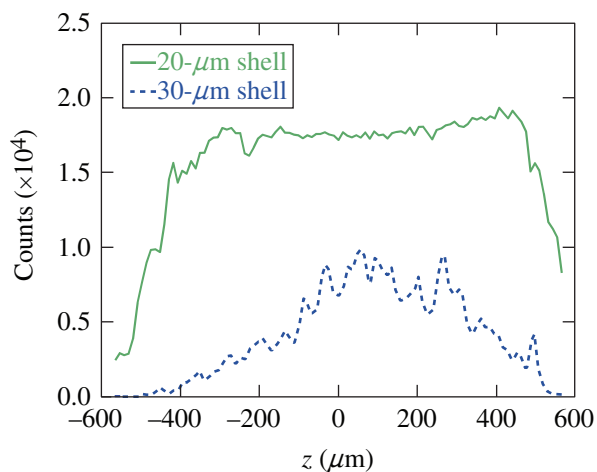
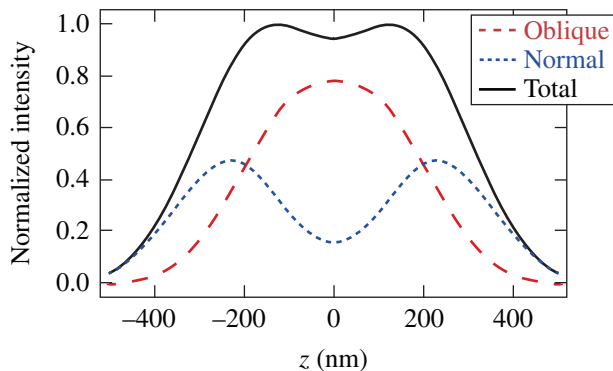


Figure 150.6 Each side of the shell was fit with a fourth-order polynomial to determine the shape of the shell in flight. The laser energy was then tuned to get the shape as flat as possible over the longest region.



TC13146JR

Figure 150.7  
Thinner shells that have faster implosion velocities give broader and flatter emission from the core. A raw lineout of charge-injection device counts plotted versus the axial position from a pinhole camera demonstrates this fact. This suggests that a faster implosion is needed at the OMEGA scale to mitigate increased thermal losses. Pinhole images also provide a second metric for implosion uniformity.



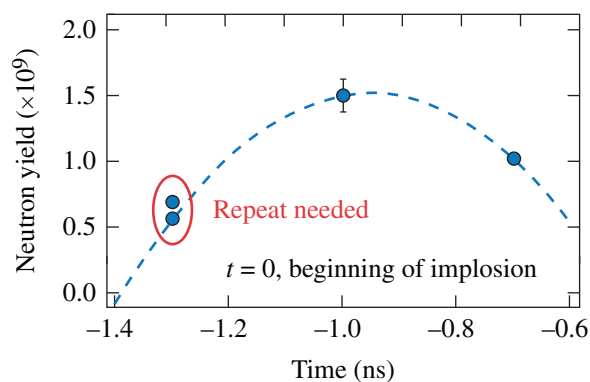
TC13144JR

Figure 150.8  
The irradiation pattern that gives the most cylindrically uniform compression.

### Integrated MagLIF Experiments

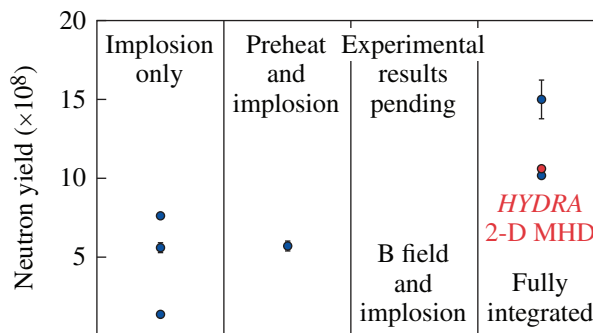
The first integrated MagLIF experiments on OMEGA were used to scan preheat beam timing relative to the drive beams. Simulations and experiments both indicate the optimal time to fire the preheat laser was  $\sim 1.0$  ns before the start of the drive beams, which corresponds to preheat finishing as the shell starts to implode. This made it possible for preheat to occur without introducing too much mix of wall material into the gas. Three times were scanned and the results can be seen in Fig. 150.9.

Yield enhancement from both preheat and magnetic field and preheat only matched with 1-D and 2-D simulation predictions based on the point design.<sup>5</sup> We have many shots with just the implosion from the beam-balancing campaign. In Fig. 150.10, the three best-quality implosion-only targets are shown along with a preheat and implosion shot, the two successful integrated MagLIF shots from the preheat beam-timing campaign, and the predicted performance of the point design from 2-D *HYDRA* MHD simulations. An implosion with magnetic field and no preheat has yet to be successfully completed. One- and two-dimensional MHD simulations replicating the implosion dynamics and magnetic-field compression are also under development. This is the first demonstration of yield enhancement in a magnetized cylindrical implosion



TC13147JR

Figure 150.9  
Neutron yield as a function of preheat beam time. The start of the drive beams is at  $t = 0$ . Some implosion beams were partially obstructed by the magnetic-field coils for both cases at the  $-1.3$ -ns timing, so these shots must be repeated, but the data follow the expected trend predicted by the simulations.



TC13148JR

Figure 150.10  
A summary of neutron yields for each configuration of the OMEGA MagLIF platform. Integrated MagLIF shots are compared to a 2-D magnetohydrodynamic (MHD) prediction made by the code *HYDRA*.

on OMEGA and is a very promising result that confirms the utility of laser-driven MagLIF in the development of a viable path toward ignition.

### Future Work

At the time of publication of this article, the first experiments that will probe the evolution of the axial magnetic field will have been performed. Understanding the dynamics of the magnetic field within the fuel is directly related to the confidence interval of yield predictions from MHD simulations. If the magnetic-field advection within the gas is poorly understood, yields can vary in simulation by whole orders of magnitude. The dominant contribution to magnetic-field advection within the gas is from the Nernst effect,<sup>8</sup> which is an additional advection velocity to the magnetic field proportional to the electron heat flow.<sup>9</sup> Therefore, the heat flow itself can push against the magnetic field, thereby negating any benefit of the reduced thermal conduction. Proton radiography of the implosion can provide a direct indication of the rate of this additional advection.

Experiments to explore the MagLIF parameter space are scheduled to occur over the next year. A magnetic-field scan will explore the dependence on the magnetic field and help us understand the scaling of the Nernst effect with the magnetic field. A scan of the initial fuel density will determine the highest achievable convergence ratio before a decrease in performance. Laser-driven MagLIF has the ability to use thinner shells with higher implosion velocities than pulsed-power-driven MagLIF because of ablative stabilization of the Rayleigh–Taylor instability. A scan will be made to determine the minimum shell thickness that can be imploded without a significant decrease in neutron yield.

### ACKNOWLEDGEMENT

The authors express their appreciation to the Mechanical Engineering Division of the Laboratory for Laser Energetics for the installation, characterization, and maintenance of the P9 3 $\omega$  laser, which provides the preheating capabilities for mini-MagLIF. We also acknowledge the entire Omega Laser Facility, which continues to be a great asset for achieving experimental configuration milestones. The information, data, or work presented herein was funded in part by the Advanced Research Projects Agency-Energy (ARPA-E), U.S. Department of Energy, under Award Number DE-AR0000568. The views and opinions of authors expressed herein do not necessarily state or reflect those of the United States Government or any agency thereof. This material is based upon work supported by the Department of Energy National Nuclear Security Administration under Award Number DE-NA0001944.

### REFERENCES

1. S. A. Slutz, M. C. Herrmann, R. A. Vesey, A. B. Sefkow, D. B. Sinars, D. C. Rovang, K. J. Peterson, and M. E. Cuneo, *Phys. Plasmas* **17**, 056303 (2010).
2. M. R. Gomez, S. A. Slutz, A. B. Sefkow, D. B. Sinars, K. D. Hahn, S. B. Hansen, E. C. Harding, P. F. Knapp, P. F. Schmit, C. A. Jennings, T. J. Awe, M. Geissel, D. C. Rovang, G. A. Chandler, G. W. Cooper, M. E. Cuneo, A. J. Harvey-Thompson, M. C. Herrmann, M. H. Hess, O. Johns, D. C. Lamppa, M. R. Martin, R. D. McBride, K. J. Peterson, J. L. Porter, G. K. Robertson, G. A. Rochau, C. L. Ruiz, M. E. Savage, I. C. Smith, W. A. Stygar, and R. A. Vesey, *Phys. Rev. Lett.* **113**, 155003 (2014).
3. J. P. Knauer, O. V. Gotchev, P. Y. Chang, D. D. Meyerhofer, O. Polomarov, R. Betti, J. A. Frenje, C. K. Li, M. J.-E. Manuel, R. D. Petrasso, J. R. Rygg, and F. H. Séguin, *Phys. Plasmas* **17**, 056318 (2010).
4. M. Hohenberger, P.-Y. Chang, G. Fiksel, J. P. Knauer, R. Betti, F. J. Marshall, D. D. Meyerhofer, F. H. Séguin, and R. D. Petrasso, *Phys. Plasmas* **19**, 056306 (2012).
5. J. R. Davies, D. H. Barnak, R. Betti, E. M. Campbell, P.-Y. Chang, A. B. Sefkow, K. J. Peterson, D. B. Sinars, and M. R. Weis, “Laser-Driven Magnetized Liner Inertial Fusion,” to be published in *Physics of Plasmas*.
6. J. R. Davies, R. Betti, P.-Y. Chang, and G. Fiksel, *Phys. Plasmas* **22**, 112703 (2015).
7. B. Fryxell *et al.*, *Astrophys. J. Suppl. Ser.* **131**, 273 (2000).
8. A. L. Velikovich, J. L. Giuliani, and S. T. Zalesak, in *2014 IEEE 41st International Conference on Plasma Sciences (ICOPS) held with 2014 IEEE International Conference on High-Power Particle Beams (BEAMS)* (IEEE, Washington, DC, 2014).
9. A. Nishiguchi *et al.*, *Phys. Rev. Lett.* **53**, 262 (1984).

# Mitigation of Cross-Beam Energy Transfer in Symmetric Implosions on OMEGA Using Wavelength Detuning

## Introduction

In the direct-drive<sup>1,2</sup> approach to inertial confinement fusion (ICF), laser beams directly illuminate a spherical target, depositing most of their energy in the coronal plasma. This energy is transported by electron thermal conduction through a conduction zone to higher densities, where ablation occurs. At the ablation surface, material rapidly expands, producing pressure that drives the shell of the target and thermonuclear fuel [usually deuterium–tritium (DT)] toward the center of the capsule, compressing the target to  $\sim 400 \text{ g/cm}^3$  (Ref. 2). To achieve this compression, the laser pulses are precisely shaped to launch a series of synchronized spherical shocks that cause the fuel to compress quasi-adiabatically. As the capsule converges, its kinetic energy is converted to internal energy, creating a hot dense core in which fusion reactions initiate, surrounded by a cold, dense, nearly Fermi-degenerate shell.<sup>1–3</sup>

Successful direct-drive ignition requires both efficient deposition of the laser energy in the coronal plasma and uniform target illumination to produce the spherically symmetric drive required to avoid hydrodynamic instabilities and low-mode-number asymmetries that can quench the implosion.<sup>4,5</sup> The target is illuminated by a number of beams, distributed symmetrically around the target, with diameters that are selected by the trade-off between increased drive uniformity and decreased drive efficiency as the laser spot size increases.<sup>6</sup> When neglecting laser–plasma instabilities, a laser focal-spot radius approximately equal to the target radius provides the best compromise.<sup>7</sup>

The total laser drive pressure and its uniformity can be significantly degraded by the transfer of energy between laser beams crossing in the coronal plasma.<sup>8–12</sup> Cross-beam energy transfer (CBET) is a three-wave process that occurs when the beat wave created by the interference between two electromagnetic waves resonantly excites a plasma ion-acoustic wave (IAW) as shown in Fig. 150.11. When two lasers with frequencies  $\omega_1, \omega_2$  and wave vectors  $\vec{k}_1, \vec{k}_2$  cross in a plasma, the ponderomotive force of their beat wave can drive a plasma density perturbation. These density perturbations form a grating and

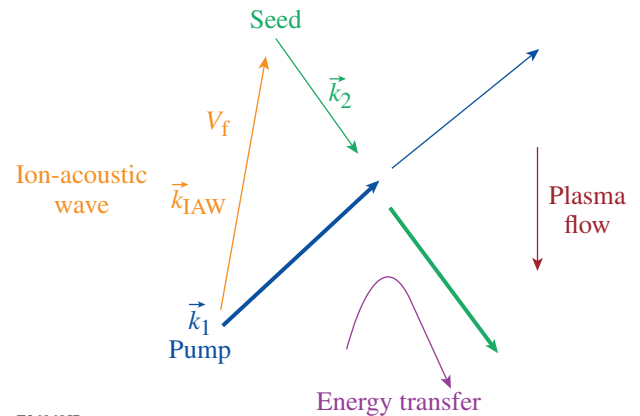
cause Bragg diffraction, facilitating the transfer via stimulated Brillouin scattering (SBS). The coupling is maximized when the driven wave satisfies the dispersion relation for the IAW:

$$\omega_{\text{IAW}} - \vec{u}_f \cdot \vec{k}_{\text{IAW}} = \pm c_s |k_{\text{IAW}}|,$$

$$\omega_{\text{IAW}} = \omega_1 - \omega_2, \quad (1)$$

$$\vec{k}_{\text{IAW}} = \vec{k}_1 - \vec{k}_2,$$

where  $\vec{u}_f$  is the local plasma hydrodynamic flow velocity,  $c_s$  is the local sound speed, and  $\omega_{\text{IAW}}$  and  $\vec{k}_{\text{IAW}}$  are the frequency and wave vector, respectively, of the ion-acoustic wave. The two branches ( $\pm c_s |k_{\text{IAW}}|$ ) of the dispersion relation correspond to the direction of power flow from the higher-frequency (in the plasma reference frame) “pump” wave to the lower-frequency “seed” wave. Since CBET is seeded by a laser beam rather than small-amplitude thermal noise, significant energy can be exchanged even when the SBS gain is small.



E26069JR

Figure 150.11  
A  $k$ -space diagram of cross-beam energy transfer (CBET). Energy is transferred from the pump beam to the seed beam as indicated by the magenta arrow labeled “Energy transfer.”

Experiments have demonstrated the existence of CBET between frequency-mismatched beams<sup>13</sup> and beams with the same frequency but crossing in a flowing plasma.<sup>14–18</sup> CBET has been modeled many times for a pair of crossing beams.<sup>19–22</sup> Indirect-drive hohlraum experiments at the National Ignition Facility (NIF)<sup>23</sup> have identified CBET as a mechanism responsible for transferring significant amounts of energy between laser beams.<sup>24</sup> In these experiments, the angle between crossing beams was small enough that steady-state CBET models could use a 3-D paraxial approximation or neglect small 3-D effects.

These models showed that significant CBET occurred between NIF beams when they were at the same wavelength and that energy was forward scattered from beams pointed toward the hohlraum equator to those directed nearer to the ends of the hohlraum, affecting the implosion symmetry on indirect-drive hohlraum experiments. It was also shown that CBET can distort the effective beam profile<sup>20</sup> even when the net transfer between beams is zero.<sup>25</sup> These models predicted that relatively small wavelength shifts (of the order of 1 Å) could tune the shape of an indirect-drive hohlraum implosion by transferring energy between beam rings. Independently varying the wavelength of the NIF beams to control CBET is now used as a tool to tune the implosion symmetry on the NIF<sup>25–29</sup> and to reduce stimulated Raman scattering (SRS) backscatter.<sup>27,30</sup> Recently, an in-line CBET model<sup>31,32</sup> was incorporated into the main 3-D radiation–hydrodynamics code, known as *HYDRA*,<sup>33</sup> for the NIF.

In direct drive, the presence of CBET was first inferred from the experimental observation of the scattered-light spectra<sup>34,35</sup> and the implosion velocity.<sup>36,37</sup> Early direct-drive CBET modeling typically used a 1-D linear geometry,<sup>10,38</sup> however, to properly model a direct-drive implosion, the crossings of many beams must be calculated simultaneously. The complex beam paths caused by refraction through the coronal plasma invalidate the paraxial approximation, and CBET models for direct-drive implosions typically use 3-D ray tracing to calculate the crossing beam trajectories. Initial CBET modeling suggested that in direct drive, CBET could backscatter energy out of ingoing rays from the hydrodynamically efficient small-impact parameter inner portion of the laser beam spot to outgoing large-impact parameter rays near the edge of the beam spot.<sup>34,39</sup> This would allow significant amounts of the incident energy from the central portion of the laser beams to bypass the highest absorption region near the critical surface, reducing the ablation pressure and hydrodynamic efficiency of the implosion. The redistribution of power modifies the effective beam profile identically for each beam in a symmetric implosion and

can have a large effect on a target’s illumination uniformity. The details and orientation of the redistribution depend on the 3-D positions of the beams with respect to each other and should be modeled in 3-D. In-line ray-based CBET models<sup>36,40,41</sup> have now been added to the direct-drive codes *LILAC* (1-D)<sup>42</sup> and *DRACO* (2-D),<sup>43</sup> which allow one to hydrodynamically self-consistently model CBET in direct-drive implosions. CBET redistributes ~30% of the incident energy on OMEGA at intensities of  $5 \times 10^{14}$  W/cm<sup>2</sup> and is responsible for a 10% to 20% reduction in laser absorption according to the *LILAC* model.<sup>36</sup>

Several different schemes have been proposed to mitigate CBET in direct-drive implosions, including doped ablaters,<sup>40</sup> narrow beams,<sup>36,44–46</sup> and multicolor lasers.<sup>36,40</sup> The predictions in direct drive that outgoing light from the edge of the beam was taking energy out of the incoming light from the beam center led to the proposal that shrinking the beam radius would reduce CBET.<sup>36</sup> Studies have shown that reducing the diameter of the laser beams by 30% can restore nearly all of the kinetic energy lost to CBET, but at a cost of increased low-mode perturbations.<sup>44</sup> Low-mode uniformity might be maintained by using two-state beam “zooming,” where the implosion is initiated using full-sized beams that are then reduced in radius after the corona has developed a sufficient conduction zone to smooth out perturbations.<sup>45</sup> Implementing zooming on OMEGA would require new phase plates, referred to as zooming phase plates (ZPP’s) and co-propagating dual driver lines.<sup>46</sup> Using laser beams with multiple wavelengths has been proposed to mitigate CBET in direct-drive implosions. Color-splitting the beams into two or more co-propagating wavelengths with  $\Delta\lambda > 5$  Å reduces CBET by ~50% in 1-D modeling.<sup>36,40</sup> Instead of each beam containing multiple wavelengths, the beams could be grouped into subsets of monochromatic beams with distinct wavelengths.<sup>47</sup> The current in-line models will not capture the full effect of the 3-D beam distribution because of their respective 1-D and 2-D approximations.

In this article, the effects of frequency detuning laser beams in direct-drive symmetric implosions are studied using a 3-D CBET model. To our knowledge, this is the first fully 3-D modeling of CBET for direct-drive implosions. The 3-D ray-based CBET model was benchmarked against full-field calculations,<sup>48</sup> providing confidence in the implementation of the model to calculate the effects of CBET in full-scale implosion experiments. These calculations show that interactions between beams with relative angles between 45° and 90° are the most significant for CBET in OMEGA direct-drive implosions. Redistribution of laser power because of CBET can increase the rms (root mean square) absorption nonuniformity by an order

of magnitude. Shifting the relative wavelengths of three groups of laser beams by  $\sim 10 \text{ \AA}$  maximized the total absorption, and the rms absorption nonuniformity was near minimum for the implosion conditions studied in this article.

The following sections discuss the model equations and gridding; report on model results for two-beam and many-beam CBET coupling when all the beams are launched with the same wavelength; and present predictions for a CBET mitigation scheme in 60-beam symmetric OMEGA direct-drive implosions using wavelength detuning.

### The 3-D CBET Model

The CBET model used here (*BeamCrosser*) was originally developed as a *MATLAB*<sup>49</sup>-based hydrodynamics code post-processor to simulate scattered-light spectra from OMEGA implosions<sup>50</sup> and provided the first evidence that CBET was significantly degrading implosion performance relative to 1-D hydrodynamic predictions.<sup>34,39</sup> As a hydrodynamics code postprocessor, the CBET model relies on time-varying coronal plasma parameters calculated independently by a hydrodynamics code such as *LILAC* (1-D) or *DRACO* (2-D). The CBET model is used to gain insight into 3-D effects during an implosion, even though its calculations are not fully self-consistent with the plasma hydrodynamics.

#### 1. Ray Tracing and Model Gridding

The model is a ray-based CBET model and therefore does not solve the full electromagnetic Maxwell equations. The reduced ray equation for geometric optics<sup>51</sup> is used to determine the laser beam propagation through the coronal plasma of an implosion. The ray equation is solved by a fourth-order Runge–Kutta method similar to that of Sharma *et al.*<sup>52</sup>

A single geometric optics-based ray is simply a path through space that by itself carries no inherent information about the local light intensity. The laser intensity along a ray is calculated using the intensity law of geometrical optics<sup>51</sup> and the spacing between points of neighboring rays on the same wavefront (having equal optical path lengths) along with the change in intensity caused by absorption and CBET, as discussed in the next section.

An example of the ray paths for a single laser beam propagating through a spherically symmetric coronal plasma of a direct-drive implosion is shown in Fig. 150.11. Refraction of the rays produces a paraboloid-like shadow behind the target inside of which rays cannot reach. The envelope of tangential rays defining the boundary surface of the shadow volume is a

caustic<sup>53</sup> of the “fold catastrophe” type,<sup>54</sup> where rays fold upon themselves and all points on the unshadowed side of the caustic are intersected by two distinct rays. The points where the rays graze the caustic are sometimes referred to as their “turning points,”<sup>53</sup> but that is not true in general. The turning point is best defined as the point of deepest radial penetration into the coronal plasma. It is clear from the outermost rays shown in Fig. 150.12 that these rays cross well away from their closest approach to the target. The intensity law of geometrical optics breaks down near the caustic, where the spacing between points on the same wavefront becomes very small, giving unphysically high intensities. The actual intensity where two rays cross is limited by diffraction. The intensity near the caustic is similar to an Airy pattern superimposed on the intensity from the geometric law. The CBET model limits the intensity along the rays from reaching unphysically high intensities by using either a fixed limiting factor or a field swelling limit based on Krueer,<sup>48,55</sup> however, this limit has only a small effect on the results of the code since it is applied only in a small volume.

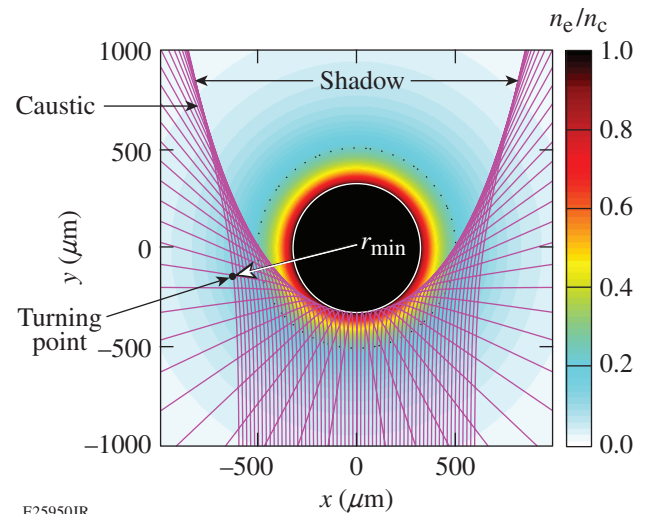


Figure 150.12  
Ray tracing of a laser beam through a spherical plasma.

The change in local laser frequency along the ray path resulting from changing plasma conditions is calculated from the difference in flight times of successive wavefronts:<sup>56</sup>

$$\Delta\omega = \omega_L \frac{\partial\tau}{\partial t}, \quad (2)$$

where  $\omega_L$  is the initial laser vacuum frequency and  $\tau$  is flight time of the light along the ray. The rate of change in flight time is directly calculable along a ray using the local rate of change in plasma density along each ray path. Calculating this general-

ized Doppler effect is essential because the change in frequency between incoming and outgoing rays in a typical direct-drive implosion is of the same order as the difference in the frequency needed for CBET (approximately a few angstroms).

The model “gridding” follows the beam trajectories determined by the ray trace. Each on-target laser beam profile is discretized into many square “beamlets” with flat intensities on a 2-D grid, as shown in Fig. 150.13(a). The distance along the path of each beamlet provides the third dimension for the gridding of each beam. Figure 150.13(b) shows this non-orthogonal overlapping grid in which more than one cell for a single beam can occupy the same physical space. CBET at these intrabeam crossings between beamlets from the same beam is calculated by the model in addition to crossing between beamlets from different beams. The significant refraction of the laser light in a direct-drive implosion plasma is a major difference from indirect drive, where the refraction of the laser beams can typically be ignored<sup>26</sup> and the paraxial approximation can be employed<sup>25</sup> in the volume where the beams cross.

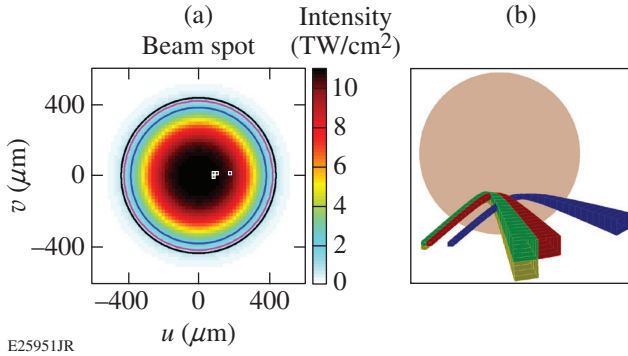


Figure 150.13

(a) Laser beam discretization into beamlets for an OMEGA beam with SG4 phase plates. The magenta circle is the nominal beam radius (contour containing 95% of the beam energy); (b) 3-D gridlines of four sample beamlets corresponding to the same-colored squares in (a).

## 2. CBET Theory and Equations

The CBET equations used in the model are a 3-D extension of the quasi-steady-state 1-D slab fluid model of Randall *et al.*,<sup>38</sup> which assumes that where two rays cross, they can be treated locally as plane waves. To facilitate conservation of energy, the equations are written in terms of power rather than intensity.

The total power in a beamlet  $P_b$  along its path ( $s$ ) is followed by the model as

$$dP_b(s) = P_b(s) \left( \frac{1}{L_{\text{abs}}} + \sum_{\text{all beam crossings}} \frac{C_{\text{CBET}}}{L_{\text{CBET}}} \right) ds, \quad (3)$$

where  $L_{\text{abs}}$  is the scale length of inverse bremsstrahlung absorption.<sup>57</sup>  $C_{\text{CBET}}$  is a multiplier, typically of the order of 2 for implosion modeling,<sup>58</sup> applied to the calculated CBET coupling to better match experimental measurements (discussed in detail below).  $L_{\text{CBET}}$  is the local spatial rate of energy gain/loss because of CBET in the strong damping limit:<sup>36,38,59</sup>

$$L_{\text{CBET}}^{-1} = 5.85 \times 10^{-2} \frac{1}{\nu_a} \frac{n_e/n_c}{(1-n_e/n_c)} \times \frac{I_{14} \lambda_{0,\mu\text{m}}}{T_{e,\text{keV}} (1 + 3T_{i,\text{keV}}/ZT_{e,\text{keV}})} \times \psi \times R(\eta) (\mu\text{m}^{-1}), \quad (4)$$

where  $\lambda_{0,\mu\text{m}}$  is the laser wavelength in microns,  $I_{14}$  is the crossing laser intensity in  $10^{14}$  W/cm<sup>2</sup>,  $T_{e,\text{keV}}$  and  $T_{i,\text{keV}}$  are the electron and ion temperatures, respectively, in keV,  $Z$  is the average ionization,  $\nu_a$  is the dimensionless amplitude damping rate for the IAW,  $n_e$  is the electron density, and  $n_c$  is the critical density. Since  $L_{\text{CBET}}$  depends on the intensity of the crossing beamlets, Eqs. (3) and (4) form a set of coupled nonlinear equations.

The factor  $R(\eta)$  is the resonance function accounting for how closely the driven wave satisfies the IAW dispersion relation [Eq. (1)],

$$R(\eta) = \frac{\nu_a^2 \eta}{(\eta^2 - 1)^2 + \nu_a^2 \eta^2}, \quad (5)$$

$$\eta = (\vec{k}_{\text{IAW}} \cdot \vec{u}_i - \omega_{\text{IAW}}) / k_{\text{IAW}} c_s.$$

The factor  $\psi$  accounts for the effect of polarization on the coupling of the crossing beams. For random polarization or when the beams have their polarization evenly distributed in two orthogonal components,

$$\psi = \frac{1}{4} (1 + \cos^2 \theta_k), \quad (6)$$

where  $\theta_k$  is the beam crossing angle.<sup>60</sup> This is appropriate for most implosions on OMEGA, where distributed polarization rotators (DPR's)<sup>61</sup> are used to split the beams into orthogonal polarizations, or on the NIF, where the beams are arranged in quads in such a way that the polarizations of two beams are orthogonal to the polarization of the other two beams in the quad.<sup>60</sup> When DPR's are not used on OMEGA, the beams are linearly polarized and the coupling between the beams affects only the shared polarization component.<sup>62</sup>

As mentioned above, outside the beam shadow, all points are crossed twice by rays from each beam, so there are a total of  $2N-1$  possible crossings to be considered at each point along a beamlet, where  $N$  is the total number of beams. Equations (4)–(6) are applied to all beamlet crossings to determine the total CBET coupling at each grid point along all beamlets. Since pump depletion is inherent in CBET, the system is solved using fixed-point iteration. Energy is conserved by balancing the power exchanged between beamlets such that the power gain (loss) calculated for beamlet A where it is crossed by beamlet B is identical to the power loss (gain) for beamlet B where it is crossed by beamlet A.

### 3. Benchmarking the Model

The CBET model was benchmarked by comparing it with the predictions of a full-wave code *LPSE* (laser-plasma simulation environment).<sup>48</sup> *LPSE* solves the time-enveloped Maxwell equations coupled to a linearized time-dependent fluid plasma response to calculate the enveloped electric-field vector and the ponderomotively driven ion-density perturbations. *LPSE* is impractical for full-scale 3-D implosion modeling because of its computational costs, but full-scale 2-D and reduced-scale 3-D runs provide good benchmarks for a ray-based model.

Figure 150.14 shows an *LPSE* calculation of two lasers crossing in a constant-density plasma with a linearly varying plasma velocity profile that places the maximum of the resonance function [Eq. (2)] at  $x = 8.6 \mu\text{m}$ . Both beams are polarized  $45^\circ$  out of the plane. CBET affects only the components of the polarization that are shared by the beams, so the polarization of each beam is expected to rotate. The intensities of the beams after undergoing CBET predicted by the ray-based model (with  $C_{\text{CBET}} = 1$ ) are an excellent match to those predicted by *LPSE* [Fig. 150.14(b)]. The predicted rotation in the polarization caused by CBET is very good over the region where the beam power is significant, but some divergence between the calculations is observed where the beam intensities are small. Overall, the comparison with the full-field calculations of *LPSE* provides confidence on the validity of the approximations made in the ray-based code.

In direct-drive implosions, experimental measurements of the ablation rate and the ablation-front trajectory on both OMEGA and the NIF are in good agreement with *DRACO* predictions provided a CBET gain multiplier of  $C_{\text{CBET}} = 2$  is used.<sup>58</sup> A similar factor of  $C_{\text{CBET}} = 2$  is required by the CBET model described here in order for its scattered-light predictions to match observations. This indicates that some physics pres-

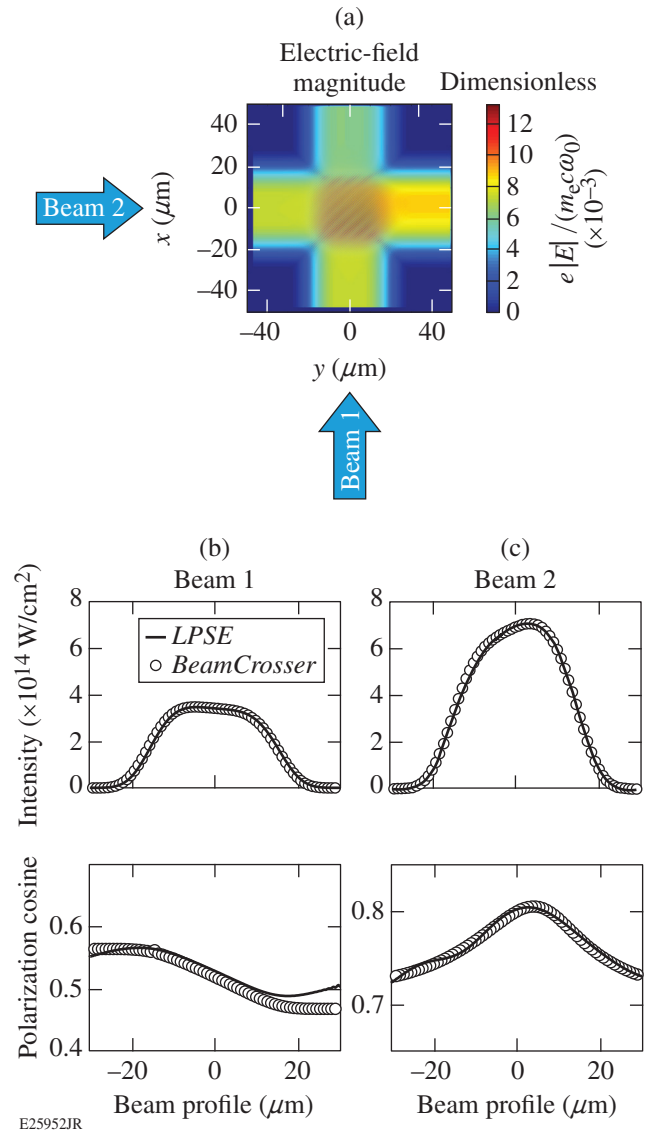


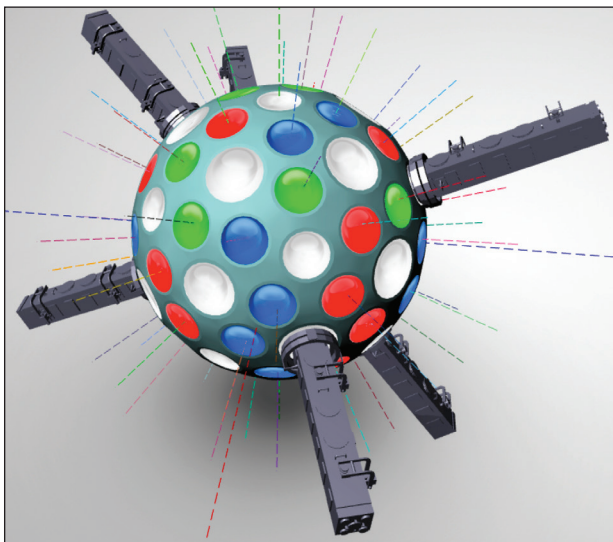
Figure 150.14 Laser-plasma simulation environment (*LPSE*) benchmarking: (a) *LPSE* simulation of the electric-field magnitude for two beams, both initially polarized  $45^\circ$  out of the plane, crossing in a plasma; (b) intensity profiles of the beams leaving the plasma for *LPSE* (solid curve) and *BeamCrossover* (circles); and (c) polarization cosine (where 0 is  $s$  polarized and 1 is  $p$  polarized) for the beams leaving the plasma from *LPSE* (solid curve) and *BeamCrossover* (circles) modeling.

ent in direct-drive implosions are missing from the ray-based models. Possible candidates for the missing phenomena include diffraction, polarization details, and nonlinear multibeam effects. All predictions presented here, unless mentioned otherwise, use a factor of  $C_{\text{CBET}} = 2$ .

### Beam Coupling with No Wavelength Shift

In this section, the coupling between OMEGA beams during a direct-drive implosion is modeled when all beams are launched with the same wavelength (351 nm). It is important to note that although all beamlets enter the plasma with the same wavelength, the Doppler effect<sup>56</sup> changes the wavelength of each beamlet as it passes through the plasma. This wavelength shift varies across the beam profile depending on the path each beamlet takes through the coronal plasma. The magnitude of the Doppler shift is of the order of a few angstroms and must be included when calculating the CBET coupling along a beamlet.

All of the simulations use 1-D *LILAC* predictions with a nonlocal electron heat transport model of the coronal plasma conditions for a typical OMEGA symmetric direct-drive implosion of a CH target (shot 60,000). The plasma profiles were taken from a single time late in the pulse when CBET is predicted to be largest. Figure 150.15 shows the distribution of the 60 OMEGA laser beams. All beams use a super-Gaussian of the order of 4 (SG4) intensity profile measured for the SG4 distributed phase plates (DPP's) used in the implosion. All beams entered the



E26062JR

Figure 150.15

View of the OMEGA three-leg geometry: the beams fed by each of the three different beamline legs are shown in three different colors (red, green, and blue).

plasma with 0.35 TW of power, which was the nominal power of all the beams in the implosion late in the pulse.

### 1. Two-Beam CBET Calculations

In a direct-drive implosion, each beam can interact with all other beams. In a nominally symmetric implosion, all beams have identical beam powers, intensity profiles, and relative geometries (i.e., the “view” from each beam looks the same with respect to the relative positions of the other beams). There is zero net exchange of total power between the beams, but there will still be a redistribution of power because of CBET. It is useful to determine which of the other beams has the strongest exchange with any single beam and the effect of that exchange on the effective beam intensity profile. How CBET affects the exchange between any two specific pairs of beams is mainly dependent on the angle between the two beams.

Figure 150.16 shows the laser absorption for two-beam simulations, where the angle  $\theta$  between the beams was varied;  $\theta = 180^\circ$  indicates beams launched on opposing sides of the target. Because the coupling of any two beams is small compared to the total interaction between a set of 60 beams in an OMEGA symmetric implosion, a CBET multiplier of  $C_{\text{CBET}} = 5$  was used for these two-beam interactions to accentuate the effects of CBET. The degradation in absorbed power is caused by redistribution of the beam power and is identical for both beams because of symmetry. The absorbed power is degraded most strongly by beams that are separated by  $45^\circ$  to  $90^\circ$ . Beams separated by more than  $135^\circ$  are practically decoupled. The absorption for these nearly opposite beams is essentially the same as when only intrabeam CBET interaction between a single beam and itself is considered. For  $0^\circ$  the beams are co-propagating and the laser absorption is the same as the intrabeam CBET of a single beam with twice the intensity. Figure 150.16(b) shows the effective importance of CBET between beams at different angles. The effective importance in a direct-drive implosion depends on the number of beams at that angle. For an infinite number of beams, the importance of CBET for beams at a specific angle is determined by the change in absorption of the beam from Fig. 150.16(a) weighted by the differential surface area of a sphere for that angle ( $\sin\theta \cdot d\theta$ ). The normalized change in absorption because of CBET weighted by  $\sin\theta$  is shown by the solid red line in Fig. 150.16(b). Compared to Fig. 150.16(a), the importance of different beams is skewed toward the equator where the differential area is maximum. For a finite set of beams, the effect of CBET from one beam at a specific angle is weighted by the actual number of beams at that angle. The importance of different beams weighted for the symmetric 60-beam OMEGA geometry is shown by the

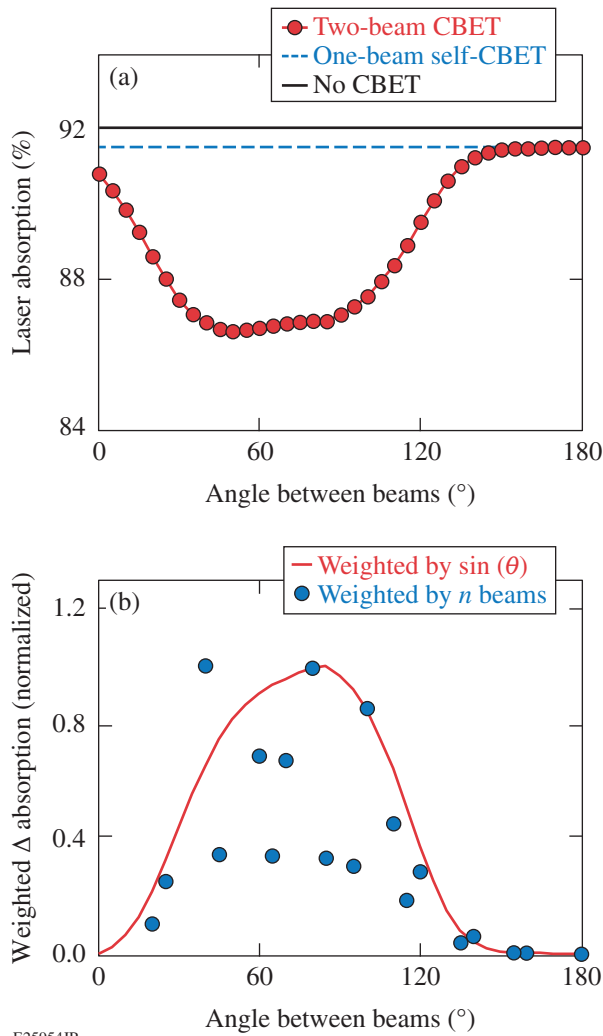


Figure 150.16  
 (a) Percent of laser power absorbed for two laser beams incident on an OMEGA symmetric implosion coronal plasma versus the angle between the launched beams. The black solid line is the laser absorption without CBET. The blue dashed line is the single-beam laser absorption with CBET calculated for intrabeam exchanges. (b) The change in absorption because of CBET weighted by the target surface area (red solid curve) and by the actual number of beams at specific angles for OMEGA (circles binned in 5° groups).

solid circles in Fig. 150.16(b). The largest effective change in absorption on OMEGA occurs from beams around 40°, 80°, and 100°.

Figure 150.17 shows the redistribution of power in the beam profile for two laser beams at a relative angle of 90°. Although CBET was known to shift the centroid of the outgoing beam profiles for simple beam geometries,<sup>20,25</sup> the redistribution is complicated for beams refracting through a spherical plasma where not all beamlets encounter a resonance with the other beam. Figure 150.17(a) shows the power gain and loss

because of CBET integrated along the path of each beamlet (as described in **Ray Tracing and Model Gridding**, p. 63). The beamlets near the horizontal axis experience a net loss and those on the beam edge closest to the other beam experience a net gain. The total absorbed power in each beamlet is shown in Fig. 150.17(b). Near the beam center there is a region of lower absorbed power caused by the CBET losses. The overall absorption profile is radially asymmetric, and there is a shift in the centroid of the absorption away from the other beam compared to the no-CBET absorption profile [Fig. 150.17(c)].

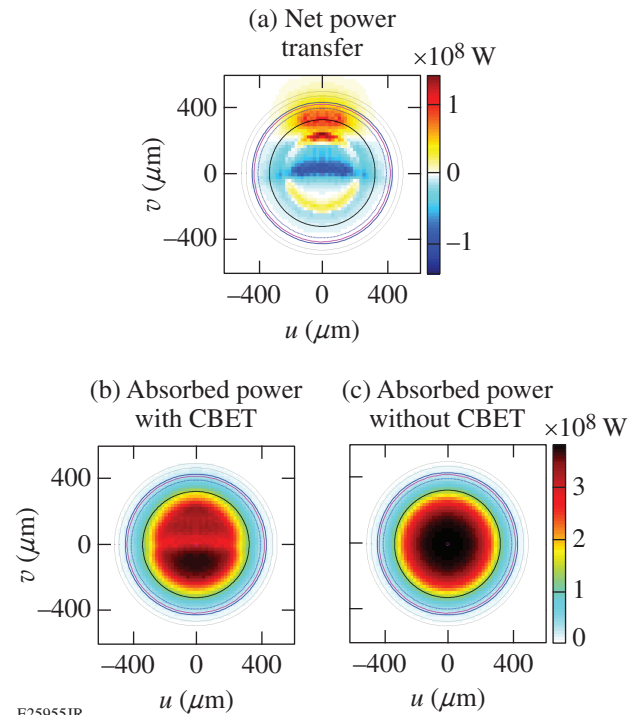


Figure 150.17  
 Beam profiles for the case of two beams at 90°. Profiles are oriented such that “up” is the directions of the other beam; i.e., the beamlets on the positive  $u$  direction are those that refract directly toward the other beam. (a) Power exchange caused by CBET summed along the full path of each beamlet. Red indicates a net gain while blue is a net loss. (b) Absorbed power summed along the full path of each beamlet; (c) absorbed power along the full path of each beamlet without CBET.

## 2. 60-beam CBET

Figure 150.18 shows the CBET exchange and absorption profiles calculated for the coronal plasma conditions modeled with the full 60 beams on OMEGA. In a direct-drive implosion, CBET’s total effect on a beam is the sum of its interactions with all other beams. The absorbed power is significantly less in magnitude and shows a more-complicated profile structure than the two-beam case. As in the two-beam case, there is

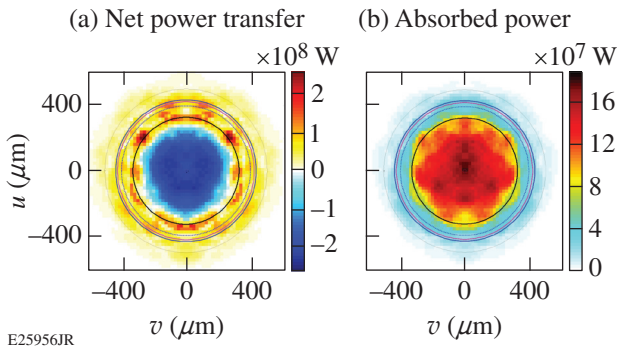


Figure 15.18  
 Beam profiles for CBET in the 60-beam OMEGA geometry. Profiles are oriented in such a way that “up” is the direction of the nearest-neighbor beam. (a) Power transfer because of CBET integrated along the path of each beamlet; (b) absorbed power integrated along the path of each beamlet.

no net exchange in power between beams because of beam symmetry but there is significant redistribution of power. The effect of many beams extends the ingoing losses over the hydrodynamically efficient small impact parameter beamlets and distributes the net outgoing gain to a ring of less hydrodynamically efficient high-impact parameter beamlets. The change in the absorbed power profile from the single-beam, no-CBET profile [Fig. 15.16(c)] has a significant effect on the absorption uniformity over the target surface.

Figure 15.19 shows an absorption surface map calculated by radially integrating the 3-D absorption at all points over the target surface. When CBET is ignored, the absorption is very uniform with an rms variation of  $\sim 0.2\%$ . When CBET is included, the nonuniformity is an order-of-magnitude larger with an rms of 2.0%. Since there is no azimuthal symmetry in

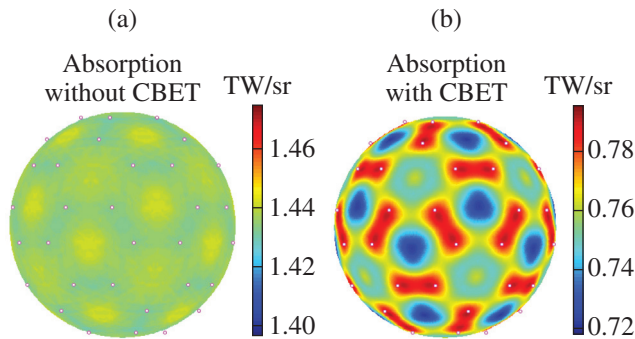


Figure 15.19  
 Surface map of the absorbed power over the target surface: (a) without CBET and (b) with CBET. The white dots show the positions of the beam centers.

the absorption surface map, the effects of this nonuniformity cannot be captured by a 1-D or 2-D hydrodynamics code.

**CBET Mitigation Using Wavelength Detuning**

One possible scheme for CBET mitigation during symmetric direct-drive implosions is wavelength detuning between groups of beams.<sup>47</sup> The 60 beams of the OMEGA Laser System originate from a single seed-pulse driver that is split three ways into “legs” and amplified separately to feed 20 beams each. The beams from each leg are distributed around the target chamber (Fig. 15.15). By shifting the wavelength of two of the legs in such a way that all three legs have different wavelengths, the CBET coupling between the groups of beams fed by the legs could be altered. With sufficient wavelength shifting, the groups of beams could be effectively decoupled from each other.

1. Single-Beam Wavelength Shift

Figure 15.20 shows the effect on absorbed laser power of shifting the wavelength of a single beam in a 60-beam symmetric implosion while keeping the other 59 beams fixed at 351 nm. The modeling predicts that small wavelength shifts can significantly increase or decrease the power absorbed in the single wavelength-shifted beam and that it takes a wavelength shift of  $|\Delta\lambda| > 30 \text{ \AA}$  to completely decouple the beam from the other 59 beams. The behavior shown in Fig. 15.20

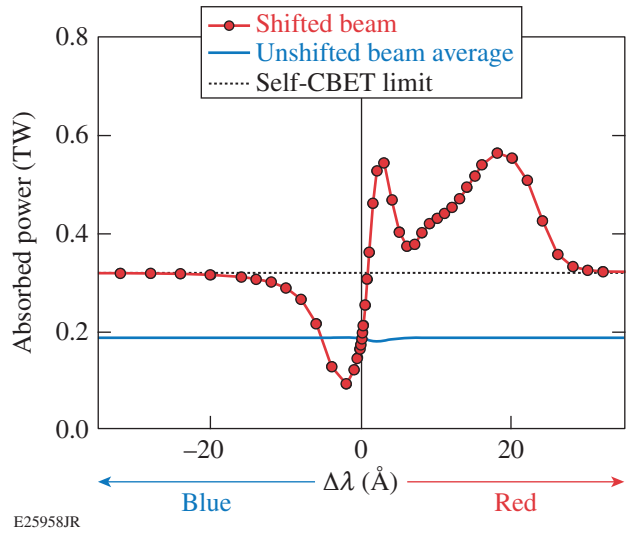


Figure 15.20  
 Absorbed power per beam in the OMEGA 60-beam geometry when one beam is wavelength shifted. The plot with red dots is the absorbed power in the single wavelength-shifted beam. The solid blue curve is the average absorbed power for the other 59 beams. The dotted black line is the absorbed power for a beam completely decoupled from all other beams but still experiencing CBET with itself.

is complicated because of the complex 3-D crossings with 59 other beams, but the behavior can be broken down into a few general phenomena.

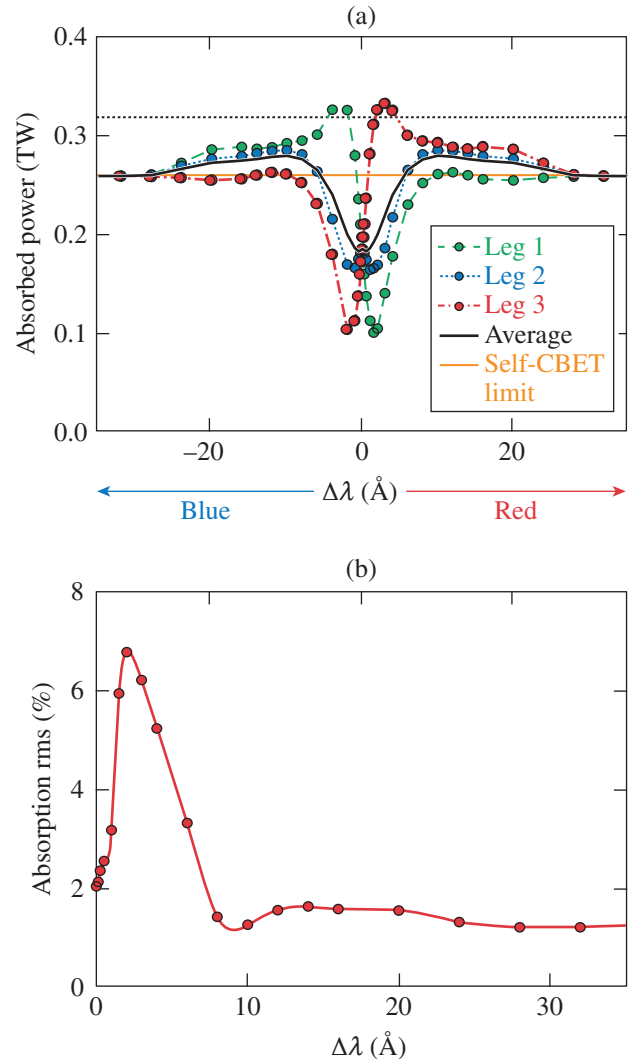
When  $\Delta\lambda$  is increased *negatively*, less Doppler shift is required to satisfy the IAW dispersion relation [Eq. (1)] for power loss in the central beamlets entering the plasma. This moves their resonance to smaller radii, where the plasma velocity is lower and the density is higher. Here the CBET coupling is stronger [Eq. (4)], increasing the losses compared to the  $\Delta\lambda = 0$  case. At the same negative wavelength shift, the resonance for the power gain of the large-impact parameter beamlets moves radially outward, where the coupling parameter is weaker, thereby decreasing their power gain. Both effects reduce the total power absorption for the shifted beam, but the increased losses of the central beamlets are the primary source of the sharp drop in absorbed power shown in Fig. 150.20 as  $\Delta\lambda$  is increased negatively. The absorbed power reaches a minimum at a shift of  $\Delta\lambda \approx -2 \text{ \AA}$  and then rises again as the resonance location for the power loss moves inside the beam shadow (Fig. 150.12) and CBET losses decrease until the beams decouple at  $\Delta\lambda < -30 \text{ \AA}$ . When  $\Delta\lambda$  is increased *positively*, the resonance shifts are reversed, reducing the losses of the central beamlets, increasing the gains in the outer beamlets, and producing a sharp rise in the absorbed power that peaks near  $\Delta\lambda \approx 3 \text{ \AA}$ . Because the beam can gain energy from the 59 other beams, the total power absorbed from the shifted beam can exceed the original power in that beam (0.35 TW). For positive  $\Delta\lambda$ , a second maximum occurs near  $\Delta\lambda \approx 18 \text{ \AA}$ . This broad peak occurs because the wavelength shift is large enough to change the direction of CBET for the incoming central beamlets such that they gain energy while entering into the plasma from the other 59 beams.

## 2. Three-Leg Wavelength Shifts

Figure 150.21 shows the effect that shifting the wavelength of the three OMEGA legs has on the absorbed power and its uniformity over the implosion target for the coronal plasma conditions modeled. When  $\Delta\lambda$  is given as the wavelength shift, it means that the beams in leg 1 are wavelength shifted by  $-\Delta\lambda$  and those in leg 3 are shifted by  $+\Delta\lambda$ , while the beams in leg 2 remain unshifted at 351 nm. As  $\Delta\lambda$  is increased from zero, CBET losses in leg 1 increase and the absorbed power in leg 1 beams drops, while the opposite occurs in leg 3, whose gains increase from CBET [Fig. 150.21(a)]. This loss/gain grows sharply until about  $\Delta\lambda \approx 2 \text{ \AA}$ . Here, the difference in absorbed power between legs 1 and 3 is maximum. As  $\Delta\lambda$  is increased further, the CBET coupling between the legs decreases, and, as a result, the difference between their absorbed power decreases until  $\Delta\lambda > 30 \text{ \AA}$ ,

where the legs are essentially decoupled. If  $\Delta\lambda$  is negative, these effects remain the same except the roles of leg 1 and leg 3 are reversed. Of particular interest is the region where  $\Delta\lambda \approx 10 \text{ \AA}$ . Here, the absorbed power averaged over all 60 beams is higher than the decoupled case ( $\Delta\lambda > 30 \text{ \AA}$ ), indicating that CBET may work in favor of increased implosion drive.

Figure 150.21(b) shows that as  $\Delta\lambda$  is increased from zero, the absorption nonuniformity (rms of the absorbed energy over the target surface) increases sharply to a maximum



E25959JR

Figure 150.21 Effect of wavelength shifting the three legs (20 beams each) of the OMEGA 60-beam geometry on (a) the absorbed power per beam in each leg and (b) the root mean square (rms) of the absorbed energy over the target surface calculated by radially integrating the 3-D total absorption. Negative  $\Delta\lambda$  shifts produce a reflection of Fig. 150.20(b) because of the symmetry shown in Fig. 150.20(a).

around  $\Delta\lambda \approx 2 \text{ \AA}$ , then falls as  $\Delta\lambda$  continues to increase and the legs decouple. For  $\Delta\lambda > 8 \text{ \AA}$ , the absorption nonuniformity changes only weakly, but at the same location as the maximum total absorption ( $\Delta\lambda \approx 10 \text{ \AA}$ ), there is a local minimum in the absorption nonuniformity of 1.3%, which is almost as small as the value when the legs are completely decoupled (1.2%). Figure 150.22 shows absorption surface maps calculated for wavelength shifts between the legs of  $2 \text{ \AA}$ ,  $6 \text{ \AA}$ , and  $10 \text{ \AA}$ . Not only does the total absorption rms change with  $\Delta\lambda$ , but the surface pattern of the nonuniformity varies as well.

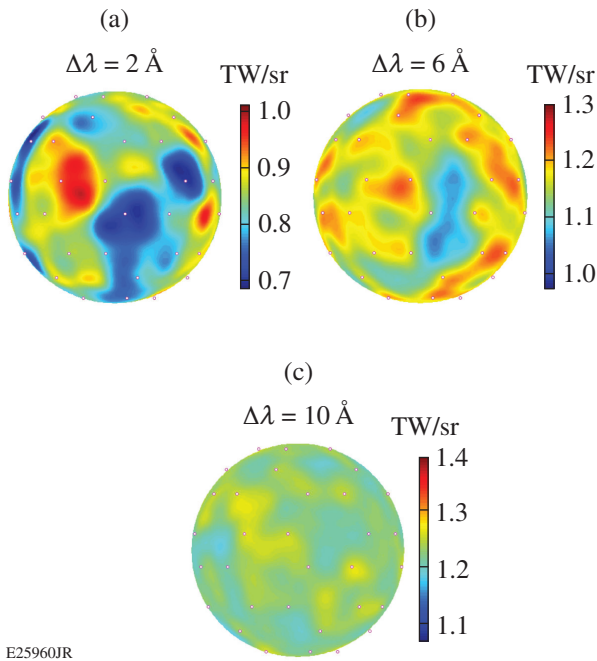


Figure 150.22  
Nonuniformity of the absorbed power of the implosion target surface for (a)  $\Delta\lambda = 2\text{-\AA}$  rms = 6.8%; (b)  $\Delta\lambda = 6\text{-\AA}$  rms = 3.3%; and (c)  $\Delta\lambda = 10\text{-\AA}$  rms = 1.3%. Color bars for all three plots are set to cover similar magnitudes of rms variation.

### Summary

A fully 3-D modeling of CBET for direct-drive symmetric implosions has been used to investigate the effects of wavelength detuning on CBET. The 3-D ray-based CBET model was benchmarked to full-wave calculations, providing confidence in the implementation of the model. For this study, coronal plasma conditions from late in the drive pulse of a typical warm OMEGA implosion were modeled. The model calculations show that beams with relative angles between  $45^\circ$  to  $90^\circ$  are most significant for CBET in OMEGA direct-drive implosions. The redistribution of laser power by CBET increases the absorption rms nonuniformity by an order of

magnitude. Implosion degradation effects resulting from this increase in absorption nonuniformity from CBET should be studied by 3-D hydrodynamic modeling. By shifting the relative wavelengths of three groups of laser beams by  $\sim 10 \text{ \AA}$ , the total laser absorption was maximized and the rms absorption nonuniformity nearly minimized for these plasma conditions.

### ACKNOWLEDGMENT

This material is based upon work supported by the Department of Energy National Nuclear Security Administration under Award Number DE-NA0001944, the University of Rochester, and the New York State Energy Research and Development Authority.

### REFERENCES

1. J. Nuckolls et al., *Nature* **239**, 139 (1972).
2. R. S. Craxton, K. S. Anderson, T. R. Boehly, V. N. Goncharov, D. R. Harding, J. P. Knauer, R. L. McCrory, P. W. McKenty, D. D. Meyerhofer, J. F. Myatt, A. J. Schmitt, J. D. Sethian, R. W. Short, S. Skupsky, W. Theobald, W. L. Kruer, K. Tanaka, R. Betti, T. J. B. Collins, J. A. Delettrez, S. X. Hu, J. A. Marozas, A. V. Maximov, D. T. Michel, P. B. Radha, S. P. Regan, T. C. Sangster, W. Seka, A. A. Solodov, J. M. Soures, C. Stoeckl, and J. D. Zuegel, *Phys. Plasmas* **22**, 110501 (2015).
3. V. N. Goncharov, T. C. Sangster, T. R. Boehly, S. X. Hu, I. V. Igumenshchev, F. J. Marshall, R. L. McCrory, D. D. Meyerhofer, P. B. Radha, W. Seka, S. Skupsky, C. Stoeckl, D. T. Casey, J. A. Frenje, and R. D. Petrasso, *Phys. Rev. Lett.* **104**, 165001 (2010).
4. S. E. Bodner, D. G. Colombant, J. H. Gardner, R. H. Lehmborg, S. P. Obenschain, L. Phillips, A. J. Schmitt, J. D. Sethian, R. L. McCrory, W. Seka, C. P. Verdon, J. P. Knauer, B. B. Afeyan, and H. T. Powell, *Phys. Plasmas* **5**, 1901 (1998).
5. S. Skupsky and R. S. Craxton, *Phys. Plasmas* **6**, 2157 (1999).
6. J. H. Gardner and S. E. Bodner, *Phys. Fluids* **29**, 2672 (1986).
7. S. Skupsky and K. Lee, *J. Appl. Phys.* **54**, 3662 (1983).
8. I. M. Begg and R. A. Cairns, *J. Phys. D: Appl. Phys.* **9**, 2341 (1976).
9. C. J. Randall, J. J. Thomson, and K. G. Estabrook, *Phys. Rev. Lett.* **43**, 924 (1979).
10. R. W. Short and E. A. Williams, *Phys. Rev. Lett.* **47**, 337 (1981).
11. W. L. Kruer et al., *Phys. Plasmas* **3**, 382 (1996).
12. J. F. Myatt, J. Zhang, R. W. Short, A. V. Maximov, W. Seka, D. H. Froula, D. H. Edgell, D. T. Michel, I. V. Igumenshchev, D. E. Hinkel, P. Michel, and J. D. Moody, *Phys. Plasmas* **21**, 055501 (2014).
13. R. K. Kirkwood et al., *Phys. Rev. Lett.* **76**, 2065 (1996).
14. K. B. Wharton et al., *Phys. Rev. Lett.* **81**, 2248 (1998).

15. K. B. Wharton *et al.*, *Phys. Plasmas* **6**, 2144 (1999).
16. R. K. Kirkwood, J. D. Moody, A. B. Langdon, B. I. Cohen, E. A. Williams, M. R. Dorr, J. A. Hittinger, R. Berger, P. E. Young, L. J. Suter, L. Divol, S. H. Glenzer, O. L. Landen, and W. Seka, *Phys. Rev. Lett.* **89**, 215003 (2002).
17. W. Seka, H. A. Baldis, J. Fuchs, S. P. Regan, D. D. Meyerhofer, C. Stoeckl, B. Yaakobi, R. S. Craxton, and R. W. Short, *Phys. Rev. Lett.* **89**, 175002 (2002).
18. R. K. Kirkwood *et al.*, *Phys. Plasmas* **12**, 112701 (2005).
19. C. J. McKinstrie *et al.*, *Phys. Plasmas* **3**, 2686 (1996).
20. C. J. McKinstrie *et al.*, *Phys. Plasmas* **5**, 1142 (1998).
21. H. A. Rose and S. Ghosal, *Phys. Plasmas* **5**, 1461 (1998).
22. J. A. F. Hittinger *et al.*, *J. Comput. Phys.* **209**, 695 (2005).
23. J. D. Lindl *et al.*, *Phys. Plasmas* **11**, 339 (2004).
24. P. Michel *et al.*, *Phys. Rev. Lett.* **102**, 025004 (2009).
25. P. Michel *et al.*, *Phys. Plasmas* **16**, 042702 (2009).
26. P. Michel *et al.*, *Phys. Plasmas* **17**, 056305 (2010).
27. P. Michel *et al.*, *Phys. Rev. E* **83**, 046409 (2011).
28. S. H. Glenzer *et al.*, *Science* **327**, 1228 (2010).
29. E. L. Dewald *et al.*, *Phys. Rev. Lett.* **111**, 235001 (2013).
30. J. D. Moody *et al.*, *Nat. Phys.* **8**, 344 (2012).
31. G. D. Kerbel, Lawrence Livermore National Laboratory, Livermore, CA, Report UCRL-53101 (1981).
32. D. J. Strozzi *et al.*, *Phys. Rev. Lett.* **118**, 025002 (2017).
33. M. M. Marinak *et al.*, *Phys. Plasmas* **8**, 2275 (2001).
34. D. H. Edgell, W. Seka, J. A. Delettrez, R. S. Craxton, V. N. Goncharov, I. V. Igumenshchev, J. F. Myatt, A. V. Maximov, R. W. Short, T. C. Sangster, and R. E. Bahr, *Bull. Am. Phys. Soc.* **53**, 168 (2008).
35. W. Seka, D. H. Edgell, J. P. Knauer, J. F. Myatt, A. V. Maximov, R. W. Short, T. C. Sangster, C. Stoeckl, R. E. Bahr, R. S. Craxton, J. A. Delettrez, V. N. Goncharov, I. V. Igumenshchev, and D. Shvarts, *Phys. Plasmas* **15**, 056312 (2008).
36. I. V. Igumenshchev, D. H. Edgell, V. N. Goncharov, J. A. Delettrez, A. V. Maximov, J. F. Myatt, W. Seka, A. Shvydky, S. Skupsky, and C. Stoeckl, *Phys. Plasmas* **17**, 122708 (2010).
37. D. T. Michel, V. N. Goncharov, I. V. Igumenshchev, R. Epstein, and D. H. Froula, *Phys. Rev. Lett.* **111**, 245005 (2013).
38. C. J. Randall, J. R. Albritton, and J. J. Thomson, *Phys. Fluids* **24**, 1474 (1981).
39. D. H. Edgell, W. Seka, J. A. Delettrez, R. S. Craxton, V. N. Goncharov, I. V. Igumenshchev, J. F. Myatt, A. V. Maximov, R. W. Short, T. C. Sangster, and R. E. Bahr, *Bull. Am. Phys. Soc.* **54**, 145 (2009).
40. I. V. Igumenshchev, W. Seka, D. H. Edgell, D. T. Michel, D. H. Froula, V. N. Goncharov, R. S. Craxton, L. Divol, R. Epstein, R. Follett, J. H. Kelly, T. Z. Kosc, A. V. Maximov, R. L. McCrory, D. D. Meyerhofer, P. Michel, J. F. Myatt, T. C. Sangster, A. Shvydky, S. Skupsky, and C. Stoeckl, *Phys. Plasmas* **19**, 056314 (2012).
41. J. A. Marozas, T. J. B. Collins, D. H. Edgell, I. V. Igumenshchev, and J. F. Myatt, *Bull. Am. Phys. Soc.* **56**, 241 (2011).
42. J. Delettrez, R. Epstein, M. C. Richardson, P. A. Jaanimagi, and B. L. Henke, *Phys. Rev. A* **36**, 3926 (1987).
43. P. B. Radha, T. J. B. Collins, J. A. Delettrez, Y. Elbaz, R. Epstein, V. Yu. Glebov, V. N. Goncharov, R. L. Keck, J. P. Knauer, J. A. Marozas, F. J. Marshall, R. L. McCrory, P. W. McKenty, D. D. Meyerhofer, S. P. Regan, T. C. Sangster, W. Seka, D. Shvarts, S. Skupsky, Y. Srebro, and C. Stoeckl, *Phys. Plasmas* **12**, 056307 (2005).
44. D. H. Froula, I. V. Igumenshchev, D. T. Michel, D. H. Edgell, R. Follett, V. Yu. Glebov, V. N. Goncharov, J. Kwiatkowski, F. J. Marshall, P. B. Radha, W. Seka, C. Sorce, S. Stagnitto, C. Stoeckl, and T. C. Sangster, *Phys. Rev. Lett.* **108**, 125003 (2012).
45. I. V. Igumenshchev, D. H. Froula, D. H. Edgell, V. N. Goncharov, T. J. Kessler, F. J. Marshall, R. L. McCrory, P. W. McKenty, D. D. Meyerhofer, D. T. Michel, T. C. Sangster, W. Seka, and S. Skupsky, *Phys. Rev. Lett.* **110**, 145001 (2013).
46. D. H. Froula, T. J. Kessler, I. V. Igumenshchev, R. Betti, V. N. Goncharov, H. Huang, S. X. Hu, E. Hill, J. H. Kelly, D. D. Meyerhofer, A. Shvydky, and J. D. Zuegel, *Phys. Plasmas* **20**, 082704 (2013).
47. J. A. Marozas, Laboratory for Laser Energetics, private communication (2017).
48. J. F. Myatt, J. G. Shaw, R. K. Follett, and D. H. Edgell, *Bull. Am. Phys. Soc.* **61**, BAPS.2016.DPP.UI3.4 (2016).
49. MATLAB® R2009a, The MathWorks Inc., Natick, MA 01760-2098 (<http://www.mathworks.com>).
50. D. H. Edgell, W. Seka, J. A. Delettrez, R. S. Craxton, V. N. Goncharov, I. V. Igumenshchev, J. Myatt, A. V. Maximov, R. W. Short, T. C. Sangster, and R. E. Bahr, *Bull. Am. Phys. Soc.* **52**, 195 (2007).
51. M. Born and E. Wolf, *Principles of Optics: Electromagnetic Theory of Propagation, Interference, and Diffraction of Light*, 7th expanded ed. (Cambridge University, Cambridge, England, 1999), pp. 752–758.
52. A. Sharma, D. V. Kumar, and A. K. Ghatak, *Appl. Opt.* **21**, 984 (1982).
53. L. Friedland and I. B. Bernstein, *Phys. Rev. A* **21**, 666 (1980).
54. Yu. A. Kravtsov and Yu. I. Orlov, *Sov. Phys.-Usp.* **26**, 1038 (1983).
55. W. L. Kruer, in *The Physics of Laser Plasma Interactions*, *Frontiers in Physics*, Vol. 73, edited by D. Pines (Westview, Boulder, CO, 2003), Chap. 4, p. 34.

56. T. Dewandre, J. R. Albritton, and E. A. Williams, *Phys. Fluids* **24**, 528 (1981).
57. W. L. Kruer, in *The Physics of Laser Plasma Interactions*, *Frontiers in Physics*, Vol. 73, edited by D. Pines (Westview, Boulder, CO, 2003).
58. A. K. Davis, D. Cao, D. T. Michel, M. Hohenberger, D. H. Edgell, R. Epstein, V. N. Goncharov, S. X. Hu, I. V. Igumenshchev, J. A. Marozas, A. V. Maximov, J. F. Myatt, P. B. Radha, S. P. Regan, T. C. Sangster, and D. H. Froula, *Phys. Plasmas* **23**, 056306 (2016).
59. J. Myatt, A. V. Maximov, W. Seka, R. S. Craxton, and R. W. Short, *Phys. Plasmas* **11**, 3394 (2004).
60. P. Michel *et al.*, *Phys. Plasmas* **20**, 056308 (2013).
61. T. R. Boehly, R. L. McCrory, C. P. Verdon, W. Seka, S. J. Loucks, A. Babushkin, R. E. Bahr, R. Boni, D. K. Bradley, R. S. Craxton, J. A. Delettrez, W. R. Donaldson, R. Epstein, D. Harding, P. A. Jaanimagi, S. D. Jacobs, K. Kearney, R. L. Keck, J. H. Kelly, T. J. Kessler, R. L. Kremens, J. P. Knauer, D. J. Lonobile, L. D. Lund, F. J. Marshall, P. W. McKenty, D. D. Meyerhofer, S. F. B. Morse, A. Okishev, S. Papernov, G. Pien, T. Safford, J. D. Schnittman, R. Short, M. J. Shoup III, M. Skeldon, S. Skupsky, A. W. Schmid, V. A. Smalyuk, D. J. Smith, J. M. Soures, M. Wittman, and B. Yaakobi, *Fusion Eng. Des.* **44**, 35 (1999).
62. P. Michel, L. Divol, D. Turnbull, and J. D. Moody, *Phys. Rev. Lett.* **113**, 205001 (2014).

---

## Picosecond Time-Resolved Measurements of Dense Plasma Line Shifts

Understanding the time-averaged and time-dependent response of ions in dense plasma is important for correctly interpreting and modeling atomic structure and radiation transport in extreme environments,<sup>1,2</sup> including stellar atmospheres<sup>3</sup> and imploding inertial fusion capsules.<sup>4</sup> The potential in and near an ion immersed in a dense plasma is influenced by its bound electrons, free electrons, and neighboring ions. These influences can change the radiative and thermodynamic properties of the plasma by modifying the energy levels that are available to an ion and causing energy-level shifts.<sup>5</sup>

Dense plasma line shifts originate from free-electron modification of the ionic potential.<sup>1,2</sup> Free electrons in the ion sphere screen the nuclear charge and shift bound energy levels toward the continuum. The energy separation between levels is decreased for a given bound-electron configuration, and emission lines are shifted to lower photon energies. Correct identification of this effect helped resolve the disparity between spectroscopically inferred white dwarf masses and the results from other measurement methods and the predictions of general relativity.<sup>6</sup>

While dense plasma line shifts have been described mathematically<sup>7</sup> and confirmed experimentally,<sup>8</sup> few measurements have tested line-shift model predictions at high energy density, leading to an incomplete picture of how this process is understood and modeled in extreme conditions. Data comparisons to line-shift model predictions in this regime have been hampered by the difficulty of obtaining uniform, well-characterized, and high-energy-density (HED) plasmas. Line-shift measurements are especially needed in hot dense plasmas to provide a stringent test for analytic and detailed atomic kinetics and radiative-transfer calculations. Equally important, line-shift measurements can provide a sensitive benchmark for free-electron distribution models within the ion sphere—an important application of the  $N$ -body problem.<sup>9</sup>

This article reports the first picosecond time-resolved measurements of dense plasma line shifts of the  $1s2p-1s^2$  transition in He-like Al ions as a function of the instantaneous plasma

conditions. Line shifts were measured with picosecond time resolution for free-electron densities of  $1$  to  $5 \times 10^{23} \text{ cm}^{-3}$  and temperatures of  $250$  to  $375 \text{ eV}$ . The plasma conditions were inferred with well-quantified errors from spectroscopic measurements of the Al He $_{\alpha}$  complex. The data are compared to a generalized analytic model proposed by Li *et al.*<sup>10</sup> based on a parameterization of numerical ion-sphere model calculations. The predicted line shifts show broad agreement with the data over the full range of densities and temperatures studied, with evidence for deviation from the experimental data at the most-extreme densities. This work provides an experimental test of a simplified method that calculates quantum-number-dependent energy level shifts for ions in dense, finite-temperature plasma.

The experiments were carried out at LLE's Multi-Terawatt (MTW) Laser Facility.<sup>11</sup> Figure 150.23(a) shows the experimental setup. The laser directly irradiated small-mass targets with  $0.7$ -ps,  $\leq 16$ -J pulses at the laser's fundamental wavelength ( $\lambda = 1054 \text{ nm}$ ) or second harmonic. The laser was focused to an  $\sim 5$ - $\mu\text{m}$  full-width-at-half-maximum (FWHM) focal spot by an  $f/3$  off-axis parabolic mirror at normal incidence to the target at intensities greater than  $10^{18} \text{ W/cm}^2$ . The targets were thin plastic foils with a buried Al microdot. The microdot was vacuum deposited in a  $0.2$ - $\mu\text{m}$  layer on a  $1$ - $\mu\text{m}$  parylene- $N$  (CH) support. The thickness of the front parylene- $N$  overcoat was varied between  $0$  and  $2 \mu\text{m}$  to access different plasma densities. The Al microdot was kept purposefully thin to limit spatial gradients, while the outer plastic layers constrain sample expansion to achieve near-solid-density conditions.<sup>12</sup>

High-intensity laser pulses with low contrast reduce the maximum electron density that can be achieved in buried-layer target interactions by causing the target to prematurely heat and decompress.<sup>13</sup> In the experiments reported here, free-electron densities of up to  $2 \times 10^{23} \text{ cm}^{-3}$  were achieved at the laser's fundamental wavelength with a measured temporal contrast of the order of  $10^8$  up to  $100 \text{ ps}$  prior to the main pulse.<sup>14</sup> Experiments with high-contrast, frequency-doubled pulses achieved free-electron densities of the order of  $5 \times 10^{23} \text{ cm}^{-3}$ . Based on work by previous authors and the measured contrast of the  $1\omega$

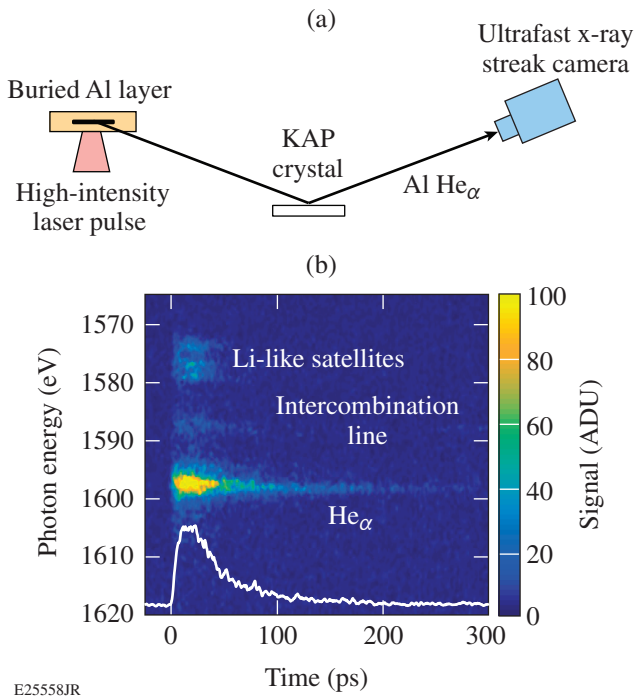


Figure 150.23 (a) Experimental setup. (b) Example streaked He $\alpha$  emission from a rapidly heated Al surface layer. The Li-like satellites, intercombination line, and He $\alpha$  line are shown. KAP: potassium acid phthalate; ADU: analog digital unit.

beam, the temporal contrast of the frequency-doubled beam is estimated to be  $10^{12}$  (Ref. 15); however, no on-shot contrast measurement was available for this particular experiment. Residual  $1\omega$  light was rejected at a spectral contrast of the order of  $10^{12}$  by six transport mirrors with 99%  $1\omega$  extinction coatings.

Picosecond streaked x-ray spectroscopy was used to infer the density and temperature of the Al layer. For this measurement, a conically curved potassium acid phthalate (KAP) streaked x-ray spectrometer was used in combination with a time-integrating flat pentaerythritol (PET) crystal spectrometer. The streaked spectrometer was configured to study Al He $\alpha$  ( $1s2p-1s^2$ ) thermal line emission with spectral resolving power  $E/\Delta E \sim 1000$  and 2-ps temporal resolution.<sup>16</sup> Time-integrated spectra were measured on each shot and used to correct the streaked spectra for variations in spectral sensitivity introduced by the photocathode.<sup>17</sup>

It is noted that the plasma-induced line shifts measured in the experiment could be exaggerated or disguised by streak camera charge-coupled-device (CCD) clocking errors. The CCD clocking was measured offline using a structured photocathode illuminated by a static x-ray source. The tests identified

a  $0.46 \pm 0.01^\circ$  correction that was applied to the experimental data. Experimental tests with low-density, laser-driven Al plasmas confirm that the clocking offset was properly corrected.

Figure 150.23(b) shows example streaked data where the dispersion of the streaked x-ray spectrometer was determined *in situ* from the emission lines of He- and Li-like Al ions at low plasma density. A well-resolved emission spectrum was selected after the plasma was allowed to expand for 12 ps after the high-intensity pulse [Fig. 150.24(a)]. The initial He $\alpha$  and intercombination line positions cannot be directly identified with tabulated transition energies because the plasma environment modifies the ionic energy-level structure. The Li-like satellite lines are not expected to shift measurably because of the screening effect of the  $n = 2$  spectator electron.<sup>18</sup> The

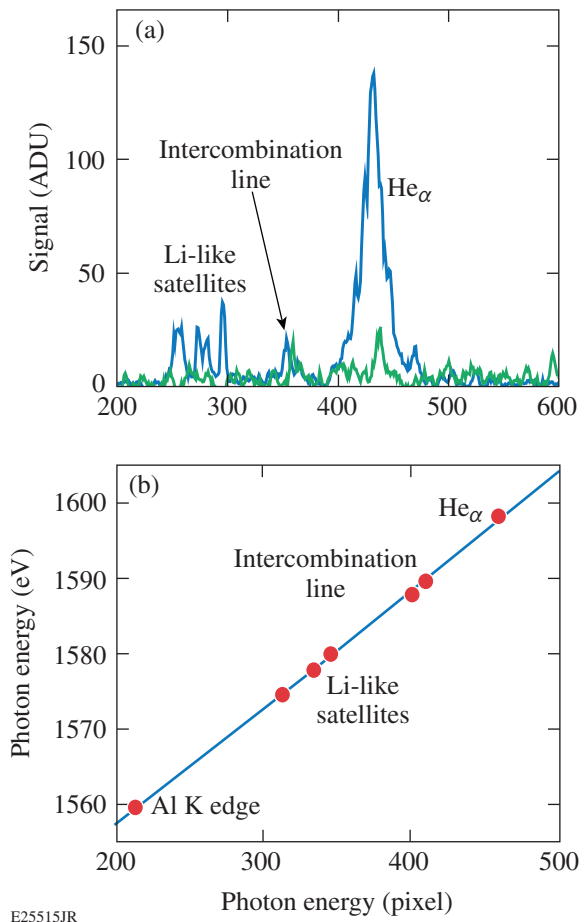


Figure 150.24 (a) X-ray spectra from an Al surface layer at  $t_0 + 12$  ps (blue) and  $t_0 + 275$  ps (green). (b) The measured peak positions were identified with tabulated transition energies using an analytic dispersion calibration derived from Bragg's law for the spectrometer geometry.

green trace in Fig. 150.24(a) corresponds to the latest time in the plasma evolution that could be reliably measured, corresponding to  $t_0 + 275$  ps, where  $t_0$  is the arrival time of the high-intensity laser pulse at the target. At this time, the plasma consists of approximately isolated radiators and the  $\text{He}_\alpha$  resonance and intercombination lines are observed at a higher photon energy. The observed positions of these lines are constant in time and provide an absolute energy fiducial to register the calibration. Additional Al K-edge measurements were carried out to verify the calibration. A 2- $\mu\text{m}$  Al filter placed *in situ* over the detector aperture was backlit by laser-produced x rays and the K-shell absorption edge at 1559.6 eV was recorded. The measured edge location is free from plasma effects and provides an absolute energy fiducial to confirm the dispersion slope and offset.

The measured fiducial position  $P$  was related to the photon energy  $E$  via Bragg's law for the spectrometer geometry:

$$P(\text{pixel}) = A \cdot \tan \left[ a \sin \left( \frac{hc}{2d} \frac{1}{E} \right) \right] + B, \quad (1)$$

where  $A$  and  $B$  are fitting parameters,  $h$  is Planck's constant,  $c$  is the speed of light, and  $2d = 26.64 \text{ \AA}$  is the Bragg spacing of the KAP crystal. The results of the calibration are shown in Fig. 150.24(b). A conservative estimate for the uncertainty in peak position yields two pixels, or 0.25 eV. Uncertainty in the location of the K edge is slightly larger because of degraded spectral resolution at the edge of the streak camera field of view, where the K edge was measured. This uncertainty provides the dominant contribution to the calculated error in the measured shifts. The overall uncertainty in the dispersion is within the

width of the data points in Fig. 150.24(b). This dispersion was applied to all data collected in this work. An important point for these measurements is that the dispersion was established self-consistently without reference to plasma-dependent fiducials. Previous work<sup>19,20</sup> relied on time-averaged measurements of the  $\text{K}_\alpha$  line shape to set the dispersion. The technique presented here provides the dispersion over the full spectral range of interest, registered to the cold Al K-shell absorption edge.

Figure 150.25(a) shows the streaked data gathered from an Al layer heated by a 16-J, 0.7-ps pulse focused to  $\sim 1 \times 10^{19} \text{ W/cm}^2$ . The Al was enclosed on both sides by a 1- $\mu\text{m}$  parylene- $N$  tamper. The data were corrected for the streak tube's geometric curvature and variations in photocathode spectral sensitivity. The time axis was calibrated in separate tests. The Stark-broadened resonance line and the commensurate strong satellite emission indicate high plasma density over the duration of the experiment. Spectra were averaged over a five-pixel temporal window (shaded region) corresponding to the streak camera's temporal impulse response. A linear background was removed from the data.

The  $\text{He}_\alpha$  FWHM and  $\text{He}_\alpha$ -to-satellite intensity ratio was interpreted using a nonlocal-thermodynamic-equilibrium (NLTE) collisional-radiative atomic model<sup>21</sup> to infer the Al density and temperature as a function of time.<sup>2,22</sup> The model calculated synthetic spectra for Al IX–XIV ions over a regular density and temperature grid of 0.1 to 6  $\text{g/cm}^3$  and 100 to 600 eV, respectively. The simulation was carried out in 1-D for a 0.2- $\mu\text{m}$  Al slab. Satellite contributions to the line shape were treated in detail by including transitions from all ions with non-negligible populations. Satellite blending with the

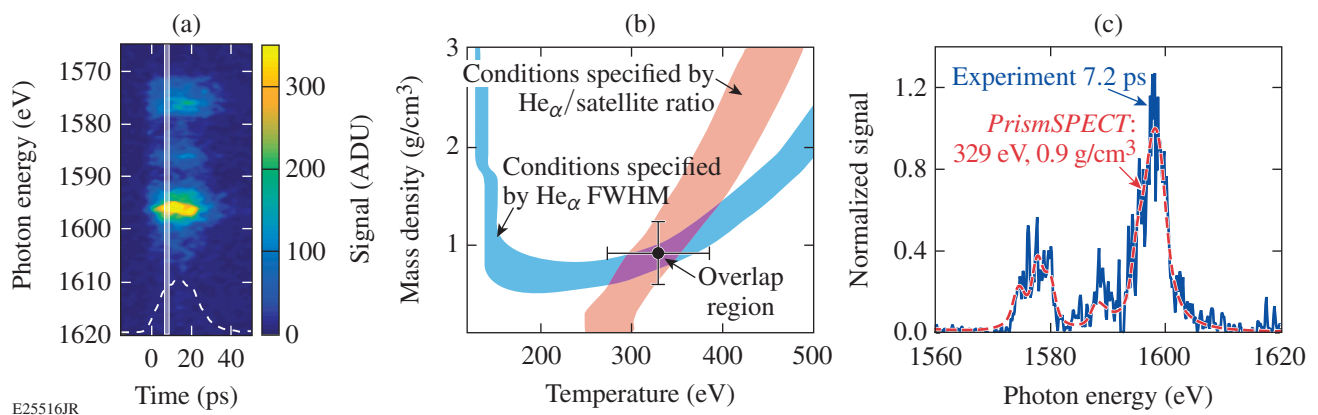


Figure 150.25

(a) Streaked  $\text{He}_\alpha$  emission from a buried Al layer (1  $\mu\text{m}$  CH). (b) The plasma conditions are inferred from the  $\text{He}_\alpha$  intensity ratio (red) and full width at half maximum (FWHM) (blue). (c) The synthetic spectrum corresponding to  $T_e = 330$  eV and  $\rho = 0.9 \text{ g/cm}^3$  (red) is compared to the data (blue).

resonance line may otherwise be misinterpreted as spurious Stark broadening or red shift.<sup>23</sup> The effects of radiation transfer were included using an escape probability approach based on local escape factors to calculate photoexcitation rates.<sup>21</sup> The line profiles were calculated with the effects of Doppler, Stark, natural, Auger, and opacity broadening.<sup>24</sup> The synthetic spectra were convolved with the detector resolving power, and the  $\text{He}_\alpha$  FWHM and  $\text{He}_\alpha$ -to-satellite intensity ratio were tabulated for each temperature and density grid point for comparison to the measured spectra. Apparent  $\text{He}_\alpha$  shifts caused by line broadening and satellite blending were calculated from the model to verify that the observed shifts were caused by true plasma effects.

The experimental  $\text{He}_\alpha$ -to-satellite intensity ratio was formed over the same spectral bands as the synthetic data. The error was determined from a Monte Carlo study that produced a ratio distribution from uncertainties introduced by photon statistics and the analysis procedure. The distribution variance characterizes the ratio error with coupled sources of uncertainty. For the lineout selected in Fig. 150.25(a), the ratio was  $2.5 \pm 0.5$ . Figure 150.25(b) shows the temperature and density contour specified by the measured ratio (red). The  $\text{He}_\alpha$  FWHM provides a second measurement to constrain the inferred conditions.<sup>25</sup> The FWHM was measured from a spline fit through the data to minimize random error introduced by statistical signal fluctuations. Noise was considered separately as a source of uncertainty by calculating the probability distribution for the measured width based on the likelihood that statistical signal fluctuations could be spuriously detected as FWHM crossing points. For the data shown, the width was  $5.3 \pm 0.6$  eV. The measured FWHM specifies a second contour in temperature and density space (blue) that constrains the inferred temperature and density. The width of the two contours and the size of the overlap region are related to the uncertainties in the measured quantities.

An estimate for the true temperature and density is calculated from the mean temperature and density in the overlap region. The error in the estimated temperature and density corresponds to the extent of the overlap region along each axis. The conditions were inferred to be  $330 \pm 56$  eV and  $0.9 \pm 0.3$  g/cm<sup>3</sup> ( $n_e = 2.2 \pm 0.8 \times 10^{23}$  cm<sup>-3</sup>). Figure 150.25(c) shows the unfiltered spectrum and the model prediction for the measured conditions. The model considers the instrument resolving power and reproduces the experimental data well. It is noted that the data have been uniformly shifted to higher photon energies by 2.4 eV for comparison with the synthetic

spectrum since the atomic kinetics model used here does not include dense plasma line shifts.

The spectral shifts were quantified by the difference between the first moment of the measured  $\text{He}_\alpha$  line shape and the predicted (unshifted)  $\text{He}_\alpha$  line shape. The limits of integration were selected to fully encompass the  $\text{He}_\alpha$  line without contamination from the intercombination line. The uncertainty in the measured shift was calculated assuming independent contributions from dispersion calibration error and statistical signal fluctuations. The measured shift for the spectrum shown in Fig. 150.25(c) was  $2.4 \pm 0.3$  eV.

Figure 150.26(a) shows the measured  $\text{He}_\alpha$  line shifts for inferred electron densities from 1 to  $5 \times 10^{23}$  cm<sup>-3</sup>. The dataset is composed of well-resolved spectra with no self-reversal. The error bars are shown for a few representative data points at low, medium, and high densities. The asymmetric vertical error bars reflect the uncertainty in the measured location of the Al K-shell absorption edge used to register the absolute dispersion calibration. This uncertainty does not propagate to the inferred temperature and density since those quantities are sensitive only to the relative dispersion. The data show a nearly linear shift with increasing electron density.<sup>26</sup> The highest electron densities measured were near 80% of solid and were achieved with the high-contrast  $2\omega$  drive. The data were selected over a small range of temperatures between 250 and 375 eV.

For each data point, an apparent shift was calculated from the atomic kinetics model to confirm that the observed shifts were not spurious. These data are plotted in red and the typical error is within the data point. The magnitude of the apparent shift appears to decrease with electron density because the  $2\omega$  drive for high-density studies produced proportionately higher temperatures that suppress satellite enhancement of the red wings of the line profile.<sup>22</sup>

Predictions from a generalized analytic ion-sphere model proposed by Li *et al.*<sup>19</sup> are compared to the data in Fig. 150.26(a). The analytic approach relies on the self-consistent field ion-sphere model (SCFISM)<sup>27</sup> to obtain the self-consistent density distribution of bound and free electrons within the ion sphere. Relativistic atomic structure calculations of the bound wave functions are carried out in a screened nuclear potential determined from the electron density distribution. Detailed scaling studies were performed to obtain a generalized density- and temperature-dependent formula for the energy level structure in the plasma.

For each data point in Fig. 150.26(a), the analytic formulation was used to predict the line shift at the inferred temperature and density. The calculation is monoenergetic and considers only the  $1s2p-1s^2$  transition. The calculation agrees well with the data at low density but diverges at higher densities, likely because the calculation neglects unresolved satellites and other contributions to the line shape. An attempt was made to recover this information by adding the apparent shifts to the ion-sphere model predictions. This addition produces better agreement at low and moderate densities, as shown in Fig. 150.26(b). The error bars indicate uncertainty in the calculated shifts based on the density uncertainty in the corresponding data point. The temperature uncertainty was neglected since the model exhibits a weak dependence on electron temperature ( $\sim T_e^{-0.25}$ ).

Sensitive spectral measurements of this nature may prove to be a valuable test of electron screening models in extreme conditions. For example, improved agreement between the analytic model and the experimental data is obtained for an *ad hoc* 10% reduction of the ion-sphere radius [Fig. 150.26(b)]. The optimum reduction was determined by a single-parameter maximum-likelihood least squares fit to the data that considered uncertainties in the inferred densities and line shifts. The quality of the match is surprisingly sensitive to the scale factor. It is noted that a 40% increase in the inferred densities

can reproduce the improved agreement. It is unlikely, however, that the analysis overestimates the inferred densities by that amount, and it is improbable that densities above solid were achieved in the experiment.

Moreover, spectroscopic temperature and density measurements from K-shell ions can be sensitive to the choice of atomic model. Recent work has demonstrated that model discrepancies can contribute up to 30% uncertainty in the inferred conditions, mostly from uncertainty in Stark-line-shape calculations.<sup>28</sup> Model-dependent temperature and density measurements will become more reliable as theoretical and experimental work further validates line-shape models.

In summary, spectral line shifts of the  $1s2p-1s^2$  transition in He-like Al ions have been studied as a function of the instantaneous plasma conditions at high energy density. The line shifts were measured using a picosecond time-resolved x-ray spectrometer with an absolutely calibrated spectral dispersion. Buried-layer targets and a high-contrast  $2\omega$  laser driver provided access to densities near 80% of solid. The plasma conditions were inferred by comparing the measured spectra to calculations from a NLTE collisional-radiative atomic physics model. A generalized analytic line-shift model was found to be broadly consistent with the experimental data for all but

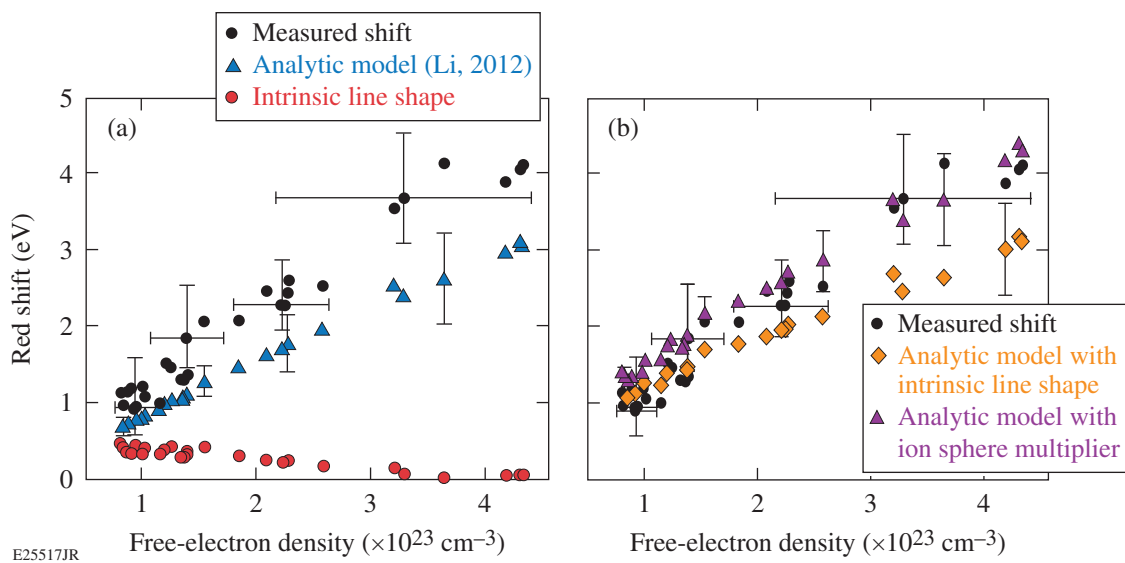


Figure 150.26

(a) Comparison of the data (black) to the analytic line-shift model (blue) and apparent shifts (red). (b) Comparison of the data (black) to the analytic line-shift model plus apparent shifts (orange) and the line-shift model with a scaled ion-sphere radius (purple). The optimum scale factor was determined by a single-parameter least squares fit to the data.

the highest densities studied. These findings are important to understanding plasma-dependent atomic structure and radiation transport in high-energy-density environments.

#### ACKNOWLEDGMENT

The authors gratefully acknowledge C. Stoeckl and W. Theobald for helpful discussions and diagnostic development and thank S. Hansen for her careful reading of this article.

This material is based upon work supported by the Department of Energy National Nuclear Security Administration under Award Number DE-NA0001944, the University of Rochester, and the New York State Energy Research and Development Authority.

#### REFERENCES

1. D. Salzmann, *Atomic Physics in Hot Plasmas*, International Series of Monographs on Physics, Vol. 97 (Oxford University Press, New York, 1998), Chap. 5, pp. 122–146.
2. H. R. Griem, *Principles of Plasma Spectroscopy* (Cambridge University, Cambridge, England, 1997).
3. F. J. Rogers and C. A. Iglesias, *Science* **263**, 50 (1994).
4. S. Atzeni and J. Meyer-ter-Vehn, *The Physics of Inertial Fusion: Beam Plasma Interaction, Hydrodynamics, Hot Dense Matter*, International Series of Monographs on Physics (Clarendon, Oxford, 2004).
5. O. Ciricosta *et al.*, *Nat. Commun.* **7**, 11713 (2016).
6. J. Halenka *et al.*, *Astrophys. J.* **808**, 131 (2015); H. M. Van Horn and V. Weidemann, eds. *White Dwarfs and Variable Degenerate Stars* (University of Rochester, Rochester, NY, 1979), IAU Colloquium 53.
7. D. B. Boercker and C. A. Iglesias, *Phys. Rev. A* **30**, 2771 (1984); C. F. Hooper, G. C. Junkel, M. A. Gunderson, D. A. Haynes, R. C. Mancini, D. Bradley, J. Delettrez, and P. Jaanimagi, in *Strongly Coupled Coulomb Systems*, edited by G. J. Kalman, J. M. Rommel, and K. Blagoev (Springer US, Boston, MA, 2002), pp. 385–389; G. C. Junkel *et al.*, *Phys. Rev. E* **62**, 5584 (2000); H. R. Griem, M. Blaha, and P. C. Kepple, *Phys. Rev. A* **41**, 5600 (1990).
8. A. Saemann *et al.*, *Phys. Rev. Lett.* **82**, 4843 (1999); K. Eidmann *et al.*, *J. Quant. Spectrosc. Radiat. Transf.* **65**, 173 (2000); O. Renner *et al.*, *J. Quant. Spectrosc. Radiat. Transf.* **99**, 523 (2006); F. Y. Khattak *et al.*, *J. Phys.: Conf. Ser.* **397**, 012020 (2012).
9. G. Buck, *Nature* **395**, 51 (1998).
10. X. Li and F. B. Rosmej, *Europhys. Lett.* **99**, 33001 (2012).
11. V. Bagnoud, I. A. Begishev, M. J. Guardalben, J. Puth, and J. D. Zuegel, *Opt. Lett.* **30**, 1843 (2005).
12. T. S. Perry *et al.*, *Phys. Rev. Lett.* **67**, 3784 (1991).
13. C. R. D. Brown *et al.*, *Phys. Rev. Lett.* **106**, 185003 (2011).
14. C. Dorrer, A. Consentino, D. Irwin, J. Qiao, and J. D. Zuegel, *J. Opt. A: Pure Appl. Opt.* **17**, 094007 (2015).
15. I. A. Begishev, C. R. Stillman, S. T. Ivancic, S.-W. Bahk, R. Cuffney, C. Mileham, P. M. Nilson, D. H. Froula, J. D. Zuegel, and J. Bromage, “Efficient Second-Harmonic Generation of Large-Aperture Multi-Terawatt Hybrid Nd: Laser Subpicosecond Pulses for Laser–Matter Interactions,” to be submitted to *Applied Physics*.
16. P. M. Nilson, J. R. Davies, W. Theobald, P. A. Jaanimagi, C. Mileham, R. K. Jungquist, C. Stoeckl, I. A. Begishev, A. A. Solodov, J. F. Myatt, J. D. Zuegel, T. C. Sangster, R. Betti, and D. D. Meyerhofer, *Phys. Rev. Lett.* **108**, 085002 (2012).
17. S. P. Regan, J. A. Delettrez, R. Epstein, P. A. Jaanimagi, B. Yaakobi, V. A. Smalyuk, F. J. Marshall, D. D. Meyerhofer, W. Seka, D. A. Haynes, Jr., I. E. Golovkin, and C. F. Hooper, Jr., *Phys. Plasmas* **9**, 1357 (2002).
18. J. M. Bañón and H. Nguyen, *J. Phys. B: At. Mol. Phys.* **20**, 2989 (1987).
19. K. Eidmann *et al.*, *J. Quant. Spectrosc. Radiat. Transf.* **81**, 133 (2003); P. Hakel *et al.*, *High Energy Density Phys.* **5**, 35 (2009).
20. U. Andiel *et al.*, *Europhys. Lett.* **60**, 861 (2002).
21. J. J. MacFarlane *et al.*, *High Energy Density Phys.* **3**, 181 (2007).
22. A. H. Gabriel and T. M. Paget, *J. Phys. B: At. Mol. Phys.* **5**, 673 (1972).
23. R. Shepherd *et al.*, *J. Quant. Spectrosc. Radiat. Transf.* **81**, 431 (2003).
24. J. J. MacFarlane *et al.*, *Proc. SPIE* **5751**, 588 (2005).
25. F. B. Rosmej, in *Handbook for Highly Charged Ion Spectroscopic Research*, edited by Y. Zou and R. Hutton (CRC, Boca Raton, FL, 2012), Part II, Chap. 12, pp. 267–342.
26. R. Cauble, *J. Quant. Spectrosc. Radiat. Transf.* **28**, 41 (1982); S. Skupsky, *Phys. Rev. A* **21**, 1316 (1980).
27. F. J. Rogers, H. C. Graboske, and D. J. Harwood, *Phys. Rev. A* **1**, 1577 (1970); S. Ichimaru, *Rev. Mod. Phys.* **54**, 1017 (1982); X. Li, Z. Xu, and F. B. Rosmej, *J. Phys. B: At. Mol. Opt. Phys.* **39**, 3373 (2006); X. Li and F. B. Rosmej, *Phys. Rev. A* **82**, 022503 (2010).
28. T. Nagayama *et al.*, *High Energy Density Phys.* **20**, 17 (2016).



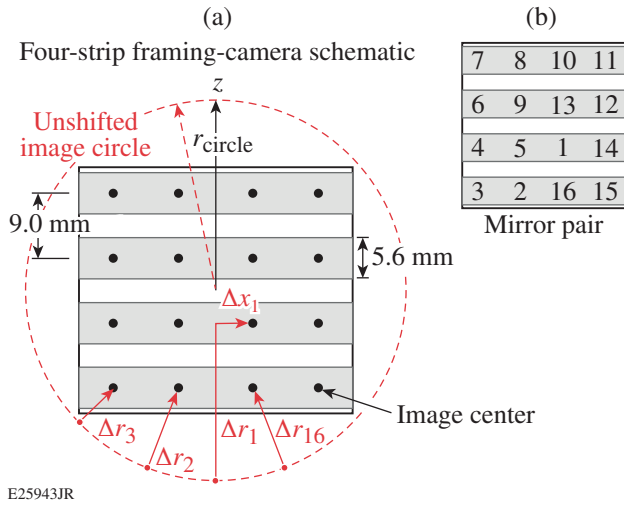


Figure 150.28 (a) Framing-camera image pattern and illustration of relocation of KB image to this pattern. (b) Mirror pair associated with each image location in (a).

this work, and the focus equation will be assumed to apply to the mirror pair, with the center of the pair taken as its location along the optic axis. For a given magnification  $M = q/p$ , the KB focus equation can be re-expressed as

$$q = \sqrt{M(M+1)R\delta x}, \quad (2)$$

where  $\delta x$  is the offset of a single mirror pair perpendicular to the  $z$  axis.

For untilted mirror pairs, the images fall on a circle  $r_{\text{circle}}$  given by

$$r_{\text{circle}} = \sqrt{2}\delta x(M-1). \quad (3)$$

The images of the ideal framing-camera pattern have three different offsets from the center of the pattern [Fig. 150.28(a)]. Four images are at the corners, eight images are on the sides, and four images are at the center of the pattern. The amounts

that a mirror pair must be moved,  $\Delta r_{\text{mirror}}$ , and tilted in pitch,  $\Delta\alpha_{\text{mirror}}$ , to move the image by  $\Delta r_{\text{image}}$  are given by

$$\Delta r_{\text{mirror}} = \Delta r_{\text{image}} / (M+1), \quad (4)$$

$$\Delta\alpha_{\text{mirror}} = \Delta r_{\text{image}} / p. \quad (5)$$

The parameters of the compact KB mirrors used in this work are given in Table 150.I. The angles  $\phi$  that the mirror pairs make with the axis of the framing camera and the mirror-pair positions and tilts that generate the pattern of image positions shown in Fig. 150.28(b) are provided in Table 150.II. Note that to move the inner images sideways, the mirrors must be tilted in roll  $\Delta\beta_{\text{mirror}}$  by an amount

$$\Delta\beta_{\text{mirror}} = \Delta x_{\text{image}} / 2q, \quad (6)$$

where  $\Delta x_{\text{image}}$  is the perpendicular amount to move the image. As an example,  $\Delta x_1$  is shown in Fig. 150.28(a).

The mirror-pair alignment is accomplished by placing the mirror-pair vertex at the offset positions given by the values in Table 150.II with preimposed tilts in pitch and roll. This was accomplished by using precision positioning stages and

Table 150.I: Parameters of compact mirrors used in the assembly of the KBFRAMED optic.

$R_{\text{KB}}$	27.5 m
$\Delta t$	4.5 mm
$\Delta x$	2.2 mm
$M$	12
$q$	2173.2 mm
$p$	181.0 mm
$r_{\text{circle}}$	34.22 mm
$i$	0.696°

Table 150.II: Mirror-pair offsets and tilts needed to generate the image locations in Fig. 150.28(a) with the pair assignments shown in Fig. 150.28(b). The remaining 12 pairs have common positions and tilts depending on image location as described in the text.

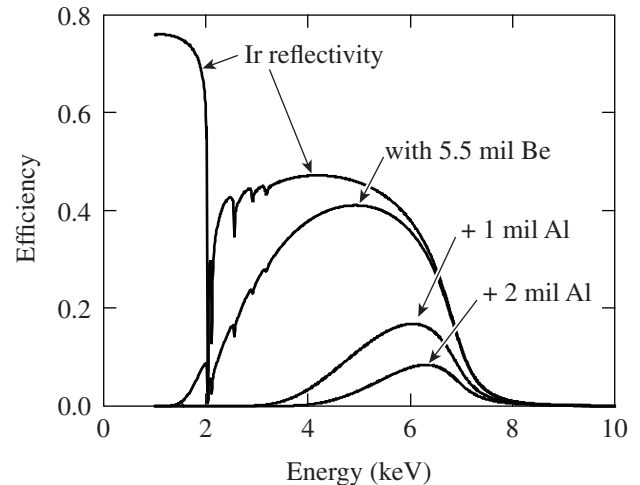
Mirror Pair	$\phi$ (°)	$r_{\text{image}}$ (mm)	$\Delta r_{\text{image}}$ (mm)	$\Delta r_{\text{mirror}}$ (mm)	$\Delta\alpha_{\text{pitch}}$ (°)	$\Delta\beta_{\text{roll}}$ (°)
16	-22.5	14.61	19.61	1.51	0.478	0
1	0	4.5	29.72	2.29	0.725	0.059
2	+22.5	14.61	19.61	1.51	0.478	0
3	+45	19.09	15.13	1.16	0.367	0

a rotary stage to position the base under a fixed, magnified viewing system (157 $\times$  on a video display). Assembled mirror pairs with pre-applied, UV-curable epoxy on the optic base side were held in place over the base with a vacuum chuck that was positioned by a six-axis positioner (three axes of position and three of tilt). In this fashion the mirrors were cured into place with the UV epoxy acting as the tilted interface to the flat optic base. Positioner accuracies were 1/10,000th of an inch (2.54  $\mu\text{m}$ ), 0.01 $^\circ$  in rotation of the optic base, and 2.36 arcsec in pitch and roll of the mirror pair.

All mirror-pair image positions were measured by placing the optic assembly in a vacuum system with a microscope chassis identical to that used with the framing camera and back-illuminating a grid co-aligned with the axis of the microscope ( $z$  axis) and at the focus distance for  $M = 12$  (181 mm) with an e-beam-generated x-ray source. Exposures were taken using a Fuji image plate and image positions determined to 0.1 mm. Any inaccuracies in image positions were minimized by removing the mirror pair and correcting the tilt angles in pitch and roll. Final accuracies of mirror-pair alignments were  $\sim 5 \mu\text{m}$  in position and  $\sim 20$  arcsec in pitch and roll. This resulted in all images being within 1 mm of the center of the ideal framing-camera cathode strip pattern (i.e., spaced by 9 mm vertically).

The resolution of the mirror pairs at best focus and the off-axis aberrations are discussed in detail in Ref. 13, and the resolution is calculated ideally to be better than  $\sim 5 \mu\text{m}$  over a 400- $\mu\text{m}$ -diam region around best focus. Tilting and repositioning the mirrors, ideally, avoids any additional blurring caused by misalignment from best focus; whereas, in practice, exact alignment is not possible and the framing camera will add additional blurring to the images. Therefore, it is better to determine the resolution by measurement. The inferred point-spread function (PSF), including blurring by the framing camera, is discussed in the next section.

The fused-silica compact KB mirror components are coated with 500  $\text{\AA}$  of Ir on top of a 150- $\text{\AA}$  Cr sticking layer as detailed in Ref. 13. The mean radius of curvature of the set of 32 mirrors used to assemble the 16 mirror pairs is 27.2 m, with a range from 25.6 to 28.6 m. The mirror pairs have radii of curvature that are typically within 0.1 m of each other. The x-ray reflectivity<sup>13</sup> of the mirrors has been measured to approach an ideal reflector at the grazing angle of 0.7 $^\circ$ . The typical sensitive energy band of the 16-image KB, calculated from the Henke-scattering factors,<sup>15</sup> is shown in Fig. 150.29, including the transmission of the blast shield, vacuum window, and example filters. The sensitive band extends from  $\sim 2$  keV to 8 keV.



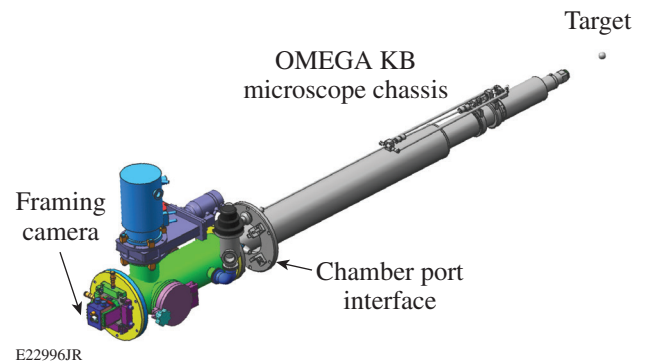
E25944JR

Figure 150.29

KB mirror-pair throughput efficiency including mirror-pair reflectivity, transmission of blast shield and vacuum window, and select filters.

### The KBFAMED Instrument

Figure 150.30 shows a schematic of the KBFAMED instrument. It consists of a chassis fixed in the OMEGA target chamber, the 16-image KB mirror assembly, and the vacuum interface to a high-speed framing camera.<sup>6</sup> The mirror assembly is held such that the mirror-pair centers are 181 mm from target chamber center, having been set to a precision of 10  $\mu\text{m}$  by a pointer placed on the optic cover when it was installed. A blast cover with holes aligned with the mirror-pair centers contains an x-ray-transparent Be foil that protects the mirrors from exposure to laser-generated target debris. A vacuum Be window separates the chamber vacuum from the path to the image plane, so a separate vacuum system provides a high vacuum ( $\sim 10^{-6}$  Torr) to the framing-camera active-detector



E22996JR

Figure 150.30

Schematic of the KBFAMED instrument.

region. This also isolates the camera from contaminants such as tritium from the targets. At present, the images are recorded on film that is not in the vacuum region of the framing camera, making it easy to exchange.

Figure 150.31 shows example images of a resolution grid taken by backlighting a grid placed at target chamber center by an Au foil placed 5 mm behind the grid. The foil is illuminated with 2 kJ of 351-nm UV light in a 1-ns pulse from six OMEGA beams. The grid (25.4- $\mu\text{m}$ -diam Cu wires, spaced by 50.8  $\mu\text{m}$ ) is placed on a Ta foil with a 500- $\mu\text{m}$ -diam hole, thereby producing 16 clearly separated images. The framing-camera images were recorded with Kodak T-MAX 3200 film and digitized on a calibrated PerkinElmer photo microdensitometer using 20- $\times$  20- $\mu\text{m}$  scan pixels. A step wedge was imposed on the film before exposure in the framing camera, which allowed the scanned film density to be converted to intensity.<sup>16</sup> The framing camera adds blurring to the images with a scale of  $\sim$ 50- $\mu\text{m}$  full width at half maximum (FWHM) at the image plane, (i.e.,  $\sim$ 5  $\mu\text{m}$  at the target plane). To estimate the effective blurring, a step pattern with the width and spacing of the Cu wires is convolved with a 2-D Gaussian blur function and then compared with the observed blurring. Figure 150.32 shows a lineout through a single intensity-corrected image taken through the central 200- $\mu\text{m}$ -wide region, averaged 10  $\mu\text{m}$  vertically to reduce noise. The measured pattern is compared to the Gaussian-blurred step pattern (dashed red curve) whose FWHM is 6  $\mu\text{m}$ . The close agreement indicates that the Gaussian blur function is a good approximation to the net blurring of the framed, KB mirror-pair images.

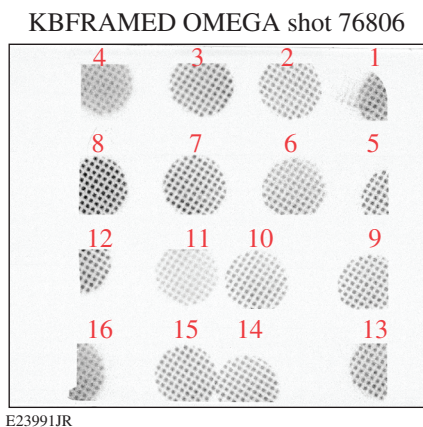


Figure 150.31  
Example framed images obtained with KBFRAMED of a backlit grid (25.4- $\mu\text{m}$ -diam Cu wires, spaced by 50.8  $\mu\text{m}$ ) taken with a high-speed framing camera.

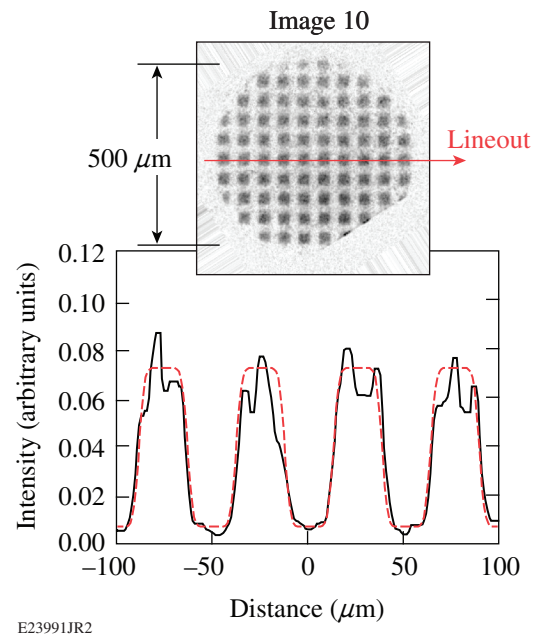


Figure 150.32

Lineout through a single framed, backlit image obtained with KBFRAMED (image 10 of Fig. 150.31). The lineout (solid curve) through the central 200  $\mu\text{m}$  is compared with an ideal grid pattern convolved with a 6- $\mu\text{m}$  FWHM Gaussian blur function (dashed red curve).

### Hot-Spot Evolution Imaged by KBFRAMED

KBFRAMED was developed principally to acquire time-resolved x-ray images of the cryogenic target implosion's stagnation region (i.e., hot spot). Triggering of the framing camera is accomplished by electrical delay using a reference to the master oscillator of the OMEGA laser that is accurate to the picosecond level. Since the hot spot evolves very quickly in time ( $\sim$ 100 ps), the framing-camera strip times are set to differ by 15 ps from strip to strip by using timed cables whose pulse propagation time differs by this amount (to within  $\pm$ 2 ps, measured to  $\pm$ 1 ps). The relative time of an image is determined from these delays and from the distance of the image from the beginning of the strip, assuming a pulse propagation speed of  $c/2$ . Deviations from the above assumptions caused by cross talk between neighboring strips are assumed to be small for these small offsets in pulse arrival times.<sup>17</sup> Absolute times can be assigned to data where the simultaneously measured time history of the neutron emission is measured by the neutron temporal diagnostic (NTD);<sup>18</sup> it is assumed that the x-ray and neutron emissions peak at the same time. Figure 150.33 shows example images of a cryogenic target's stagnation recorded by KBFRAMED with times so assigned from the beginning to the end of measurable core emission (the relative times are accurate to  $\sim$ 2 ps, whereas the absolute time may be in error

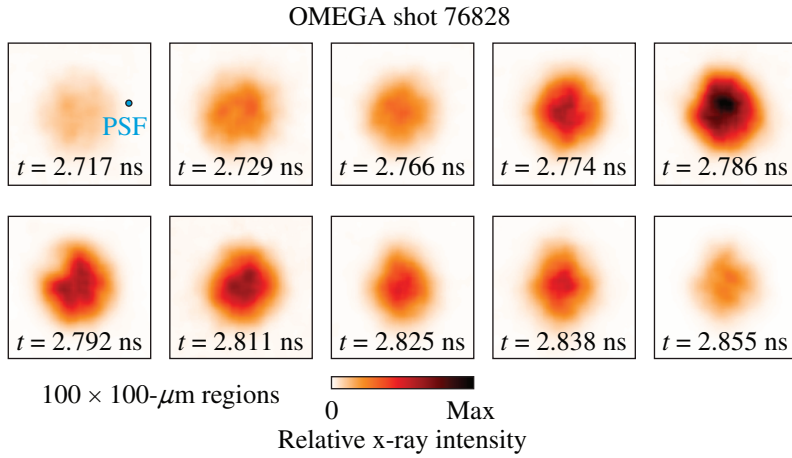


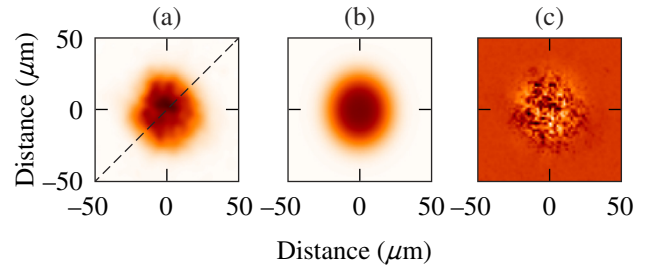
Figure 150.33  
KBFramed images of hot-spot x-ray emission from a cryogenic target implosion. The approximate point-spread function (PSF) (6- $\mu\text{m}$  FWHM Gaussian) is indicated by a circle of that size in the first image.

E24014aJR

by as much as  $\sim 50$  ps because of uncertainties in the time of the peak of the measured x-ray flux and the absolute timing of NTD). Image signal levels were adjusted for gain as a function of position on the strip determined from measurements of a uniformly illuminated x-ray-emitting foil observed with the same framing camera and the same strip timings. In this experiment an 8.8- $\mu\text{m}$ -thick deuterated polystyrene (CD) shell, 960  $\mu\text{m}$  in diam, filled with DT cryogenically cooled to form a 57- $\mu\text{m}$ -thick DT ice layer, was imploded with 29 kJ of UV (351 nm) from the 60 beams of the OMEGA Laser System,<sup>3</sup> using a triple-picket pulse, having a 1.5-ns-long main pulse.<sup>19</sup> The data were recorded with a 2-mil (50.8- $\mu\text{m}$ ) Al filter in front of the framing camera, so the energy band was  $\sim 4$  to 8 keV (see Fig. 150.29). The emission is seen to start as a low-intensity diffuse emission in a region of  $\sim 50$ - $\mu\text{m}$  diameter, brighten to a maximum in  $\sim 70$  ps, and then decrease over the next 70 ps. Inferences of hot-spot pressures are made from the size of the hot spot measured by KBFramed, the time of fusion burn, the measured ion temperature, and the measured neutron yield.<sup>20</sup> Without every one of these measurements, including the high-spatial-resolution framed images provided by KBFramed, the inferences of hot-spot pressure would not be possible. Additionally, the structure evident in the images at scales comparable to the PSF (6- $\mu\text{m}$  FWHM, as indicated by a circle of that size in Fig. 150.33) would not be observable without the resolution provided by KBFramed.

An example shape analysis of the hot-spot x-ray emission near the peak of the signal is shown in Fig. 150.34. The hot spot is first fit to a super-Gaussian ellipse convolved with the Gaussian point-spread function given by

$$I'(x,y) = \text{PSF}(x,y) \otimes I_0 \exp\left\{-\left[\left(x^*/a\right)^2 + \left(y^*/b\right)^2\right]^{\eta/2}\right\}, \quad (7)$$



E25945JR

Figure 150.34  
A single KBFramed cryogenic target hot-spot image at x-ray maximum: (a) image with dashed line indicating direction of lineout, (b) convolved, super-Gaussian-ellipse fit to image, and (c) difference between (a) and (b).

where  $\otimes$  denotes convolution,  $a$  and  $b$  are the lengths of the semi-major and semi-minor axes, respectively,  $I_0$  is the peak value, and  $\eta$  is the super-Gaussian order. The values  $x^*$  and  $y^*$  are the coordinates lying along the major and minor axes of the ellipse, given by

$$x^* = (x-x_c)\cos\alpha + (y-y_c)\sin\alpha, \quad (8)$$

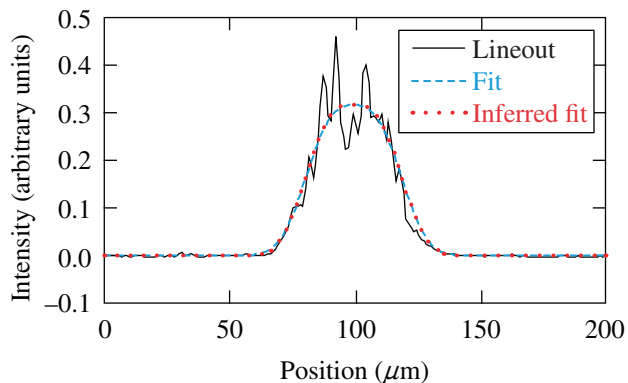
$$y^* = (x-x_c)\sin\alpha - (y-y_c)\cos\alpha,$$

where  $x$  and  $y$  are the coordinates in the image,  $\alpha$  is the phase angle to the major axis of the ellipse with respect to the  $x$  axis, and  $x_c$  and  $y_c$  are the locations of the center of the ellipse. Figure 150.34(a) shows the KBFramed image at the peak of the hot-spot emission. Figure 150.34(b) shows the best-fit, convolved super-Gaussian ellipse with  $a = 23.5 \mu\text{m}$ ,  $b = 20.9 \mu\text{m}$ ,  $\eta = 2.96$ ,  $I_0 = 0.32$ , and  $\alpha = 91.4^\circ$ . Figure 150.34(c) shows the difference, demonstrating that the fit accurately determines the size of the image with only small-scale structure and noise remaining. An example lineout through the image is shown in

Fig. 150.35 with the direction of the lineout indicated by the dashed line in Fig. 150.34(a). The need to use a fit is exemplified by the lineout, where it is evident that in order to estimate the average peak of the hot spot in the presence of noise in the image, it is necessary to use the best-fit value rather than a single peak value. The minimal difference in the convolved fitting function and the inferred super-Gaussian ellipse is because the emission is well resolved by the given resolution of KBFramED for this hot-spot size. However, since this method makes it possible to compare sizes when measured with differing resolutions, it is the preferred procedure. With the peak of the hot spot so defined, the size of the hot spot is then defined by the convention that the hot-spot radius is given by the average radius where the emission is 17% of the maximum.<sup>21</sup> With this definition,  $r_{17}$  is given by

$$r_{17} = (-\ln 0.17)^{1/\eta} r_0, \tag{9}$$

where  $r_0$  is the geometric mean of  $a$  and  $b$  ( $r_0 = \sqrt{ab}$ ). For the image above,  $r_{17}$  is found to be 26.9  $\mu\text{m}$ .



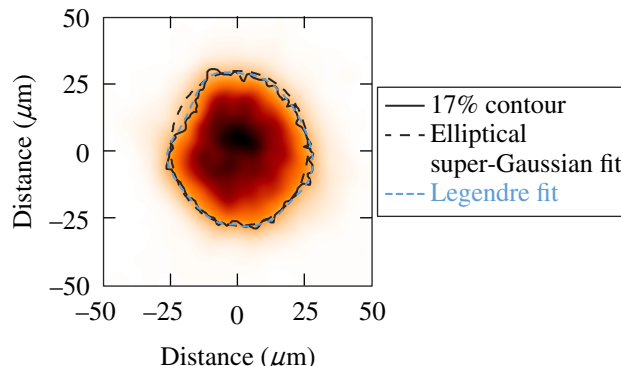
E25946JR

Figure 150.35

Lineout through image in Fig. 150.34(a) and through the convolved super-Gaussian ellipse fit to that image (fit) and through the unconvolved fit (inferred fit).

A more-detailed fit to the hot-spot envelope is determined by fitting the contour of the image at 17% of the fit peak to a Legendre polynomial with the axis of the fit taken as the semi-major axis of the super-Gaussian fit. Figure 150.36 shows the 17% contour, the Legendre fit to the contour (the two sides of the image are separately fit with the major axis of the super-Gaussian fit defining the sides), and the super-Gaussian-fit 17% contour on the image of Fig. 150.34(a). The fractional-radial deviation (departure from a circle) of the contours as a function of angle from the semi-major axis is plotted in Fig. 150.37. The Legendre modes of the fit are shown in Fig. 150.38 for modes

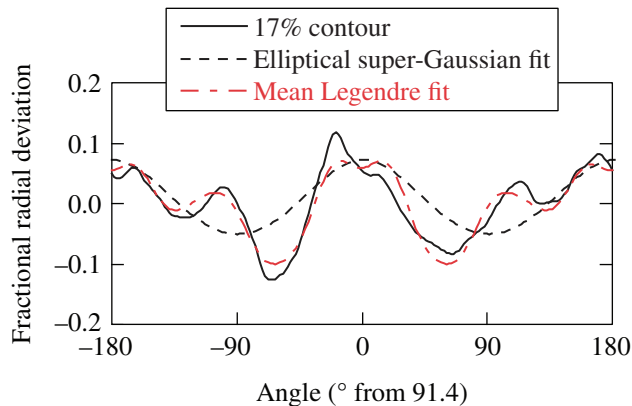
from 2 to 10 (mode 1 is just a shift of the center) with the value taken as the average of the fits to the two sides of the contour and the error bar defined by the minimum and maximum of



E25947JR

Figure 150.36

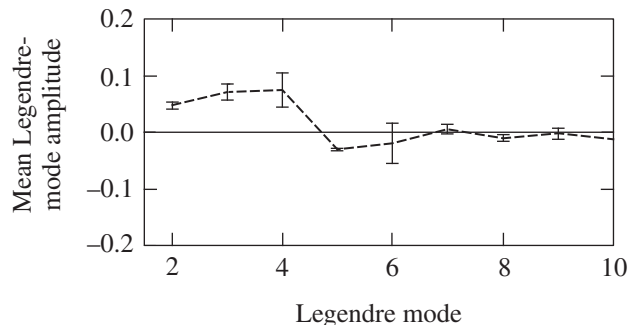
Single KBFramED image from Fig. 150.34(a) with  $r_{17}$  contours superposed.



E25948JR

Figure 150.37

Fractional-radial deviation of  $r_{17}$  contours from Fig. 150.36 as a function of the angle from the semi-major axis of the super-Gaussian-ellipse fit.



E25949JR

Figure 150.38

Legendre-mode spectrum of the fit to the measured  $r_{17}$  contour in Fig. 150.36.

those two fits. The Legendre fit to the hot-spot envelope at  $r_{17}$  is, as expected, closer to the observed shape, although the average radius differs only slightly from the elliptical fit ( $26.7\ \mu\text{m}$  for the observed and Legendre fit as opposed to  $26.9\ \mu\text{m}$  for the elliptical fit). In this particular image, modes 2 through 5 are significant although all are less than 0.1 (i.e., less than 10%), whereas modes 6 through 10 are less than  $\sim 2\%$ . Note that with an emission region of this radius, mode 10 is expected to be suppressed by the resolution of the instrument by approximately a factor of 2, i.e., the true limit for mode 10 is less than  $\sim 4\%$  for an observed limit of  $\sim 2\%$ .

The dominant modes of the hot-spot envelope are those expected from on-target illumination nonuniformities coming from beam-intensity imbalance,<sup>22</sup> but this observation does not determine that they are the source of the perturbations. Also, it is important to note that the major axis of the ellipse is within  $2^\circ$  of the vertical ( $91.4^\circ$  best fit), which is approximately parallel to the direction of the stalk that holds the cryogenic target in place in the OMEGA target chamber (KBFRAMED is located  $10^\circ$  below the equator of the OMEGA chamber and the stalk direction is downward in the images). The stalk and the glue spot that binds the stalk to the CD shell that surrounds the DT ice layer are known to be the largest mass perturbation at the surface of the target. The effect of a stalk is complex in nature<sup>23</sup> but, simply put, it causes the hot spot to become elongated in the direction of the stalk. This example serves to illustrate the benefit of the increased resolution of the KBFRAMED instrument and the type of information that can be obtained from these images.

## Conclusions

A novel 16-image KB microscope design that couples to a high-speed framing camera has been implemented on the OMEGA Laser System. This instrument, known as KBFRAMED, obtains framed images of x-ray emission from laser-generated plasmas with  $\sim 6\text{-}\mu\text{m}$  spatial resolution,  $\sim 30\text{-ps}$  time resolution over a region of  $\sim 400\ \mu\text{m}$  in the energy band from 2 to 8 keV. It was specifically designed to measure the stagnation region (hot spot) of cryogenically cooled DT target implosions that have typical sizes of  $\sim 60\text{-}\mu\text{m}$  diameter and durations of  $\sim 100\ \text{ps}$ . The spatial resolution and time sampling of KBFRAMED allow one to measure the time-varying size and shape of these hot spots.

## ACKNOWLEDGMENT

The authors acknowledge the support of the staff at the University of Rochester's Laboratory for Laser Energetics and of the Omega Laser Facility. This material is based on work supported by the Department of Energy National

Nuclear Security Administration under Award Number DE-NA0001944, the University of Rochester, and the New York State Energy Research and Development Authority.

## REFERENCES

1. P. Kirkpatrick and A. V. Baez, *J. Opt. Soc. Am.* **38**, 766 (1948).
2. J. F. McGee and J. W. Burrows, *Proc. SPIE* **106**, 107 (1977).
3. T. R. Boehly, D. L. Brown, R. S. Craxton, R. L. Keck, J. P. Knauer, J. H. Kelly, T. J. Kessler, S. A. Kumpan, S. J. Loucks, S. A. Letzring, F. J. Marshall, R. L. McCrory, S. F. B. Morse, W. Seka, J. M. Soures, and C. P. Verdon, *Opt. Commun.* **133**, 495 (1997).
4. M. C. Richardson *et al.*, *IEEE J. Quantum Electron.* **QE-19**, 1861 (1983).
5. F. J. Marshall, M. M. Allen, J. P. Knauer, J. A. Oertel, and T. Archuleta, *Phys. Plasmas* **5**, 1118 (1998).
6. D. K. Bradley *et al.*, *Rev. Sci. Instrum.* **66**, 716 (1995).
7. F. J. Marshall and P. B. Radha, *Rev. Sci. Instrum.* **85**, 11E615 (2014).
8. F. J. Marshall and J. A. Oertel, *Rev. Sci. Instrum.* **68**, 735 (1997).
9. L. A. Pickworth *et al.*, *Rev. Sci. Instrum.* **85**, 11D611 (2014).
10. E. I. Moses *et al.*, *Phys. Plasmas* **16**, 041006 (2009).
11. S. Yi *et al.*, *Rev. Sci. Instrum.* **87**, 103501 (2016).
12. F. J. Marshall, J. A. Oertel, and P. J. Walsh, *Rev. Sci. Instrum.* **75**, 4045 (2004).
13. F. J. Marshall, *Rev. Sci. Instrum.* **83**, 10E518 (2012).
14. F. J. Marshall and Q. Su, *Rev. Sci. Instrum.* **66**, 725 (1995).
15. B. L. Henke, E. M. Gullikson, and J. C. Davis, *At. Data Nucl. Data Tables* **54**, 181 (1993).
16. J. P. Knauer, R. Betti, D. K. Bradley, T. R. Boehly, T. J. B. Collins, V. N. Goncharov, P. W. McKenty, D. D. Meyerhofer, V. A. Smalyuk, C. P. Verdon, S. G. Glendinning, D. H. Kalantar, and R. G. Watt, *Phys. Plasmas* **7**, 338 (2000).
17. L. R. Benedetti *et al.*, *Rev. Sci. Instrum.* **83**, 10E135 (2012).
18. C. Stoeckl, R. Boni, F. Ehrne, C. J. Forrest, V. Yu. Glebov, J. Katz, D. J. Lonobile, J. Magoon, S. P. Regan, M. J. Shoup III, A. Sorce, C. Sorce, T. C. Sangster, and D. Weiner, *Rev. Sci. Instrum.* **87**, 053501 (2016).
19. P. B. Radha, J. A. Marozas, F. J. Marshall, A. Shvydky, T. J. B. Collins, V. N. Goncharov, R. L. McCrory, P. W. McKenty, D. D. Meyerhofer, T. C. Sangster, and S. Skupsky, *Phys. Plasmas* **19**, 082704 (2012).
20. S. P. Regan, V. N. Goncharov, I. V. Igumenshchev, T. C. Sangster, R. Betti, A. Bose, T. R. Boehly, M. J. Bonino, E. M. Campbell, D. Cao, T. J. B. Collins, R. S. Craxton, A. K. Davis, J. A. Delettrez, D. H. Edgell, R. Epstein, C. J. Forrest, J. A. Frenje, D. H. Froula, M. Gatu Johnson, V. Yu. Glebov, D. R. Harding, M. Hohenberger, S. X. Hu, D. Jacobs-

- Perkins, R. T. Janezic, M. Karasik, R. L. Keck, J. H. Kelly, T. J. Kessler, J. P. Knauer, T. Z. Kosc, S. J. Loucks, J. A. Marozas, F. J. Marshall, R. L. McCrory, P. W. McKenty, D. D. Meyerhofer, D. T. Michel, J. F. Myatt, S. P. Obenshain, R. D. Petrasso, R. B. Radha, B. Rice, M. Rosenberg, A. J. Schmitt, M. J. Schmitt, W. Seka, W. T. Shmayda, M. J. Shoup, III, A. Shvydky, S. Skupsky, A. A. Solodov, C. Stoeckl, W. Theobald, J. Ulreich, M. D. Wittman, K. M. Woo, B. Yaakobi, and J. D. Zuegel, *Phys. Rev. Lett.* **117**, 025001 (2016); **117**, 059903(E) (2016).
21. C. Cerjan, P. T. Springer, and S. M. Sepke, *Phys. Plasmas* **20**, 056319 (2013).
22. F. J. Marshall, J. A. Delettrez, R. Epstein, R. Forties, R. L. Keck, J. H. Kelly, P. W. McKenty, S. P. Regan, and L. J. Waxer, *Phys. Plasmas* **11**, 251 (2004).
23. I. V. Igumenshchev, F. J. Marshall, J. A. Marozas, V. A. Smalyuk, R. Epstein, V. N. Goncharov, T. J. B. Collins, T. C. Sangster, and S. Skupsky, *Phys. Plasmas* **16**, 082701 (2009).

---

# Modeling Tritium Interactions with Metals

## Introduction

Quantitatively modeling the interaction of tritium with metals is a vital step toward understanding the mechanisms of tritium migration through the metal. In turn, understanding these fundamental mechanisms is necessary to interpret experimental results and to make accurate predictions regarding tritium migration in metals during exposures to tritium gas and subsequent storage periods and/or cleaning procedures. While the literature contains several attempts at creating a quantitative model,<sup>1–4</sup> each attempt lacks one fundamental aspect: tritium migration across the surface–metal lattice interface. Many reports in the literature show that tritium adsorbs onto the surface as tritiated water,<sup>1,5,6</sup> while tritium absorbs into the metal lattice as atomic tritium.<sup>5</sup> This difference in retention media results in the measured large differences in tritium concentrations in the surface and in the bulk metal.<sup>7</sup> Including this physical condition into a quantitative model is necessary to accurately model the complete tritium–metal system.

In this article, we present a quantitative tritium migration model (QTRIMM) for modeling tritium migration in various metal substrates. This model includes the surface film of adsorbed water and relates the concentrations of tritium within the thin film of adsorbed water to the tritium concentrations within the substrate metal. Additionally, the tritium concentrations throughout the metal sample are output from the model calculation. Currently, this information is obtained experimentally only through acid etching or other destructive techniques. The model developed in this work provides two major advantages. First, inclusion of the thin film of adsorbed water in the model provides the first step toward a global model, capable of describing all experimental conditions. Second, because the tritium concentration profiles throughout the sample are calculated, the model has the potential to predict the location of tritium within a metal using only the loading and storage conditions. This avoids the necessity of destructive techniques to determine the tritium concentration profiles. Further, the model can be used to calculate the increase in gas-phase protium concentrations in a mixture of deuterium and tritium.

In this article the physical picture of a metal's surface is presented first, along with the primary assumptions and the relevant equations. Following this, a detailed derivation of the model is included. This derivation is divided into two major parts: bulk migration and surface conditions. To model tritium migration in the bulk metal lattice, Fick's second law of diffusion is solved numerically. This solution includes a condition for tritium diffusion through composite media. Next, the surface boundary conditions used to model tritium migration during an exposure to tritium gas and during a subsequent storage period are presented. Finally, a few predictions are made by using QTRIMM.

## Surface–Metal Interface Condition

Tritium interacts with metal substrates by first adsorbing onto the metal surface and then permeating through the metal lattice. Under most conditions, tritium does not adsorb directly onto the metal's surface. Instead, the tritons adsorb in the form of tritiated light water (HTO).<sup>1,5,6</sup> After adsorption onto the surface, tritium can migrate from the water layers into the bulk metal lattice. The tritons occupy interstitial locations and defect sites within the metal's crystal lattice and diffuse through the lattice by migrating between the various sites. This process is illustrated in Fig. 150.39. Here, the approximate thickness of both the water layers and the metal oxide layers are shown for reference. The remainder of this section will address the tritium migration mechanisms treated in QTRIMM and will discuss the major assumptions of the model.

The first step in the tritium permeation process is adsorption onto the metal surface. This process presumably occurs through isotope exchange between tritiated species in the gas phase and water molecules adsorbed on the metal surface.<sup>6</sup> This exchange process is expected to occur rapidly, relative to tritium migration into the underlying metal lattice. Assumption of rapid equilibrium across the surface–gas interface is justified by comparing the flux of gaseous tritium to the surface and the diffusive flux of tritium into the metal lattice.<sup>8</sup> Additionally, the average residence time of adsorbed species is of the order of femtoseconds at 25°C.

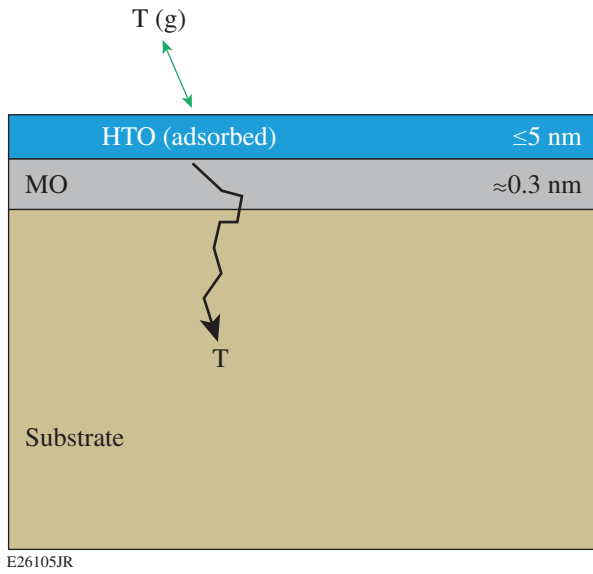


Figure 150.39  
Illustration of tritium adsorption and migration into a metal sample. The adsorbed water layers and metal oxide (MO) layers are depicted on the surface of a metal substrate.

Rapid equilibrium across the surface–gas interface makes it possible to determine the surface concentration of tritium. At equilibrium, the surface concentration of tritium is related to the concentration of tritium within the gas phase

$$\chi_{\text{surf}}^{\text{eq}} = f * \chi_{\text{gas}}^{\text{eq}} \quad (1)$$

In this formula, the mole fraction of tritium on the surface ( $\chi_{\text{surf}}^{\text{eq}}$ ) is related to the mole fraction of tritium in the gas phase ( $\chi_{\text{gas}}^{\text{eq}}$ ) by a constant factor ( $f$ ). This factor accounts for various isotope exchange probabilities. In the limiting case of equal exchange probabilities, the scaling factor is unity. In reality, it is likely that the formation of double-isotope species, such as  $\text{T}_2\text{O}$ , is not as probable as the formation of mixed isotope species of water, such as HTO or DTO (tritiated heavy water). This more-realistic scenario of nonequal reaction probabilities would reduce the scaling factor to a fractional value ranging between zero and unity. For simplicity, we take  $f = 1$  in our calculations.

Using the above relation between the mole fractions in the two phases makes it possible to determine the absolute concentration of tritium in the adsorbed water layers. Assuming the density of these water layers does not change significantly with each successive layer, the concentration of tritium on the metal's surface is given by

$$c_{\text{surf}}^{\text{eq}} = \frac{\chi_{\text{gas}}^{\text{eq}} * f * \rho_{\text{H}_2\text{O}}}{\delta_{\text{ML}}} * \frac{2 \text{ mol H}}{\text{mol H}_2\text{O}} \quad (2)$$

Here, the concentration of tritium ( $c_{\text{surf}}^{\text{eq}}$ ) is determined by the mole fraction of tritium in the gas phase ( $\chi_{\text{gas}}^{\text{eq}}$ ), the isotope exchange scaling factor ( $f$ ), the surface density of water ( $\rho_{\text{H}_2\text{O}}$ ), and the thickness of a monolayer of water ( $\delta_{\text{ML}}$ ). An additional factor of 2 is included to relate the number of moles of hydrogen to the moles of water on the surface. In the limit of  $f = 1$ ,  $c_{\text{surf}}^{\text{eq}}$  is taken to be equal to a saturated surface solubility  $S_{\text{surf}}$ . Under the assumptions of rapid equilibrium and a static gas phase, the equilibrium surface concentration in Eq. (2) remains constant throughout an exposure to tritium gas. In a situation where the fraction of tritium in the gas phase changes, the surface concentration will rapidly adjust to the new conditions.

After adsorption onto the surface, tritium can then permeate through the metal lattice by diffusing from site to site within the lattice. Permeation through the lattice begins with the triton crossing the surface–metal lattice interface. Migration across this interface is also assumed to be much faster than the rate of tritium diffusion in the underlying metal substrate. As such, the chemical potentials of tritium dissolved on either side of the interface are equal at the interface:

$$\mu_{\text{surf}}(x_I) = \mu_{\text{metal}}(x_I) \quad (3)$$

where  $\mu_{\text{surf}}$  and  $\mu_{\text{metal}}$  are the chemical potentials in the adsorbed water layers and the metal lattice, respectively, and  $x_I$  represents the position of the interface. This equality leads to a relation between the concentrations of tritium within each region:

$$\frac{c_{\text{surf}}^{\text{eq}}(x_I)}{c_{\text{metal}}^{\text{eq}}(x_I)} = \exp\left(-\frac{\mu_{\text{surf}}^* - \mu_{\text{metal}}^*}{RT}\right) \quad (4)$$

This equation states that the ratio between the equilibrium concentrations in each region ( $c^{\text{eq}}$ ) depends on the standard chemical potentials in each region ( $\mu^*$ ), the gas constant ( $R$ ), and the temperature ( $T$ ). In a complete description of solute migration across an interface, the standard chemical potentials can vary from point to point as a function of depth. Varying standard potentials may result in gradual changes in the potential, culminating with equal standard potentials at the interface. Equal standard potentials result in equal concentrations at the

interface and therefore in a continuous solute concentration profile across the interface region. Including spatially variable standard chemical potentials may not be necessary since some physical situations can be modeled well with the simplified approach of constant chemical potentials.<sup>9</sup> Physical situations like this may be the result of well-defined boundaries between phases, similar to the interface between two solids. In these situations, the standard potential changes over a small distance are small and the equilibrium tritium concentrations at the interface are related by a constant factor.

The constant factor relating the tritium concentrations at the interface can be obtained by using Sievert's law, where the ratio of the tritium concentrations given by Eq. (4) is equal to the ratio of the solubilities of tritium in each region ( $S_i$ ), assuming the partial pressure of tritium at the interface is a constant:

$$\frac{c_{\text{surf}}^{\text{eq}}}{c_{\text{metal}}^{\text{eq}}} = \frac{S_{\text{surf}}}{S_{\text{metal}}}. \quad (5)$$

This equation makes it possible to determine the tritium concentration in the metal lattice, given a tritium concentration on the surface. In order for the equality shown in Eq. (5) to hold, the metal lattice concentration must be multiplied by the isotope exchange scaling factor [Eq. (1)]:

$$\frac{c_{\text{surf}}^{\text{eq}}(f)}{f * c_{\text{metal}}^{\text{eq}}} = \frac{S_{\text{surf}}}{S_{\text{metal}}}. \quad (6)$$

For a constant temperature, the ratio of tritium solubilities in each region is a constant. Therefore, if the isotope exchange scaling factor is less than unity, the surface concentration will decrease, which means the concentration in the metal lattice must also decrease by the same factor.

This formalism for tritium migration across a boundary applies not only to transport across the adsorbed water–metal lattice interface but to any well-defined interface. One can extend Eqs. (3)–(6) to other composite media such as gold-plated metals or to metal substrates with artificially grown metal oxide layers, for example.

The final step toward describing tritium permeation is tritium diffusion through the metal lattice. For simplicity, we treat only lattice diffusion and ignore pathways such as grain boundaries and triple junctions and trap sites such as disloca-

tions and vacancies. While these can be notable defects, the majority of the dissolved tritium is expected to migrate through the interstitial lattice sites in well-behaved metals with negligible contributions from defect sites.

### Modeling Tritium Migration in the Bulk Metal Lattice

A model based on Fickian diffusion of tritium through the metal lattice has been developed. This model numerically solves for the tritium concentrations throughout a metal and includes a condition for solute diffusion through different, but interacting media, as outlined in the previous section. The numeric solution uses an intermediate time step and divides the solid into  $N$  cells. For simplicity, the model uses a one-dimensional solution. The quantity of solute in each cell can be determined by multiplying the cell thickness ( $\Delta x$ ) with the surface area of the sample used in an experiment.

The concentration in each cell  $c$  is determined from a flux balance of tritium entering and leaving each cell. Because of this, the flux  $F$  is calculated at the intermediate positions,  $i \pm 1/2$  as shown in Fig. 150.40. The rate of change in the solute concentration in each cell is determined by relating Fick's First and Second Laws to yield

$$\frac{\partial c}{\partial t} = -\frac{\partial F}{\partial x}. \quad (7)$$

The finite-difference fluxes at the intermediate positions are

$$F_{i+1/2} = -D_{i+1/2} \left( \frac{c_{i+1} - c_i}{x_{i+1} - x_i} \right), \quad (8)$$

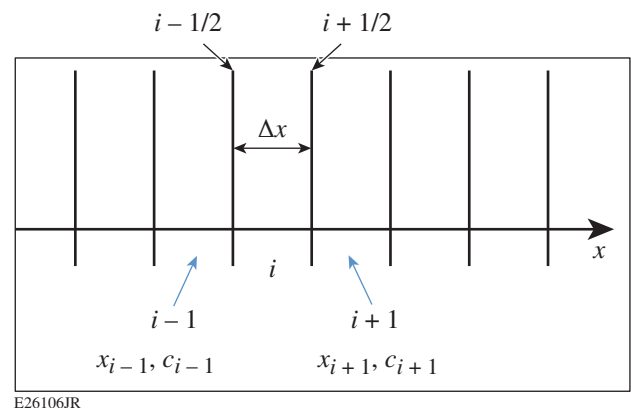


Figure 150.40  
Division of solid into equally spaced cells.

$$F_{i-1/2} = -D_{i-1/2} \left( \frac{c_i - c_{i-1}}{x_i - x_{i-1}} \right), \quad (9)$$

where  $D$  is the diffusivity. Using Eqs. (7)–(10), the rate of change of the concentration in cell “ $i$ ” is written as

$$\frac{c'_i - c_i}{\Delta t} = -\theta \frac{(F'_{i+1/2} - F'_{i-1/2})}{\Delta x_i} - \frac{(1-\theta)(F_{i+1/2} - F_{i-1/2})}{\Delta x_i}, \quad (10)$$

where the primes denote the next time step and  $\theta$  is the degree of implicitness, which determines the degree of accuracy and stability;  $\theta = 0.5$  provides the highest accuracy, while  $\theta > 0.5$  enhances stability.

Equations (7)–(10) represent the basis for QTRIMM. Using these equations, a system of linear equations is obtained. Each equation in the set gives the concentration at the next time step for a particular location within the metal. Two additional equations are necessary to solve for the boundary conditions. These equations occur at indices of  $i = 0$  and  $i = N$  and will be discussed later. The total set of equations has one degree of freedom, allowing the system of equations to be solved exactly. Coupling Eq. (10) with a set of boundary conditions makes it possible to calculate the tritium concentrations in a homogeneous solid.

Tritium diffusion across an interface between two media requires that the flux equations [Eqs. (8) and (9)] be constrained. These fluxes must be modified to maintain a constant ratio of the tritium solubilities across the interface [Eq. (5)]. The other implicit condition is that the total quantity of tritium throughout the system must be conserved. Using these conditions, the equations for the modified boundary conditions can be derived.

To maintain mass balance throughout the system, the concentration at the interface must be given by the rate of solute entering and exiting the cell, i.e., we require flux balance. In the present diffusion model, the interface between two well-defined solvents is placed within one cell ( $i = M$ ) in the discretized solid. The concentration at the interface position is then given by the average of the concentrations on the right ( $c_M^R$ ) and left ( $c_M^L$ ) sides of the cell because half of this cell is one solvent and half is the other:

$$c_M = \frac{(c_M^R + c_M^L)}{2}. \quad (11)$$

Combining Eqs. (5) and (11) yields

$$c_M^R = \left( \frac{2}{S_R + 1} \right) c_M = \varphi_R * c_M. \quad (12)$$

Similarly,

$$c_M^L = \left( \frac{2 * S_R}{S_R + 1} \right) c_M = \varphi_L * c_M. \quad (13)$$

The flux in and out of the interface cell must utilize  $c_M^L$  and  $c_M^R$ ...

$$\begin{aligned} F_{M+1/2} &= -D_{M+1/2} * \left( \frac{c_{M+1} - c_M^R}{x_{M+1} - x_M} \right) \\ &= -D_{M+1/2} * \left( \frac{c_{M+1} - \varphi_R * c_M}{x_{M+1} - x_M} \right), \end{aligned} \quad (14)$$

$$\begin{aligned} F_{M-1/2} &= -D_{M-1/2} * \left( \frac{c_M^L - c_{M-1}}{x_M - x_{M-1}} \right) \\ &= -D_{M-1/2} * \left( \frac{\varphi_L * c_M - c_{M-1}}{x_M - x_{M-1}} \right). \end{aligned} \quad (15)$$

Equations (14) and (15) can be inserted into Eq. (10) to determine the concentrations around the interface ( $i = M-1, M, M+1$ ). These equations apply only around the interface position; the remaining equations are unchanged from the form derived for a homogeneous solid.

To solve for the concentration profiles in a metal sample, two equations for the boundary conditions are necessary. For the first boundary condition, we assume a symmetric solid. Under this assumption, the diffusion model must extend only to the center of the sample; the other side of the sample is a mirror image. To solve for the concentration at the centerline, we set the fluxes into or out of this cell to be equal but with opposite signs to reflect the opposite directions of flow. The boundary condition for the sample's surface depends on the experimental conditions. Two general cases are outlined in the following section: the first case treats a storage condition where tritium is allowed to redistribute throughout the solid as well as to desorb from the surface; the second case treats a

condition where a metal is exposed to gaseous tritium and is loaded with tritium.

### Boundary Conditions at the Metal's Surface

We utilize slightly different surface boundary conditions, depending on whether the model calculates the concentration profiles during the loading phase or during a storage phase. During the loading phase, the surface concentration is assumed to be constant. During the storage phase, this concentration is allowed to vary because tritium is allowed to migrate into the metal lattice and to desorb from the surface at a constant rate. The derivations for these two conditions are shown below.

In all cases, multiple monolayers of adsorbed water develop on all metal surfaces that have been exposed to a humid atmosphere. These layers are distinct from the bulk metal and have a much higher solubility for tritium. To model tritium migrating from the bulk metal into the surface, the interface equations outlined in the previous section are used. Assuming that a rapid equilibrium develops across the surface–metal lattice interface, the concentrations on either side of the interface are related by the ratio of the solubilities for tritium in each region, as presented in Eq. (5).

The thickness of the metal substrate is much larger than the thickness of the adsorbed water layer as illustrated in Fig. 150.39. To account for this significant difference in thickness and to reduce the calculation time, two different cell sizes are used: one to calculate the concentrations in the bulk of the sample ( $\Delta x$ ) and the other to calculate the surface concentration ( $\delta x$ ). Given the small thickness of the water layer and the relatively slow rate of diffusion into the metal lattice, tritium concentrations likely equilibrate rapidly in the water layers relative to the bulk metal. Assuming this rapid equilibration and using the small water-layer thickness, the surface–metal interface is placed entirely in the first cell ( $i = 0$ ) of the discretized solid as shown in Fig. 150.41. The thickness of the surface cell ( $i = 0$ ) is determined by the surface concentration of adsorbed water ( $Q$ ), the surface density of water ( $\rho_{\text{H}_2\text{O}}$ ), and the thickness of a monolayer of water ( $\delta_{\text{ML}}$ ):

$$\delta x = \frac{Q}{\rho_{\text{H}_2\text{O}}} * \delta_{\text{ML}} * 2. \quad (16)$$

The factor of 2 in this equation scales up the thickness of this cell to account for the fact that half of this cell is adsorbed water and half is the bulk metal lattice (Fig. 150.41).

For the loading phase, the surface concentration is assumed to remain constant in time. To incorporate this fixed concen-

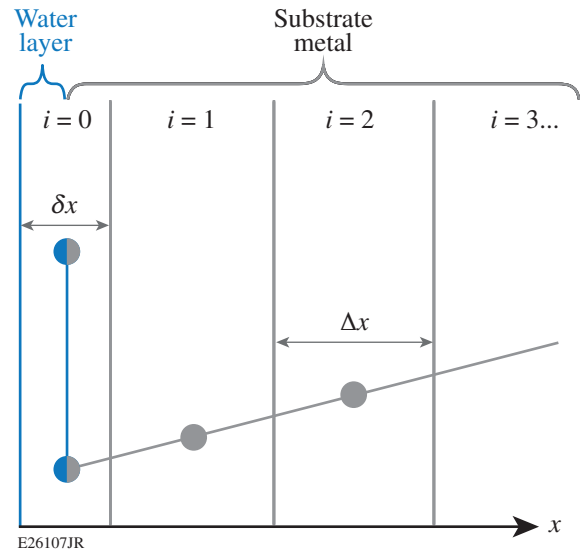


Figure 150.41  
Illustration showing the position of the surface–metal lattice interface.

tration into the solution matrix, we assume a linear relation between the concentrations in the first three cells:

$$\frac{c'_1 - c_0 \phi_R}{x_1 - x_0} = \frac{c'_2 - c_0 \phi_R}{x_2 - x_0}. \quad (17)$$

This equation follows the same form as Eq. (10) and can be inserted directly into the system of equations defined by Eq. (10).

During the storage phase, the tritium concentrations in the surface cell ( $i = 0$ ) are allowed to vary by including two conditions for tritium transport: diffusion into the metal and desorption from the surface. Following the same formalism shown above, we define the diffusive flux into the metal lattice as

$$F_{1/2} = -D * \left( \frac{c_1 - c_0 * \phi_R}{x_1 - x_0} \right). \quad (18)$$

The desorbing flux away from the surface is defined by

$$F_{-1/2} = -\nu * c_0 * \phi_L \left( \frac{\delta x}{2} \right), \quad (19)$$

where  $\nu$  is the desorption rate constant. The return flux from the atmosphere to the surface is ignored in the equation because the airborne concentration is assumed to be negligible. The

thickness of the surface cell,  $\delta x$ , is divided in half since half of this cell represents the adsorbed water layers illustrated in Fig. 150.41. The desorption rate constant  $\nu$  determines the rate at which tritium desorbs from the surface. Surette and McElroy measured this rate to be 0.91% per day for untreated stainless-steel surfaces.<sup>10</sup> This is equivalent to  $10^{-7}$  tritons desorbing per second, which is the value used in the following calculations. Equations (18) and (19) can be inserted into Eq. (10) to yield the surface boundary condition in the diffusion model.

### Model Predictions

Using the model outlined in the previous sections, we can predict the migration of tritium through a metal sample during an exposure to tritium gas, a subsequent storage period, and a decontamination procedure. The results of a series of simulations are presented in Figs. 150.42–150.44, which show the consequences of exposing stainless steel to tritium gas and then storing the metal for a period of time.

Table 150.III lists the hydrogen diffusivity in stainless steel, copper, and aluminum;<sup>11</sup> Table 150.IV lists the solubilities for these materials.<sup>11</sup> Figure 150.42 shows the calculated tritium concentration profiles that develop within a stainless steel sample, exposed to 612 Torr of hydrogen gas containing 60% tritium for 24 h. Initially, the surface concentration was fixed at the value shown, while the remaining concentrations in the metal were set to zero. The profiles are plotted in increments of 1 h. For clarity, only the concentrations within the metal

Table 150.III: Hydrogen diffusivity in select materials.

	Stainless steel	Copper	Aluminum
Frequency factor (m <sup>2</sup> /s)	$7.2 \times 10^{-7}$	$7.9 \times 10^{-7}$	$1.46 \times 10^{-6}$
Activation energy (kJ/mol)	52.9	38.6	30.0
Diffusivity at 25°C (m <sup>2</sup> /s)	$4.1 \times 10^{-16}$	$1.4 \times 10^{-13}$	$5.0 \times 10^{-12}$

Table 150.IV: Hydrogen solubility in select materials.

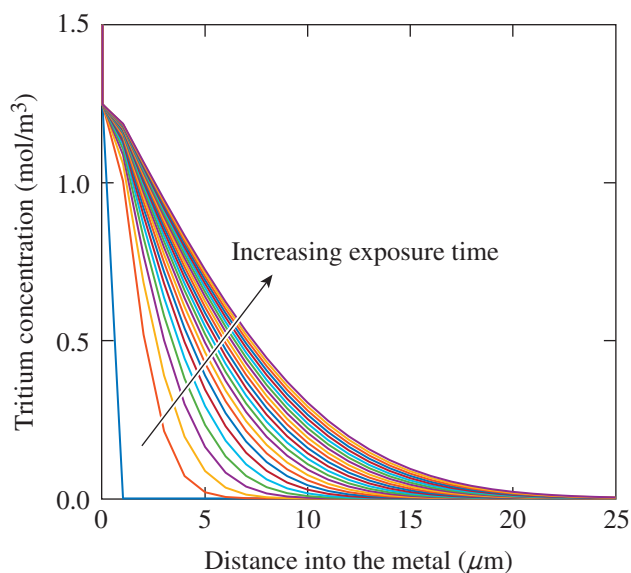
	Stainless steel	Copper	Aluminum
Frequency factor (mol/m <sup>3</sup> •atm <sup>1/2</sup> )	342	1691	4416
Activation energy (kJ/mol)	13.0	39.3	28.5
Solubility at 25°C (mol/m <sup>3</sup> )	1.8	0.22*	$4.4 \times 10^{-2}$

\*Scaled by 1000.

lattice are shown; the high surface concentrations are off-scale. Using the final profile, we calculate that tritium penetrates a mean distance of  $\sim 10 \mu\text{m}$  into stainless steel. This compares favorably with the expected mean migration distance, which is found from the semi-infinite solution to the diffusion equation. The expected mean migration distance is

$$\langle x \rangle = \sqrt{4Dt} = 11.5 \mu\text{m}, \quad (20)$$

where  $\langle x \rangle$  is the mean migration distance,  $D$  in m<sup>2</sup>/s is the diffusivity of tritium in stainless steel, and the exposure time  $t$  is 24 h.

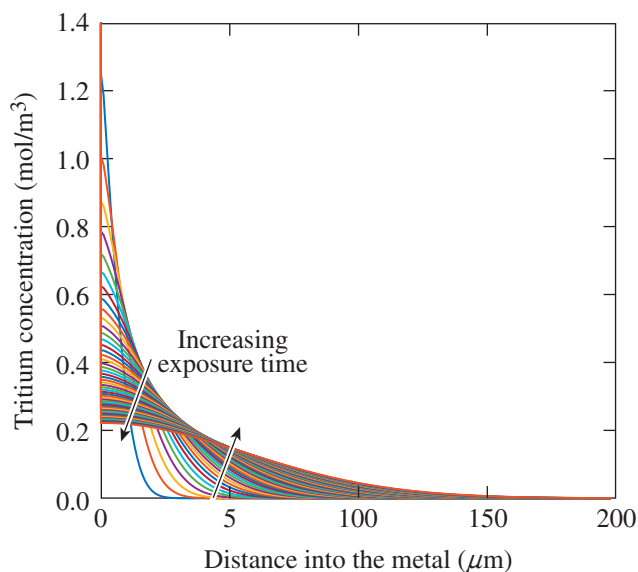


E26108JR

Figure 150.42

Evolution of tritium concentration profiles in stainless steel during an exposure to tritium.  $P = 612$  Torr,  $\chi_{\text{tritium}} = 0.6$ ,  $t = 24$  h,  $Q = 10^{-5}$  mol/m<sup>2</sup>.

In the second phase, the tritium profile evolution is tracked over a storage period of 50 days. During this time, tritium is allowed to redistribute throughout the metal, as well as to desorb from the surface. Tritium that has desorbed from the surface does not return to the sample in this example. The final concentration profile calculated for the loading procedure illustrated in Fig. 150.42 was used as the initial condition for the storage phase. The resulting concentration profiles in the metal lattice are shown in Fig. 150.43. Again, the high surface concentrations are not shown. Finally, the evolution of the concentration profiles are plotted in one-day increments. As expected the tritium concentrations in the near-surface region decrease while the tritium concentrations in the deeper regions increase with increasing storage time. This trend in the concentration profiles with increasing time produces profiles similar to those



E26109JR

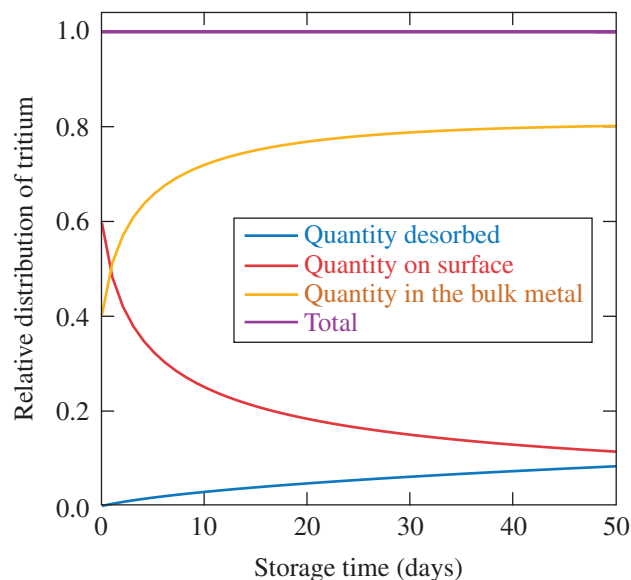
Figure 150.43

Tritium concentration profiles in stainless steel during storage following an exposure to tritium.  $P = 612$  Torr,  $\chi_{\text{tritium}} = 0.6$ ,  $t = 24$  h,  $Q = 10^{-5}$  mol/m<sup>2</sup>,  $\nu = 1 \times 10^{-7}$ /s.

observed by Penzhorn *et al.*<sup>7</sup> These authors measured a local minimum in the concentration profile near the surface. They attributed this minimum to the chronic desorption of tritium from the surface, which is an effect predicted by the model.

Figure 150.44 shows the calculated relative distribution of tritium within the stainless-steel sample over the same storage period represented by the concentration profiles in Fig. 150.43. This figure shows the relative tritium inventories contained on the surface and in the bulk metal lattice along with the relative quantity that desorbed from the surface. For reference, the total mass of the system is also included. From these results, we can see that the surface contained ~60% of the total tritium inventory immediately after the 24-h exposure. This quantity rapidly decreases over the first ten days since tritium not only diffuses into the sample but also desorbs from the sample's surface. After ~30 days of storage, the relative distribution does not change significantly because the concentration gradients in the sample illustrated in Fig. 150.41 are less steep.

In the following example, a stainless-steel sample was exposed to various atmospheres of tritium gas for differing periods of time and then stored for either zero or one day prior to decontamination. The cleaning protocol was repeated over a ten-day period. In these two examples, the surface activity was reduced to zero during decontamination and the sample was stored for one day before repeating the cleaning procedure.



E26110JR

Figure 150.44

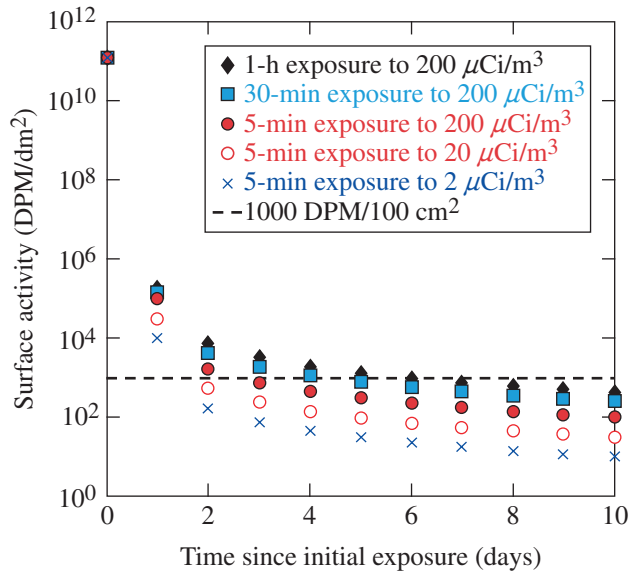
Dependence of relative distribution of tritium in stainless steel on storage time following an exposure to tritium. Included in this plot are the relative quantities of tritium that desorbed from the sample, as well as those remaining on the surface and in the bulk metal lattice.  $P = 612$  Torr,  $\chi_{\text{tritium}} = 0.6$ ,  $t = 24$  h,  $Q = 10^{-5}$  mol/m<sup>2</sup>,  $\nu = 1 \times 10^{-7}$ /s.

During the storage periods, tritium could diffuse deeper into the sample as well as desorb from the surface. During loading, the surface concentration was fixed by the given exposure conditions and the tritium content in the sample bulk was set to zero. For reference, the 1000-DPM/dm<sup>2</sup> threshold is shown as a dashed line in each of the following two plots, where DPM is disintegrations per minute.

Figure 150.45 shows the activity on the metal surface immediately prior to the cleaning. The exposure and cleaning sequence indicates that tritium migrates back to the surface within each 24-h storage period. Further, regardless of the initial exposure conditions, the surface activity present after the first 24-h period indicates that the surface is above the 1000-DPM/dm<sup>2</sup> threshold. In all exposure cases considered, one additional decontamination was sufficient to bring the surface below the threshold. Additional decontaminations performed after the second day showed no significant depletion of the surface activity. A sufficient quantity of tritium is present within the metal lattice to replenish the surface with tritium to nearly the same level each following day.

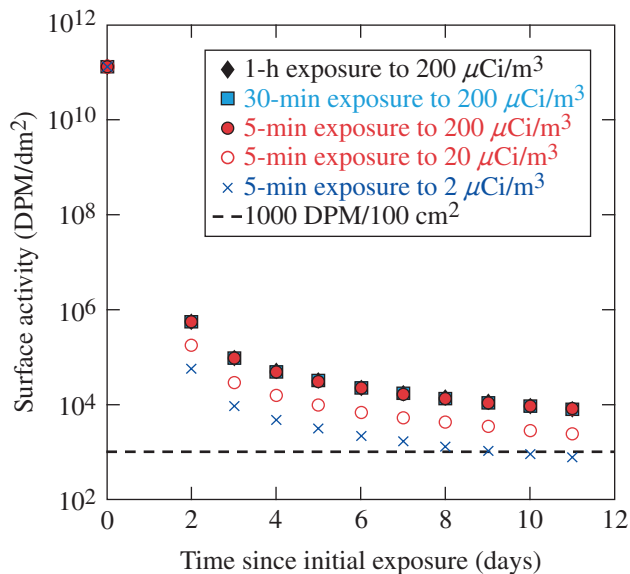
Storing the sample for 24 h after an exposure significantly affected the residual surface activity after decontamination. Figure 150.46 shows the surface activity on the sample stored

for 24 h after exposure and before the first decontamination. In general, the results show that storing the samples for one day results in surfaces containing higher quantities of tritium



E26111JR

Figure 150.45 Dependence of surface activity on stainless steel on decontamination sequences without a storage period after exposure. The decontamination was repeated every 24 h for ten days.  $Q = 10^{-5} \text{ mol/m}^2$ ,  $\nu = 1 \times 10^{-7} \text{ /s}$ .



E26112JR

Figure 150.46 Dependence of surface activity of stainless steel on decontamination sequences following a one-day storage period after exposure. The decontamination was repeated every 24 h for ten days.  $Q = 10^{-5} \text{ mol/m}^2$ ,  $\nu = 1 \times 10^{-7} \text{ /s}$ .

after each decontamination cycle. Compared with the samples that were decontaminated immediately after exposure, most of the stored samples did not reach the target threshold, even after ten decay cycles. Storing the sample after exposure gave the tritium more time to diffuse into the bulk metal lattice. This higher reservoir of tritium in the metal in turn resupplied the surface with tritium, leading to the higher surface activities.

The surface activity of aluminum after exposure to tritium and a series of subsequent decontaminations was also simulated. The operating conditions were identical to those used for stainless steel. As in the stainless-steel cases, two main scenarios were considered. In both scenarios (Fig. 150.47), the metal was exposed to a range of tritium gas concentrations for a variety of durations. In the first set of cases evaluated, decontamination proceeded immediately after exposure. In the second case, decontamination was initiated one day after the tritium exposure. In both cases, once the decontamination-dwell sequence was started, the surface was decontaminated after a 24-h hiatus over ten days.

The decontamination simulations indicate that more decontamination cycles are required for aluminum that was stored for one day prior to starting the decontamination sequence. The surface activity for the stored samples does not drop below the threshold until a minimum of seven decontamination cycles have been performed, compared to a minimum of two cycles for the case when the decontamination starts immediately after exposure. As in the stainless-steel case, the one-day storage period permitted tritium to permeate deeper into the bulk metal lattice. This leads to an increased reservoir of tritium in the lattice, which subsequently migrates to the surface after each successive cleaning.

For the same exposure conditions, stainless steel requires more decontamination cycles than aluminum when the exposed samples are stored for one day before starting the decontamination sequence. This difference is attributed to the fact that the diffusion of tritium into steel is  $2 \times 10^4$  slower compared to aluminum. The higher diffusivity of tritium into aluminum expedites tritium migration to the surface after each cleaning. As a result, a greater fraction of the tritium inventory is removed from the bulk with each successive decontamination and the surface activity remaining after each 24-h period decreases faster on aluminum than on stainless steel.

The tritium exposure and decontamination protocols described above were repeated using 3-cm-thick aluminum instead of a 0.3-cm-thick sample (Fig. 150.48).

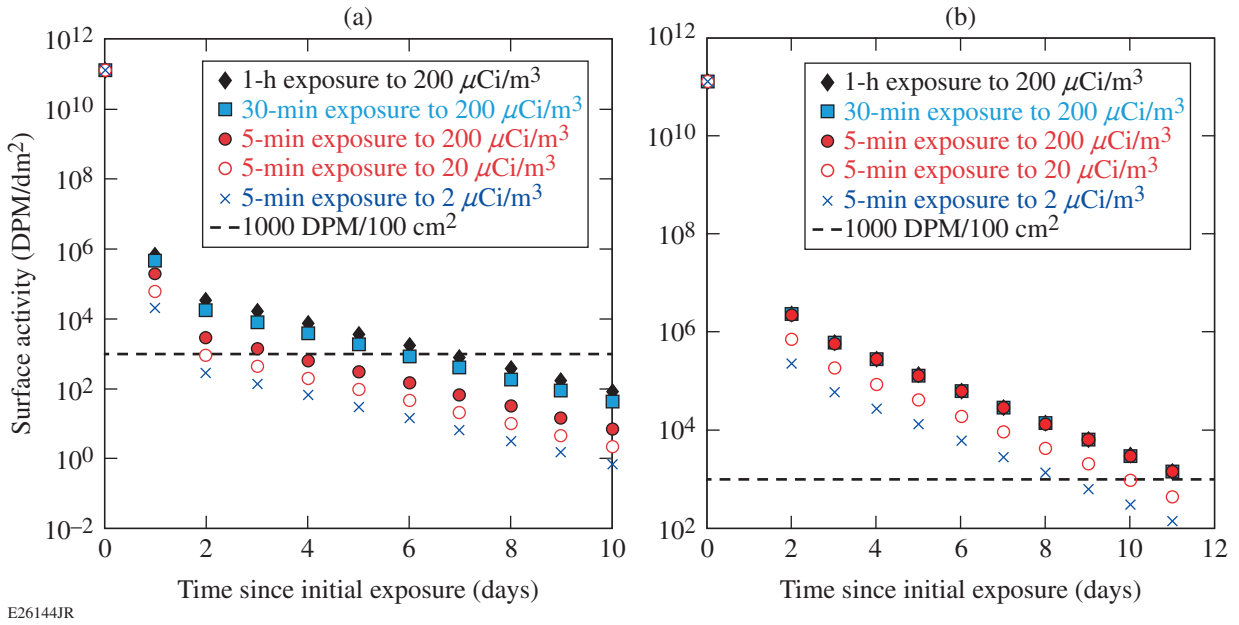


Figure 150.47  
 Decrease in the surface activity on 0.3-cm-thick aluminum calculated for a range of exposure conditions for two cases. (a) Decontamination was initiated immediately after exposure. (b) Decontamination was initiated one day after the exposure. The surfaces were decontaminated once every 24 h over a ten-day period in both cases.  $Q = 10^{-5}$  mol/m<sup>2</sup>,  $\nu = 1 \times 10^{-7}$ /s.

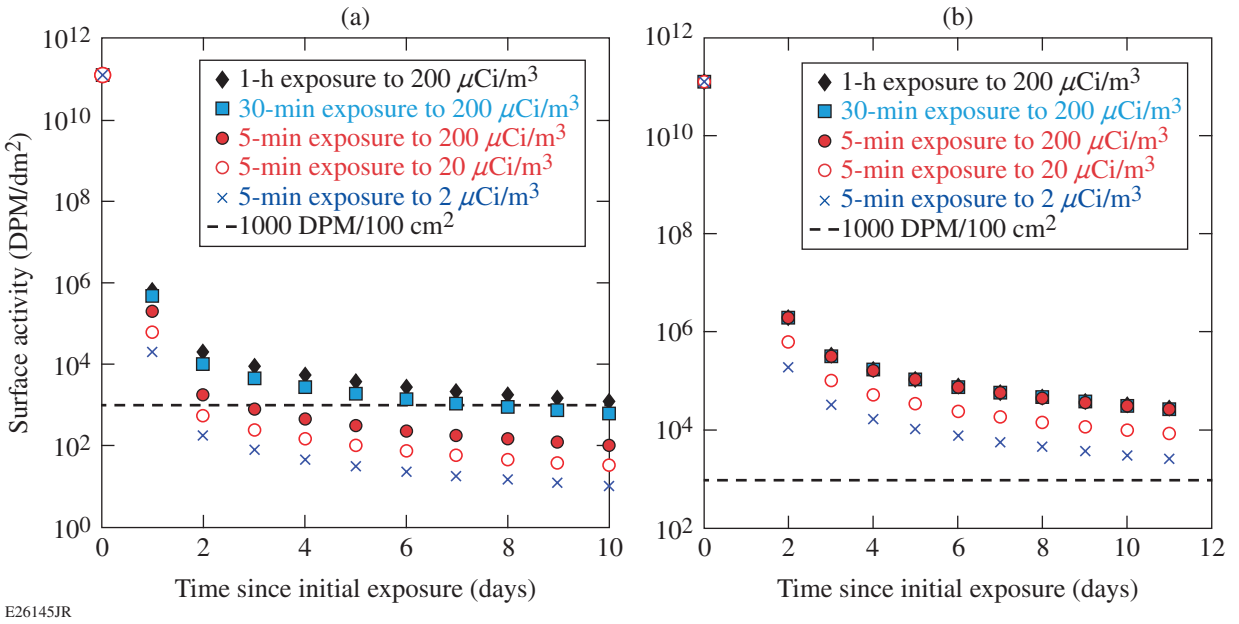


Figure 150.48  
 Decrease in the surface activity on 3-cm-thick aluminum calculated for a range of exposure conditions for two cases. (a) Decontamination was initiated immediately after exposure. (b) Decontamination was initiated one day after the exposure. The surfaces were decontaminated once every 24 h over a ten-day period in both cases.  $Q = 10^{-5}$  mol/m<sup>2</sup>,  $\nu = 1 \times 10^{-7}$ /s.

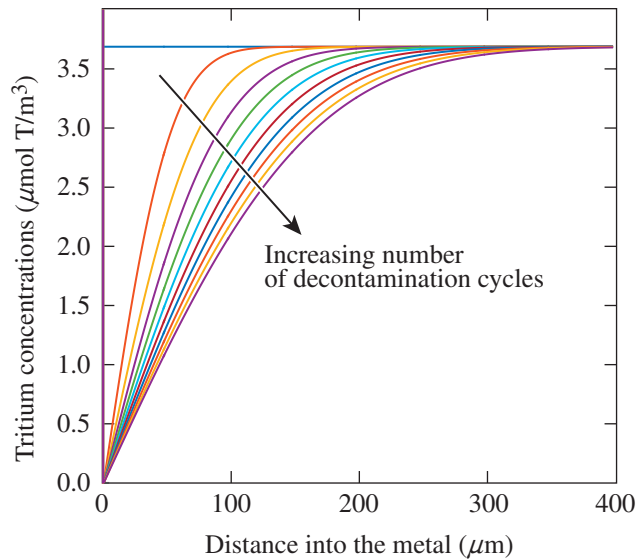
The calculations show that increasing the thickness of the aluminum results in higher surface activities throughout the decontamination process. For the immediate decontamination scenario, the surface activity remains above the target threshold for the higher tritium concentrations and longer exposure condition and drops below the threshold for the shorter periods and/or lower concentrations. In the delayed decontamination scenario, the residual surface activity does not drop below the threshold for any of the exposure cases considered. Additionally, the decay in the residual surface activity in both scenarios does not follow the trend observed for the 0.3-cm case illustrated in Fig. 150.47. In the 0.3-cm case, the residual surface activity decreased linearly after the second surface cleaning. In the 3-cm case, the residual surface activity decreases at a slower, nonlinear rate. The increased metal volume provides a larger reservoir for tritium in the 3-cm case for identical exposure conditions. Increasing the thickness of the aluminum allows tritium to migrate deeper into the bulk during the dwell periods between surface decontaminations because of the higher diffusivity of tritium in aluminum.

In the following example, a stainless-steel sample was exposed to a tritium atmosphere containing  $5 \mu\text{Ci}/\text{m}^3$  until a steady state was reached. Afterward, the sample was subjected to the same decontamination cycles described above. The surface was decontaminated once a day for ten days where each decontamination was assumed to completely remove all surface-bound tritium. During the storage period between the surface cleanings, tritium repopulated the surface and could desorb from the surface. The results are shown in Figs. 150.49 and 150.50. Figure 150.49 shows the tritium concentration profiles in the bulk metal after each decontamination, while Fig. 150.50 shows the surface activity remaining prior to the next decontamination cycle.

Figure 150.49 shows that each successive decontamination further depletes the tritium content in the near-surface region. This depletion is in response to the removal of the surface activity and, consequently, the abrupt change in the tritium inventory at the interface on the metal side. The concentration gradient drives tritium to migrate out of the metal lattice and back into the surface layer. Storing the sample for one day between successive decontamination cycles provides the necessary time for tritium to migrate into the surface water layer. Increasing the storage time would increase the quantity of tritium migrating to the surface since tritium diffusion through the metal lattice limits the flux to the surface.

In addition to depleting the near-surface tritium with each decontamination, the simulation shows that the surface con-

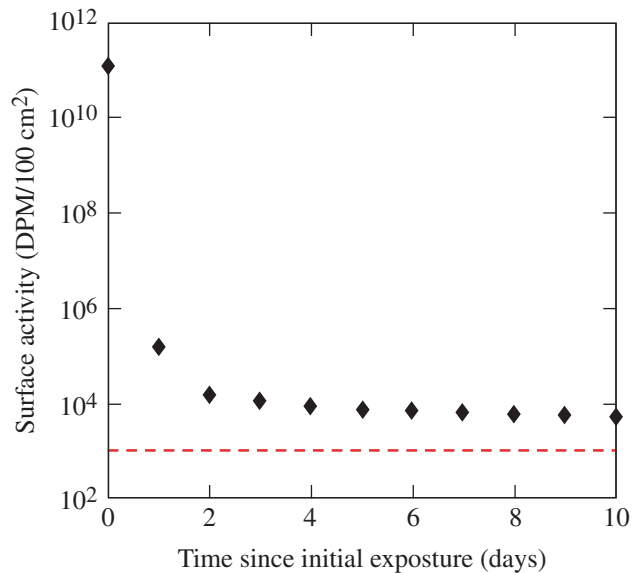
tamination cannot reach the  $1000\text{-DPM}/\text{dm}^2$  threshold within ten decontamination cycles. Figure 150.50 shows the evolution



E26113JR

Figure 150.49

Evolution of tritium concentration profiles that develop in the bulk metal of stainless steel following sequential decontaminations after exposure to  $5 \mu\text{Ci}/\text{m}^3$  of tritium in an inert environment until steady-state concentration profiles were reached in the metal. The profiles are plotted in one-day increments for sequential decontaminations. The initial profile is shown for reference.



E26114JR

Figure 150.50

Dependence of the surface activity on decontaminations repeated once a day over ten days for stainless steel exposed to a tritium atmosphere of  $5 \mu\text{Ci}/\text{m}^3$  for a prolonged period. The sample was stored for 24 h between decontaminations.  $Q = 10^{-5} \text{ mol}/\text{m}^2$ ,  $P_{\text{tritium}} = \mu\text{Ci}/\text{m}^3 = 3.2 \times 10^{-9} \text{ Torr}$ ,  $\chi_{\text{tritium}} = 1$ ,  $\nu = 1 \times 10^{-7}/\text{s}$ .

of surface activities with sequential decontaminations. While the decontamination cycles reduce the residual surface activity to lower values, progress to puncture the 1000-DPM/dm<sup>2</sup> threshold is slow. The difficulty in reducing surface contamination is because of the vast reservoir of tritium present within the metal lattice.

QTRIMM can also be used to calculate the temporal evolution of tritium pulses applied to various metals. In the example under consideration, one side of a metal wall is exposed to a deuterium–tritium (DT) gas mixture at room temperature. Following the exposure, the DT gas is evacuated and the wall remains under vacuum for a specified period of time. This cycle of exposure followed by vacuum outgassing is repeated several times. The tritium concentration profiles and tritium distributions are calculated for each cycle. In these calculations, the downstream boundary condition is modified to include a high-solubility surface from which tritium can desorb. This condition is identical to that used for tritium desorption from a surface in Eq. (19) except that the flux is positive since the flow is in the opposite direction. The permeation calculations compare the performance of three metals: aluminum, copper, and stainless steel using the literature survey averages of the solubilities and diffusivities for the three metals listed in Tables 150.III and 150.IV. The solubility of tritium in copper was increased by a factor of 1000 relative to the literature survey average to account for the observed increase in hydrogen solubility in copper at low temperatures. The parameters listed in Table 150.V are used for this example for the three metals. We cannot assume that the quantity of water absorbed on the metal surfaces is the same for the three metals because these quantities are metal dependent.<sup>6</sup> Additionally, the desorption rates from the upstream and

downstream surfaces may be different because of the different environments;<sup>12</sup> however, these parameters are not expected to differ significantly from metal to metal.

The response of the metals to the tritium pulses are shown in Figs. 150.51–150.53. In each figure (a) shows the calculated

Table 150.V: Parameters used to calculate tritium permeation through the selected metals.

Mole fraction of tritium in the gas	0.7
DT pressure	50 Torr
Temperature	298 K
Quantity of adsorbed water on upstream (DT gas/vacuum) wall	10 <sup>-5</sup> mol H <sub>2</sub> O/m <sup>2</sup>
Quantity of adsorbed water on downstream (lab air) wall	5 × 10 <sup>-5</sup> mol H <sub>2</sub> O/m <sup>2</sup>
Desorption rate constant (both surfaces)	10 <sup>-7</sup> /s
Exposure time	100 h
“Storage” time	50 h
Wall thickness	3 mm
Number of exposure/vacuum cycles	5

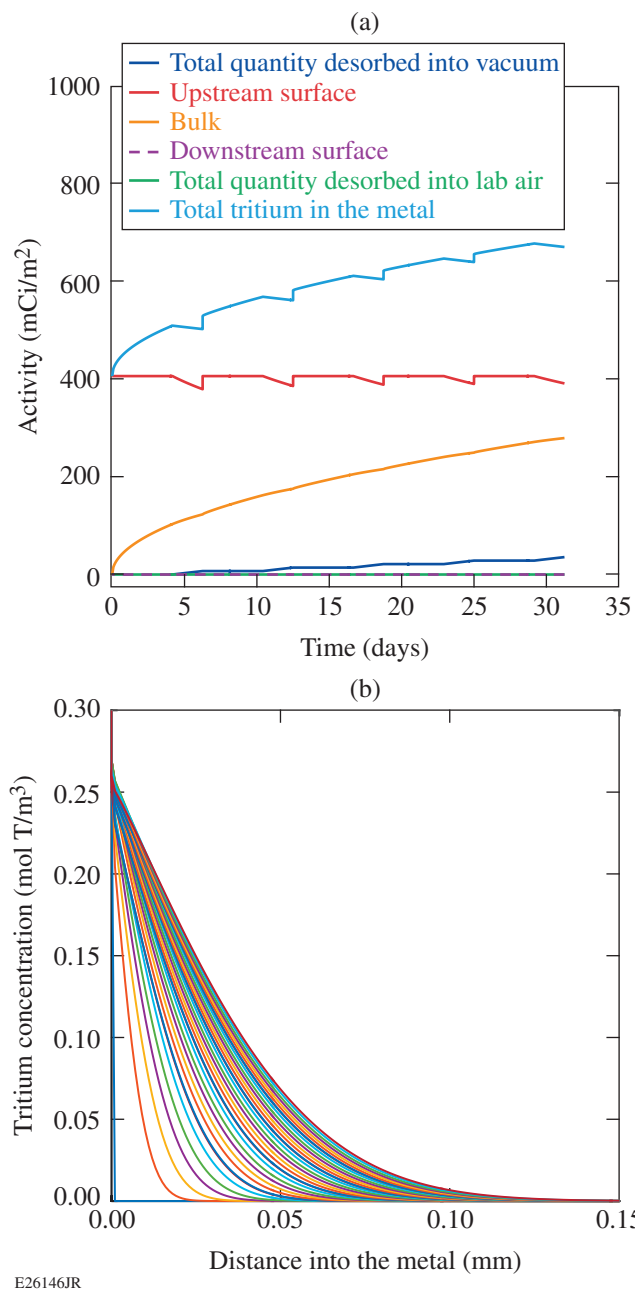
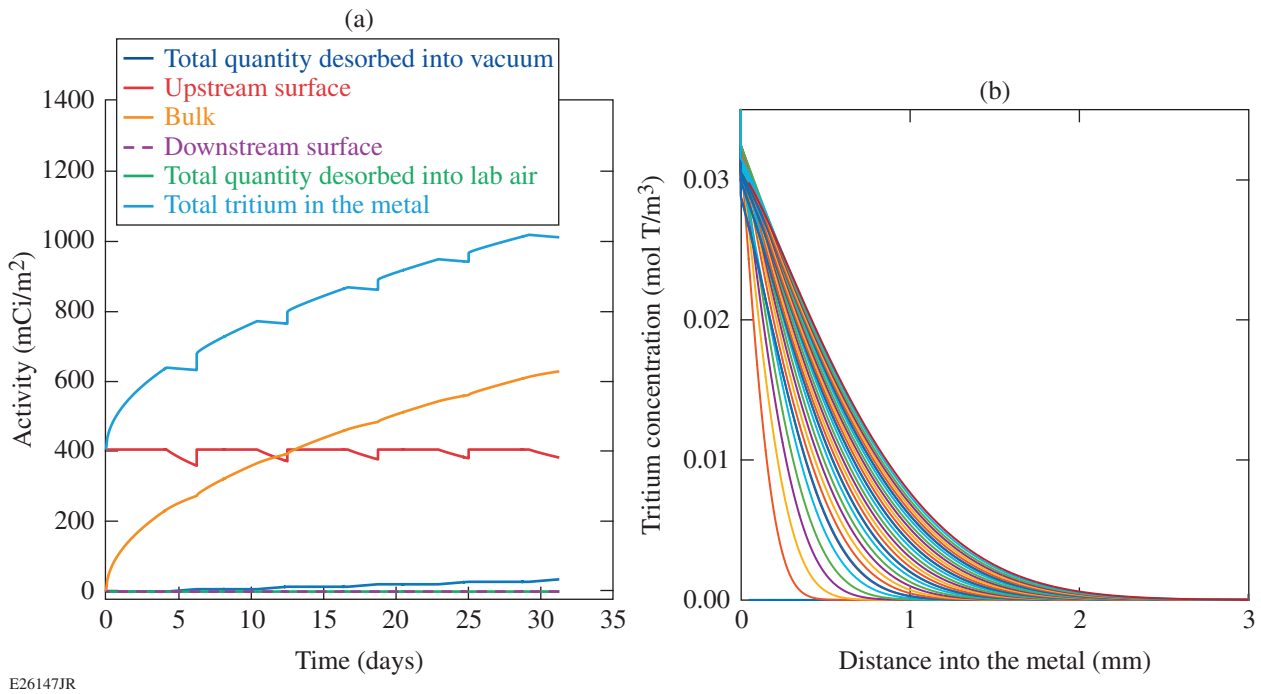


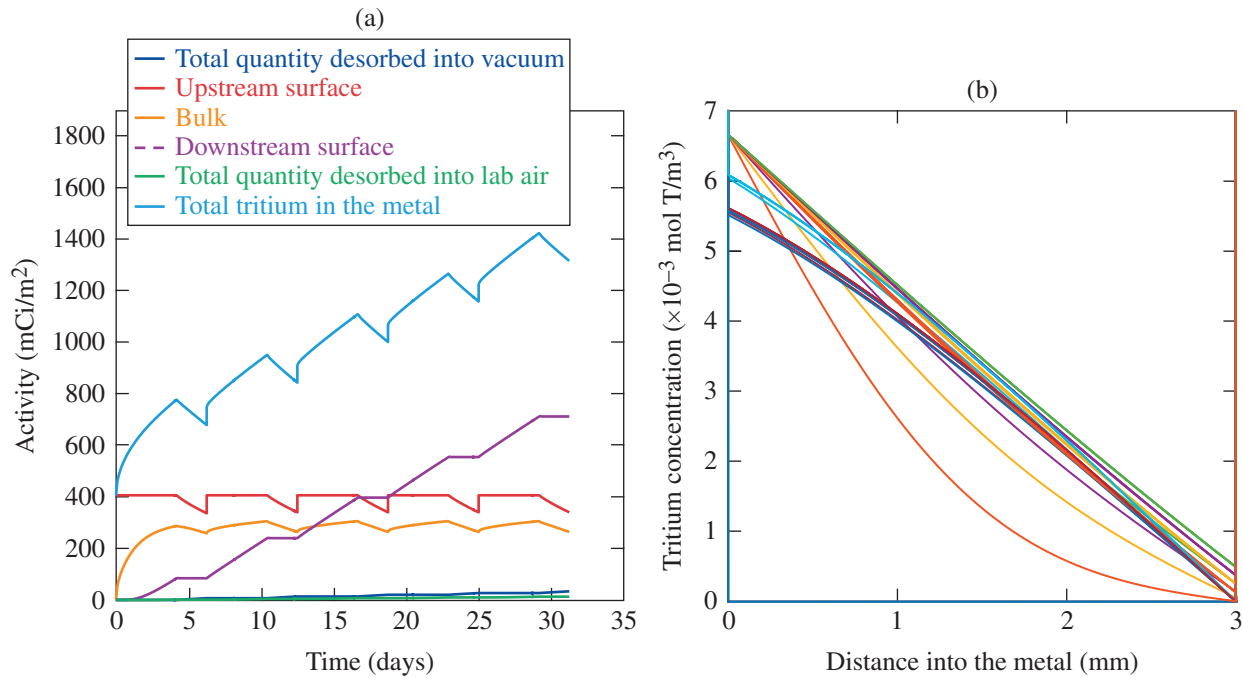
Figure 150.51 (a) Activity distribution and (b) tritium concentration profiles calculated for a stainless-steel wall exposed to repeated cycles of DT gas followed by vacuum desorption.



E26147JR

Figure 150.52

(a) Activity distribution and (b) tritium concentration profiles calculated for a copper wall exposed to repeated cycles of DT gas, followed by vacuum desorption.



E26148JR

Figure 150.53

(a) Activity distribution and (b) tritium concentration profiles calculated for an aluminum wall exposed to repeated cycles of DT gas, followed by vacuum desorption.

quantities for tritium present on the upstream and downstream surfaces, tritium within the metal lattice, and the amount of tritium lost to the downstream side. The total tritium inventory present on the surfaces and in the lattice is plotted as well. In each figure (b) shows the evolution of the tritium concentration profiles in the metal lattice over the course of five exposure and vacuum cycles. In general, the activity distributions show that each wall absorbs tritium during each DT exposure. Additionally, while tritium desorbs from the inner wall when under vacuum, the duration of the exposure to vacuum is not long enough to allow a significant release of the absorbed tritium. Ultimately, this leads to the metal wall absorbing increasingly more tritium with each exposure-vacuum cycle. The tritium concentration profiles within the metal lattice show increasing penetration into the metal with each successive cycle. The exception is for aluminum, which attains steady-state permeation through the wall within the first exposure cycle.

The simulations show several notable differences among the three metals. The first difference is evident in the calculated concentration profiles within each metal. The profiles indicate that tritium permeates through aluminum much faster than the other two metals, such that steady-state permeation is achieved within the first DT exposure. Additionally, while the subsequent vacuum portions of each cycle serve to decrease the concentrations throughout the aluminum wall, steady-state permeation is reclaimed during the following DT exposure. For copper, a negligible quantity of tritium permeates through the wall and steady-state permeation is not achieved during the five cycles. Finally, permeation through stainless steel is the slowest, with no tritium reaching the downstream surface. This trend in tritium permeation rates follows the same trend in the tritium diffusivity through each metal: tritium diffusivity is slowest in stainless steel and quickest in aluminum. As a consequence, the calculated quantity of tritium desorbing from the downstream side of the wall is largest for aluminum and smallest for stainless steel.

### Conclusions

QTRIMM, outlined in this article, allows one to calculate the tritium concentration profiles within a metal sample. This model represents a novel approach to assessing the migration of tritium into, out of, and within a metal. It accounts for high concentrations of tritium on metal surfaces. The model predicts the evolution of the tritium concentration profiles that develop during an exposure to tritium gas, during subsequent storage periods, and during iterative decontamination cycles. This article illustrates the application of QTRIMM to show the tritium concentrations within stainless steel that was exposed

to tritium gas and then stored for 50 days. Additionally, QTRIMM was used to predict the changes in surface activity as a result of decontamination cycles. The model demonstrates two well-known phenomena: (1) tritium can “reappear” on a decontaminated surface and (2) the longer one waits to clean a contaminated surface, the harder it is to decontaminate the metal. Finally, QTRIMM was used to predict the quantities of tritium that can permeate through aluminum, copper, and stainless steel. The calculations show that the greatest quantity of tritium permeated through aluminum compared to copper or stainless steel of the similar thicknesses. As a result of the quicker diffusion of tritium through aluminum, the model predicts that aluminum will contain the largest quantity of tritium after several exposures to DT gas compared to the other two metals but it is expected to be decontaminated more quickly than the other two metals.

### ACKNOWLEDGMENT

This material is based upon work supported by the Department of Energy National Nuclear Security Administration under Award Number DE-NA0001944, the University of Rochester, and the New York State Energy Research and Development Authority.

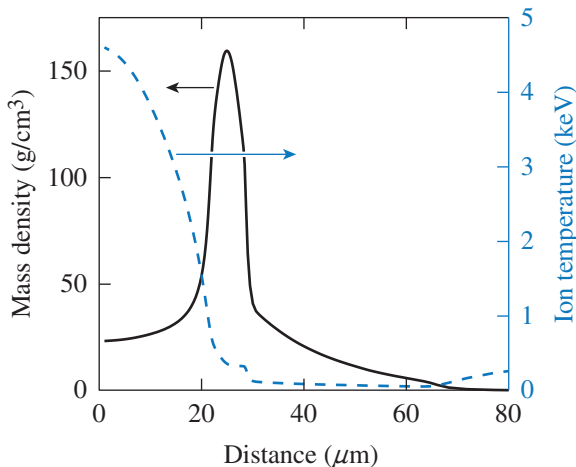
### REFERENCES

1. N. Nakashio *et al.*, *Fusion Sci. Technol.* **39**, 189 (2001).
2. K. Akaishi *et al.*, *J. Vac. Sci. Technol. A* **26**, 321 (2008).
3. S. Naoe *et al.*, *Fusion Sci. Technol.* **54**, 515 (2008).
4. R.-D. Penzhorn *et al.*, *Fusion Sci. Technol.* **57**, 185 (2010).
5. T. Hirabayashi, M. Saeki, and E. Tachikawa, *J. Nucl. Mater.* **126**, 38 (1984).
6. M. Nishikawa *et al.*, *J. Nucl. Mater.* **277**, 99 (2000).
7. R.-D. Penzhorn *et al.*, *J. Nucl. Mater.* **353**, 66 (2006).
8. Y. Torikai and R.-D. Penzhorn, *Fusion Sci. Technol.* **67**, 615 (2015).
9. G. Münchow *et al.*, *Langmuir* **24**, 8547 (2008).
10. R. A. Surette and R. G. C. McElroy, *Fusion Technol.* **14**, 1141 (1988).
11. M. Sharpe, W. T. Shmayda, and W. U. Schröder, *Fusion Sci. Technol.* **70**, 97 (2016).
12. W. T. Shmayda, M. Sharpe, A. M. Boyce, R. Shea, B. Petroski, and W. U. Schröder, *Fusion Sci. Technol.* **68**, 766 (2015).

# Three-Dimensional Modeling of Neutron-Based Diagnostics to Infer Plasma Conditions in Cryogenic Inertial Confinement Fusion Implosions

## Introduction

In direct-drive cryogenic inertial confinement fusion (ICF)<sup>1</sup> implosions, a target comprising a shell of cryogenic deuterium–tritium (DT) fuel enclosing a vapor region is irradiated using multiple nearly identical laser beams. As the kinetic energy of the imploding shell is converted to the thermal energy of the hot spot, the shell undergoes deceleration and conditions relevant for achieving fusion reactions are obtained. Conditions achieved in the compressed core, at the time of peak fusion neutron production, from a typical cryogenic direct-drive implosion on the OMEGA Laser System<sup>2</sup> are shown in Fig. 150.54. The profile was obtained from a spherically symmetric simulation using the code *LILAC*;<sup>3</sup> nonuniformity was ignored in this calculation. Ideally, a hot core is surrounded by a high-density shell, although multidimensional simulations indicate that while this is largely true, the neutron-producing region is typically not centered and the high-density shell can be significantly perturbed. Perturbations are typically quantified in terms of spherical harmonics (from 3-D simulations) or Legendre modes (in 2-D experimental images or 2-D simulations).



TC13274JR

Figure 150.54  
A typical density and temperature profile at peak neutron production in an OMEGA cryogenic implosion.

The goal of cryogenic implosions on OMEGA is to understand the physics of directly driven ICF implosions. This requires observations that could potentially shed light on failure mechanisms including the role of long-wavelength asymmetries on target performance. Three-dimensional (3-D) direct-drive simulations that include the effect of long-wavelength asymmetries performed with the arbitrary Lagrangian–Eulerian (ALE) code *HYDRA*<sup>4</sup> indicate that significant long-wavelength asymmetries corresponding to spherical harmonics up to 4 should be present during the time of neutron production. These asymmetries can be seeded by power imbalance among the 60 beams of OMEGA; by beam mistiming, beam mispointing, or nonuniformities on the inside of the cryogenic layer at the ice–vapor interface; or by the initial error in the placement of the target relative to the center of the target chamber, etc. Long-wavelength asymmetries can compromise performance by reducing the clean volume over which neutrons are produced. In Fig. 150.54, the clean volume has a radius of  $\sim 20 \mu\text{m}$ . The Rayleigh–Taylor<sup>5</sup> growth of the nonuniformities during the deceleration phase of the imploding capsule results in growth at approximately this radius; spikes of the high-density shell penetrate the hot spot, whereas bubbles of lower-density material distort the high-density shell. These large bubbles in the high-density shell may permit heat and fuel to escape, thereby decreasing fusion yields. These asymmetries result in angular variations in areal density, defined as

$$\rho R = \int_0^R \rho(r) dr,$$

the radial integral of the areal density, where  $\rho(r)$  is the density along the radius of the target, and  $R$  is the outer radius of the target. Another manifestation of these asymmetries is large-scale fluid flow resulting in residual kinetic energy, i.e., kinetic energy that has not been converted to hot-spot energy. Diagnosing these asymmetries is important for identifying a potential source of performance degradation. Until recently, x-ray images from a single view have been used to infer the existence of asymmetries in OMEGA cryogenic implosions,<sup>6,7</sup>

although quantitative measures are outstanding. Multiple views of neutron-based diagnostics have also been available, although a tool to interpret the results has been unavailable. In this work, we show that with additional views of the neutron-based diagnostics, asymmetries can potentially be diagnosed on OMEGA. Results from a newly developed postprocessor *IRIS3D* (see **Appendix**, p. 110) for 3-D hydrodynamic codes are described here. The role of background in interpreting the various regions of the neutron spectra for the inference of areal density and its asymmetries is emphasized; the use of multiple detectors to infer a map of asymmetries is studied; and, finally, the detection of asymmetries through the effect of the residual fluid flow on neutron spectra is studied. This work is the first such analysis; future work will include detailed post-processing of 3-D simulations to compare quantities derived from neutron spectra with experiment.

The generalized Lawson criterion for ICF implosions<sup>8</sup> provides a measure of target performance and can be written for OMEGA scale as

$$\chi_{1-D} \approx \langle \rho R \rangle (\text{g/cm}^2) \left[ \frac{\langle T \rangle (\text{keV})}{4.4} \right]^{0.8}, \quad (1)$$

where  $\langle \rho R \rangle$  is the neutron-weighted areal density of the compressed target and  $\langle T \rangle$  is the neutron-weighted ion temperature in the hot spot. A value of  $\chi_{1-D} \sim 1$  indicates marginal ignition, where the ratio of the output fusion neutron energy to the input laser energy is  $\sim 1$ . This form of the generalized Lawson criterion is derived from a power law fit to a series of spherically symmetric simulations and is written in terms of quantities—neutron-weighted areal density and ion temperature—that are, in principle, observable. As discussed later, areal density is inferred from the elastically scattered neutron spectrum,<sup>9–11</sup> and ion temperature is inferred from the width of the neutron spectrum of the D–T fusion neutrons.<sup>12</sup> Asymmetrically driven implosion experiments limit, however, the ability to directly compare the experimentally inferred quantities with spherically symmetric simulations. Areal densities can vary around the imploding target and the inferred value depends on the viewing direction. Similarly, fluid flow in the hot spot can change the width of the neutron spectrum, resulting in direction-dependent influences on the apparent ion temperature. Therefore, multiple measurements are required to constrain the values attained in implosion experiments. In addition, background neutron-producing reactions in the target can introduce ambiguities in the interpretation of neutron spectra. Therefore, it is important to understand the role of backgrounds and perform studies on

different patterns of asymmetry to be able to interpret observations. Simultaneously, comparing results from 3-D hydrodynamic simulations to observations is necessary to identify the adequacy of the modeling and infer the role of nonuniformity seeds in experiments. This requires a tool to post-process 3-D simulations and compare observables with experiment.

In this article, a Monte Carlo neutron-tracking code *IRIS3D* (see **Appendix**, p. 110) is used to model neutron transport from three primary fusion reactions in a DT capsule: the 14.1-MeV D–T fusion neutrons, the 2.45-MeV D–D fusion neutrons, and the T–T three-body reaction, which results in a continuum of neutrons. Additionally, three secondary interactions of the primary D–D and D–T neutrons including the elastic scattering off the deuterium and tritium ions (used to diagnose areal density) and the neutron-induced deuteron breakup reaction (which provides a background to the elastic scattering reactions) are also modeled. Neutron-induced triton breakup is not included in this work because its cross section is  $\sim 4\times$  smaller than the deuteron breakup reaction.<sup>13</sup>

In the following sections, the basic well-known relationship between  $\rho R$  and elastic scattering is described;<sup>9–11,14</sup> the effect of neutrons from other fusion processes in the compressed target on the inference of areal density, i.e., the role of backgrounds, is discussed; and the kinematics of the elastic scattering reaction to infer the areal density in different parts of the target is exploited. The inference of areal-density asymmetries with multiple detectors is discussed along with inferring ion temperatures from neutron spectral widths. It is shown that the effect of fluid flow is an increase in the width of the neutron spectrum, leading to an increase in the inferred ion temperature. Therefore, significantly different values of ion temperature inferred from different directions around a compressing core should indicate the presence of asymmetries. It is also shown that while the absolute values of the inferred temperatures might be inaccurate, the relative values still potentially track the underlying asymmetry. Finally, conclusions are presented.

### Areal Density and Elastic Scattering

The number of neutrons that scatter elastically,  $y'_n$ , as a number of primary neutrons,  $y_n$ , that move along a path  $s$  is given by

$$y'_n = \int_s y_n n \sigma ds, \quad (2)$$

where  $n$  is the number density of deuterons or tritons (particles per unit volume) and  $\sigma$  is the cross section of the scattering

interaction. For the D–T primary neutrons at 14.1 MeV, the cross section for scattering off deuterons is  $\sigma = \sigma_d \approx 640$  mb, and for scattering off the background tritons is  $\sigma = \sigma_t \approx 930$  mb. If the substitution

$$n = \frac{\rho}{\bar{m}} f \quad (3)$$

is used, where  $\bar{m}$  represents the average mass of particles in the material and  $f$  represents the fraction of particles that are of the type of interest (for DT fuel with equal proportions of D and T,  $M = 2.5$  amu, and  $f = 1/2$ ), Eq. (3) can be rewritten as

$$y'_n = \int_s y_n \frac{\rho}{\bar{m}} f \sigma ds. \quad (4)$$

The primary neutron yield  $y_n$  is not a constant along the path length since some fraction undergoes various reactions in the compressed target, including the process of elastic scattering; however,  $y_n$  typically changes by less than 10% along a path. For the purpose of illustrating the dependencies, it is assumed to be constant. The code used here takes into account the reduction of  $y_n$  along a path. Therefore, since  $\sigma$  and  $f$  are constants along the path length of the neutrons, the ratio of the scattered to primary neutrons can be written as (also called the down-scatter ratio or DSR)

$$\frac{y'_n}{y_n} \approx \sigma f \int_s \rho(s) ds. \quad (5)$$

Including scattering off both the deuterons and tritons, one can write an expression for the total DSR as

$$\text{DSR} \equiv \frac{y'_n}{y_n} \approx \frac{f_d \sigma_d + f_t \sigma_t}{\bar{m}} \cdot \rho L, \quad (6)$$

where

$$\rho L = \int_0^L \rho ds$$

is the areal density along a total path length  $L$ . The DSR is the observed quantity in the experiment used to infer areal density. If the trajectories of the neutrons were purely radial,  $\rho L$  would correspond to  $\rho R$ , where  $R$  is the radius of the plasma. Since fusion reactions occur throughout the hot core, neutron trajec-

tories are not radial, even for spherically symmetric implosions. Therefore, comparisons between the calculated and the observed DSR are required to identify if the simulated areal density has been achieved in implosion experiments. In addition,  $\rho L$  is dominantly sampled when the neutron-production rate is the highest in the experiment. Consequently, the areal density inferred in the experiment corresponds to a neutron-weighted value. In the remainder of this article,  $\rho L$  and  $\rho R$  will be used interchangeably. It should be kept in mind, however, that the inference of an areal density from a neutron spectrum results in a value for  $\rho L$ , whereas lineouts from the center of a simulated profile would provide a measure for  $\rho R$ .

To test and illustrate the physics associated with neutron interaction and transport, an ice-block profile that approximates typical profiles in a cryogenic implosion was used (Fig. 150.55). This ice-block model is characterized by regions of constant density and temperature. Neutron spectra (Fig. 150.56) using a Monte Carlo approach were calculated for the profile. Calculated cross sections for elastic scattering,<sup>15</sup> which previously have shown excellent agreement with measurements,<sup>15</sup> were used in this calculation. This Monte Carlo code, which post-processes spherically symmetric simulations, has also been compared previously with experiment and shown to be in excellent agreement when detailed capsule simulations are post-processed to obtain spectra for a limited class of implosions.<sup>16</sup> Of note in the neutron spectrum are the DT primary peak at 14.1 MeV and the deuteron and triton backscattered edges at 1.5 and 3.5 MeV, respectively.

The DSR is influenced by the continuous portion of the spectra as shown in Fig. 150.56. Parts of the spectra are measured in OMEGA experiments by two methods: (1) the magnetic recoil

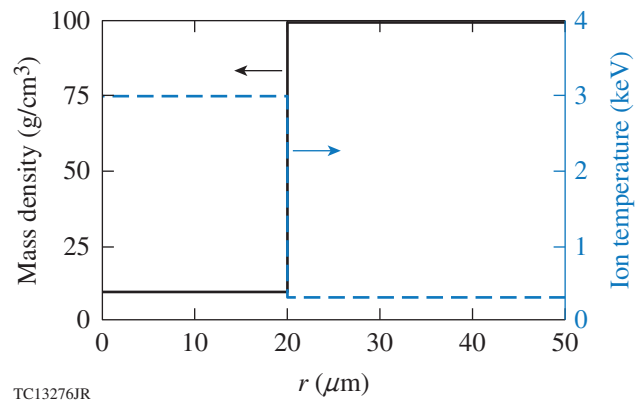


Figure 150.55  
A spherically symmetric “ice-block” test profile. A 50–50 DT fuel ratio was used.

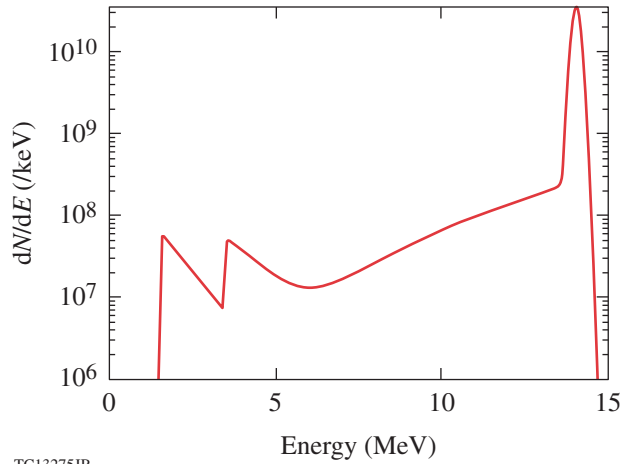


Figure 150.56  
Example of a neutron spectrum including only DT primary neutrons and deuteron and triton elastic scattering.

spectrometer (MRS)<sup>9</sup> is used to measure the down-scattered neutron spectrum between 10 and 12 MeV. (2) Neutron time of flight (nTOF) is used to measure the ratio between 3.5 and 4.5 MeV, although energies up to 6 MeV are measured currently and extension to higher energy ranges is possible.

Kinematically, DSR inferred from a specific energy range and from a particular direction samples  $\rho L$  from only a specific portion of the target. If a neutron (or any particle) of mass  $m$  and with an initial energy  $E$  scatters elastically from a particle with mass  $M$  and emerges with an energy  $E'$ , its angle of scattering  $\theta$  is given by

$$\cos\theta = \frac{x(A+1)-(A-1)}{2\sqrt{x}}, \quad (7)$$

where  $A = M/m$  and  $x = E'/E$ .

As a result, neutrons that scatter close to their original energies are deflected by small angles, whereas neutrons that emerge at low energies are nearly backscattered. When viewed from a single direction, the energy ranges of the neutron spectrum can be mapped to different parts of the target. The open squares in Fig. 150.57 show the locations of the MRS and nTOF detectors in the OMEGA target chamber. The contours represent 1-MeV energy ranges over the regions in the detector's view under the assumption of a point neutron source from the center for scattering from deuterons [Figs. 150.57(a) and 150.57(c)] and tritons [Figs. 150.57(b) and 150.57(d)]. An extended source would blur the regions and extend the region

somewhat but not significantly enough to change the conclusions. The 10- to 12-MeV range viewed by this detector has the advantage of focusing in on a narrower region of the target; however, a large number of detectors viewing this range would be necessary to get full,  $4\pi$  sampling coverage as a result. Since multiple detectors for the higher energy range can be expensive, multiple views at lower energies (i.e., through time-of-flight measurements), which can map broader regions of the target, are considered here.

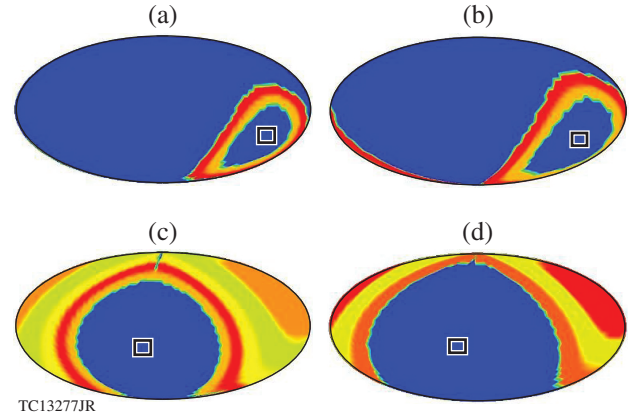


Figure 150.57  
(a) Projection of directions sampled by the magnetic recoil spectrometer (MRS) detector viewing deuteron elastic scattering in the 10- to 12-MeV range. The location of the detector in the OMEGA target chamber is shown as an open square. The contours represent the set of directions in which a primary DT neutron could be traveling under the assumption of a point-neutron source, which might result in it scattering from a deuteron in the direction of the detector. The ring is further broken up into 1-MeV-wide sub-rings, so that the outer sub-ring represents the area sampled by the 10- to 11-MeV region, and the inner sub-ring represents the area sampled by the 11- to 12-MeV energy range. (b) Same as (a) but for triton elastic scattering. [(c),(d)] Same as (a) and (b) but for a time-of-flight detector viewing the 1- to 6-MeV range. This range is now broken up into five 1-MeV sub-ranges. The locations of the time-of-flight detectors are shown as open squares.

For an nTOF detector using a range of 1 to 6 MeV, a much larger portion of the target can be sampled [Figs. 150.57(c) and 150.57(d)]. Note that only the higher three sub-rings are visible for triton backscatter [Fig. 150.57(d)] since the backscattered peaks for triton scattering occur around 3.5 MeV. Breaking up this observed spectrum into smaller sub-ranges makes it possible for a detector to sample  $\rho L$  in smaller, narrower regions of the target. In addition, by using multiple detectors, not only  $\rho L$  but also asymmetry in  $\rho L$  can be mapped to different regions of the target. As discussed in the next section, however, backgrounds can significantly influence the spectrum at these lower energies and must be accounted for carefully.

**Backgrounds for Areal-Density Inference**

The spectrum shown in Fig. 150.56 includes the primary and the elastically scattered neutrons. Additional effects such as thermal and Doppler broadening and multiple scattering are discussed in this section.

Multiple scattering is taken into account in the particle tracking code by recursively scattering neutrons off the background fuel ions until the effect is no longer numerically significant. Figure 150.58 demonstrates the effect that multiple scattering can have on down-scattered spectra for two different areal densities. Because DSR is approximately proportional to  $\rho L$ , as we have seen, multiple scattering levels should be proportional to some power of  $\rho L$ . Consequently, the effect of multiple scattering should become more significant as  $\rho L$  increases. This is shown in Fig. 150.58, where for two ice-block profiles with different areal densities, the neutron spectrum is calculated with and without multiple scattering. For the higher areal density, characteristic of cryogenic implosions at the National Ignition Facility (NIF), significant differences are observed in the neutron spectra at lower energies, indicating that multiple scattering is important under such conditions. For OMEGA-scale implosions, areal densities are typically around 0.15 to 0.25 g/cm<sup>2</sup>. In this situation, the effect of multiple scattering is negligible and can be ignored in the calculations.

All dominant components of the neutron spectrum from a cryogenic DT capsule are shown in Fig. 150.59. Again, the

ice-block spectrum in Fig. 150.55 is used to calculate the spectrum. Two additional primary neutron-generating reactions are likely to occur in a DT-filled capsule:  $d(d,n)^3\text{He}$  and  $t(t,2n)^4\text{He}$ . DD primary neutrons, generated around 2.45 MeV, are not a significant background to the down-scattered neutrons since they are clearly recognizable in the spectrum. They can interact, however, with the cold fuel, for example, by elastic scattering, causing them to contribute to the background below 2.45 MeV—e.g., around the deuteron backscattered peak.

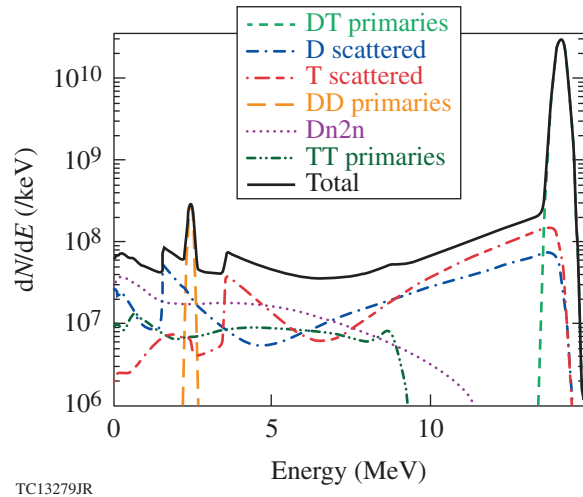


Figure 150.59 Neutron spectra generated by IRIS3D including background reactions along with thermal broadening, Doppler broadening, and multiple scattering.

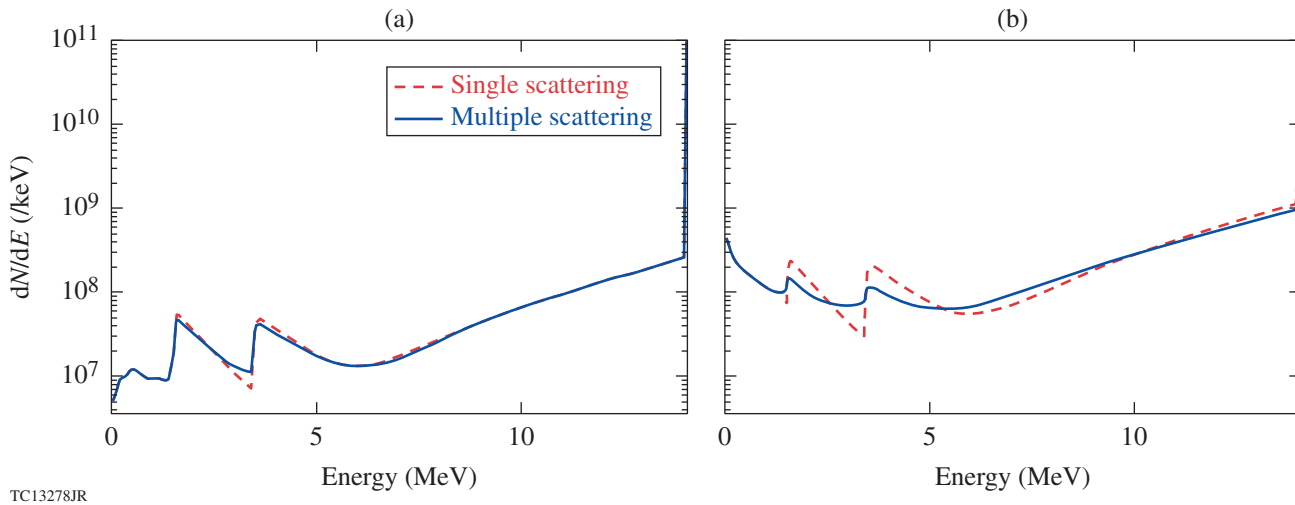


Figure 150.58 Spectra generated by IRIS3D considering only DT primaries and deuteron and triton scattering, with and without multiple scattering: (a) for the ice-block profile shown in Fig. 150.56, which has a  $\rho R$  of 0.32 g/cm<sup>2</sup>; and (b) for the same profile, but with a higher shell density of 500 g/cm<sup>3</sup>, resulting in a  $\rho R$  of 1.52 g/cm<sup>2</sup>.

Primary neutrons from the T-T reaction, on the other hand, do produce neutrons that act as background to the down-scattered signal because the T-T reaction produces three products, so the energies of the outgoing neutrons can be anywhere from 0 up to almost 10 MeV. Unlike the down-scattered spectrum, however, T-T reactions are independent of  $\rho L$ . Since *IRIS3D* also assumes that the reaction is isotropic (detailed cross-section information is unavailable), this background is assumed to be independent of the viewing angle.

Neutrons produced from the deuteron breakup reaction,  $d(n,2n)p$ , are yet another source of background to the down-scattered spectrum. Similar to the elastic-scattering reaction, this reaction is proportional to  $\rho L$ . In *IRIS3D*, this reaction is calculated only when the incoming neutron is a DT primary neutron because of the unavailability of cross sections for other energies. With an end point of 11.8 MeV, this interaction acts as a background mostly in the lower-energy portions of the spectrum. Note that when areal-density asymmetries are present, this reaction can result in ambiguities in the interpretation of areal densities from the down-scattered neutron spectrum. The directionality of neutrons from this reaction is shown in Fig. 150.60. Neutrons are launched radially from the center of the target and the locations of the product neutrons are plotted in neutrons per steradian. Figure 150.60 shows that the large

majority of deuteron-breakup neutrons emerge in the forward direction, but because there is no 1-to-1 correspondence between energy and scattering angle for an individual deuteron-breakup neutron (because there are three product particles), even these forward-emerging neutrons can have arbitrarily low outgoing energies. Therefore, an exact interpretation of the down-scattered neutron spectrum is challenging since it requires knowledge of the areal-density asymmetry to subtract the background.

The cumulative neutron spectrum (including all backgrounds) is shown in Fig. 150.61. The figure indicates that at lower energies, backgrounds can significantly influence the spectrum and therefore the inferred areal density. This is also summarized in Table 150.VI, which indicates that the  $\rho L$  inferred from the calculated spectra in the 3.5- to 4.5-MeV range including the background is considerably larger than the assumed areal density, whereas the background has a marginal effect on the inferred areal density in the 10- to 12-MeV range.

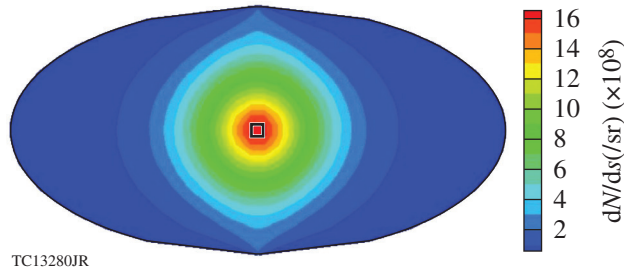


Figure 150.60 Hammer projection representing angular distribution of deuteron-breakup neutrons. Each point on the surface of a projection represents a direction in the target chamber.

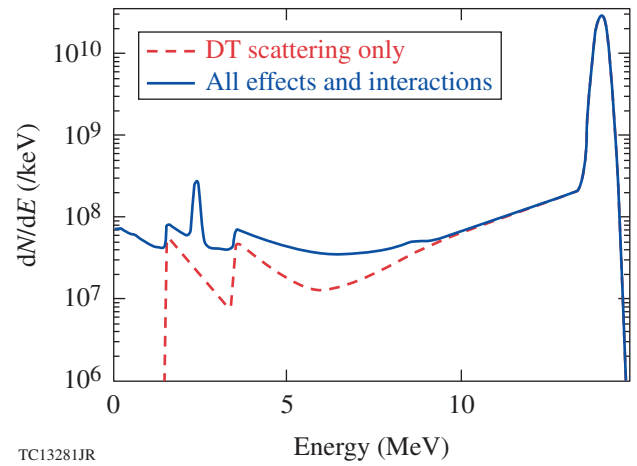


Figure 150.61 Spectra generated by *IRIS3D* for the profile shown in Fig. 150.56 with and without background effects. The areal density inferred from each spectrum in the 3.5- to 4.5-MeV and 10- to 12-MeV ranges is shown in Table 150.VI.

Table 150.VI: The  $\rho L$  values inferred from the spectra shown in Fig. 150.61 over the specified energy ranges. These values should be compared to a target  $\rho R \sim 0.32 \text{ g/cm}^2$ .

Inferred $\rho L$ ( $\text{g/cm}^2$ )	3.5 to 4.5 MeV	10 to 12 MeV
DT scattering only	0.337	0.338
All effects and interactions	0.559	0.340

### Detecting Areal Density and Asymmetries

Background can also have an effect on the inference of  $\rho R$  asymmetries. Figure 150.62 shows how the detection of areal density around an asymmetric target can be affected by the inclusion of background for two different asymmetry patterns. Asymmetric profiles are obtained by perturbing the ice-block profiles with Legendre modes. To illustrate the effect, an  $\ell = 1$  pattern with a peak-to-valley amplitude of  $0.2 \text{ g/cm}^2$  is imposed on the profile [Fig. 150.62(a)]. In what follows, it is assumed that infinite coverage around the target chamber is available. When the 3.5- to 4.5-MeV range is used to infer areal density, the opposite phase is measured for the mode [Fig. 150.62(b)]. This is because the neutrons being observed are backscattered and originate from the opposite side of the target from the detector. The minimum and maximum inferred areal densities when the background contributions are not calculated are 0.27 and  $0.41 \text{ g/cm}^2$ , respectively, so the maximum-observable contrast is  $\sim 0.14 \text{ g/cm}^2$ —less than the imposed amplitude primarily because of the averaging of the target caused by the finite solid angle of the detectors. When background contributions are included, the  $\ell = 1$  pattern is still clearly visible, but the maximum-observable contrast drops to  $\sim 0.06 \text{ g/cm}^2$  [Fig. 150.62(c)]. Consequently, while absolute values are not inferred accurately, the overall asymmetry pattern is still encoded in the neutron spectra if the pattern is dominated by  $\ell = 1$ .

Somewhat different results are obtained when an  $\ell = 2$  mode is imposed on the profile [Fig. 150.62(d)]. The  $\ell = 2$  pattern is also apparent whether or not background contributions are considered. Additionally, the phase of the underlying areal-density pattern is reproduced by the inferred areal density [Fig. 150.62(b)]. Since the asymmetry being applied is now an even mode, sampling the rear of the target actually results in the same areal density being sampled as would be seen at the front of the target, when viewed from any particular direction. The maximum-observable contrast is  $\sim 0.080 \text{ g/cm}^2$ ; when all background contributions are considered, this number drops to only  $\sim 0.075 \text{ g/cm}^2$ . The inclusion of background does not significantly hinder asymmetry detection for this mode, relative to the  $\ell = 1$  perturbation. This is again because of the opposite parities of the  $\ell = 1$  and  $\ell = 2$  modes. Recall from **Backgrounds for Areal-Density Inference** (p. 104) that (1) the deuteron-breakup background is  $\rho R$  dependent; (2) its neutrons emerge mostly in the forward direction (see Fig. 150.60); and (3) it is most significant in the backscattered (low-energy) portion of the neutron spectra, including the 3.5- to 4.5-MeV range. Therefore, when a detector infers  $\rho L$  using this range, it samples  $\rho L$  simultaneously from the opposite side of the target via elastically backscattered neutrons and the front side of the target via deuteron-breakup neutrons. In odd-mode asymmetries, these two locations will always have opposite areal densities, hindering the detection of those asymmetries, while for even-

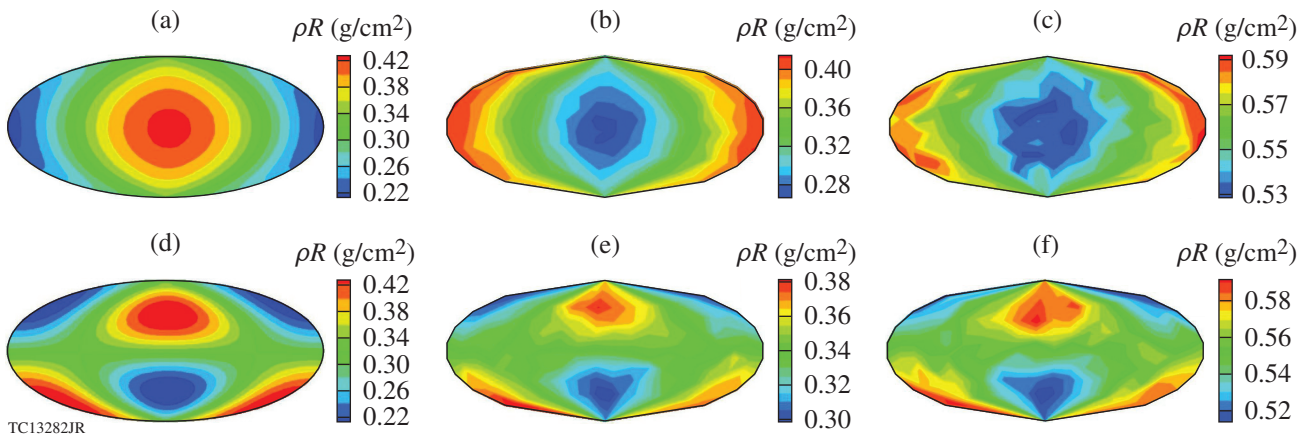


Figure 150.62

(a) Hammer plot of the line integral of  $\rho R$  from the center of the target for a profile with an imposed  $\ell = 1$  mode. As in Fig. 150.57, each point represents a location in the target chamber. The profile used is the same as that shown in Fig. 150.56, but with the spherical-harmonic perturbation applied to the value of the density in each cell based on its location. (b) Hammer plot of observed  $\rho L$  for the profile shown in (a). At each point is plotted the  $\rho L$  inferred from a detector at that location looking at the 3.5- to 4.5-MeV range, as calculated by *IRIS3D*, considering only DT primaries and single deuteron and triton scattering. (c) Same as (b), but with all effects and interaction calculated; [(d)–(f)] same as (a)–(c), but an  $\ell = 2$  mode imposed on the ice-block profile.

mode asymmetries, they will always have equal areal densities, enhancing the detection of the asymmetries. Also note that the contrast is reduced relative to the  $0.2\text{-g/cm}^2$  amplitude of the imposed mode. This is caused by the shorter wavelength of the asymmetry and the finite solid angle of the detector.

The decreasing contrast with increasing mode number is demonstrated in Fig. 160.63. Even with infinite coverage and background ignored, the contrast for an imposed mode with  $\ell = 4$  falls to 8% of the imposed value for the backscattered neutrons (3.5 to 4.5 MeV) and to 17% for the forward-scattered neutrons (10 to 12 MeV)—extremely low values that likely cannot be detected, indicating that the limit in diagnosing asymmetries is likely longer than the wavelengths corresponding to  $\ell = 4$ .

Background subtraction is the subject of active investigation for low-energy neutron spectra<sup>11</sup> and is not discussed further

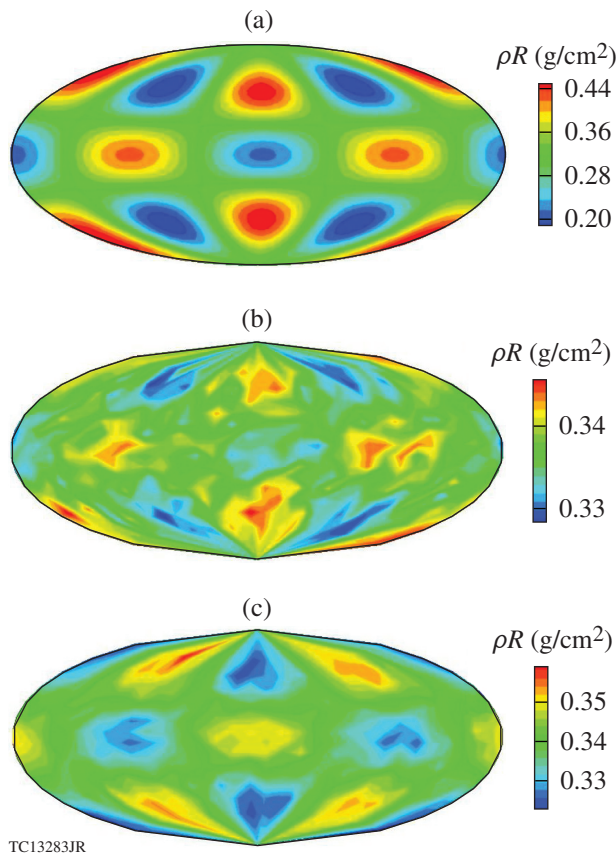


Figure 150.63  
 (a) Same as Fig. 150.61(a), with a Legendre model  $\ell = 4$  imposed on the profile;  
 (b) same as Fig. 150.61(b), but for the profile shown in part (a) of this figure;  
 (c) same as (b), but using the 10- to 12-MeV energy range.

in this work. For the remainder of this article, it is assumed that background can be accounted for by fitting an extended spectrum, potentially up to 10 MeV. The discussion that follows considers theoretical limits on inferred areal densities with a more realistic scenario: a finite number of detectors.

An areal-density map can be reconstructed as follows: For each detector and each energy sub-range, a  $\rho L$  can be inferred based on the spectral height in that sub-range as measured by that detector, as is described in **Areal Density and Elastic Scattering** (p. 101) [see Eq. (6)]. This inferred  $\rho L$  can be projected in a ring on a sphere enclosing the target as shown in Fig. 150.57. As a way to combine deuteron and triton elastic scattering, an average value of  $A = 2.5$  can be used when calculating projection angles via Eq. (7). After this is done for each detector and energy sub-range, rings that overlap can be averaged together in the regions of overlap, resulting in a reconstructed areal-density map in  $4\pi$ . Note that this projection assumes that neutrons are produced as a central source that introduces an error in the maps. This error is potentially quantifiable with neutron images that indicate the location of the primary source in the compressed core. Neutron imaging is not possible on OMEGA, however, because of limited neutron statistics; although, as shown below, if the perturbation were of a significantly large wavelength, the inference of areal-density variations would remain robust.

A proof-of-principle test of the reconstruction technique for  $\rho R$  was performed by post-processing a 3-D HYDRA<sup>4</sup> OMEGA cryogenic implosion simulation, including realistic nonuniformity seeds from laser beam imbalances and the offset of the target in the target chamber. Primary D-T neutrons and elastically scattered neutrons were tracked for 20 time slices around peak neutron production. The density profile at peak neutron production shows a dominant  $\ell = 1$  Legendre mode in the compressed core, primarily because the target was not placed at the target chamber center (Fig. 150.64). The lineout of the areal density taken from the location of the peak neutron production is also shown in Fig. 150.64(b). With infinite coverage, the inferred areal densities from the neutron spectrum are shown in Fig. 150.65(a). Since the dominant mode is given by  $\ell = 1$ , the phase is reversed compared to Fig. 150.64(b). Four detectors were arranged in an *ad hoc* tetrahedral fashion around the target in IRIS3D, and the code was used to simulate their observed spectra from 1 to 6 MeV. The locations of these detectors are shown in Fig. 150.65(b). Neutron spectra are used to reconstruct an areal-density map using the procedure described previously. The shape of the reconstructed map compares well to the lineout map seen in Fig. 150.64(b), although the contrast

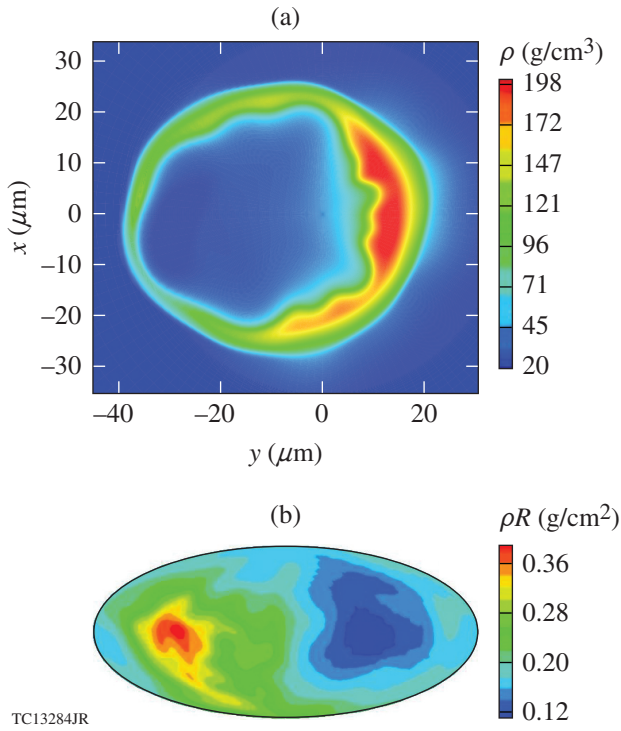


Figure 150.64

(a) Equatorial density cross section of a profile generated by *HYDRA*. An  $\ell = 1$  mode is apparent. (b) Hammer plot of lineout  $\rho R$  of the profile shown in (a), as in Fig. 150.61(a). The  $\ell = 1$  mode is again the dominant feature.

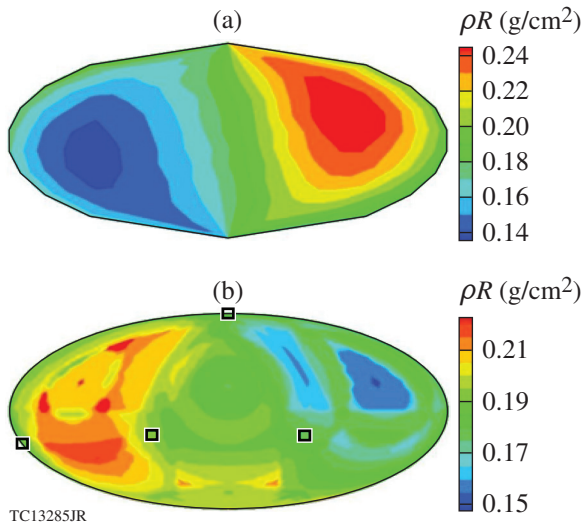


Figure 150.65

(a) Hammer plot of observed  $\rho R$  using the 3.5- to 4.5-MeV range for the profile shown in Fig. 150.64. Note the expected phase change compared to Fig. 150.64(b). (b) Reconstructed  $\rho R$  plot using the method described above with four detectors measuring the 1- to 6-MeV neutron range. The locations of the four detectors are marked with black squares. The spectrum for each detector was split into ten 1-MeV sub-ranges.

is significantly lower, at about  $0.07 \text{ g/cm}^2$ , compared to about  $0.26 \text{ g/cm}^2$  in the lineout or  $\sim 27\%$ . Figure 150.65(a) suggests, however, that even with arbitrarily many detectors viewing the low-energy portion of the spectrum, the maximum-observable contrast is  $\sim 0.10 \text{ g/cm}^2$ . This suggests that if one can account for background, a small number of detectors have the potential to reconstruct accurate areal-density maps of low-mode asymmetries around a target. It should be noted, however, that the success of any application of this method depends greatly on where the detectors happen to be placed relative to whatever asymmetries are present. If, as complementary experiments in room-temperature plastic shell implosions suggest, there is a systematic  $\ell = 1$  mode (Ref. 16), the locations for the new detectors can be optimally prescribed to detect the mode for these cryogenic implosions.

### Ion-Temperature Inference

The width around the primary peak in the neutron spectrum, for D–T and D–D fusion neutrons, depends on target ion temperatures and fluid flow. The variance  $\sigma_n^2$  in energy for a primary spectrum<sup>17</sup> is

$$\sigma_n^2 = \frac{2m_n T_i E_0}{m_n + m_\alpha} + 2m_n E_0 \sigma_v^2, \quad (8)$$

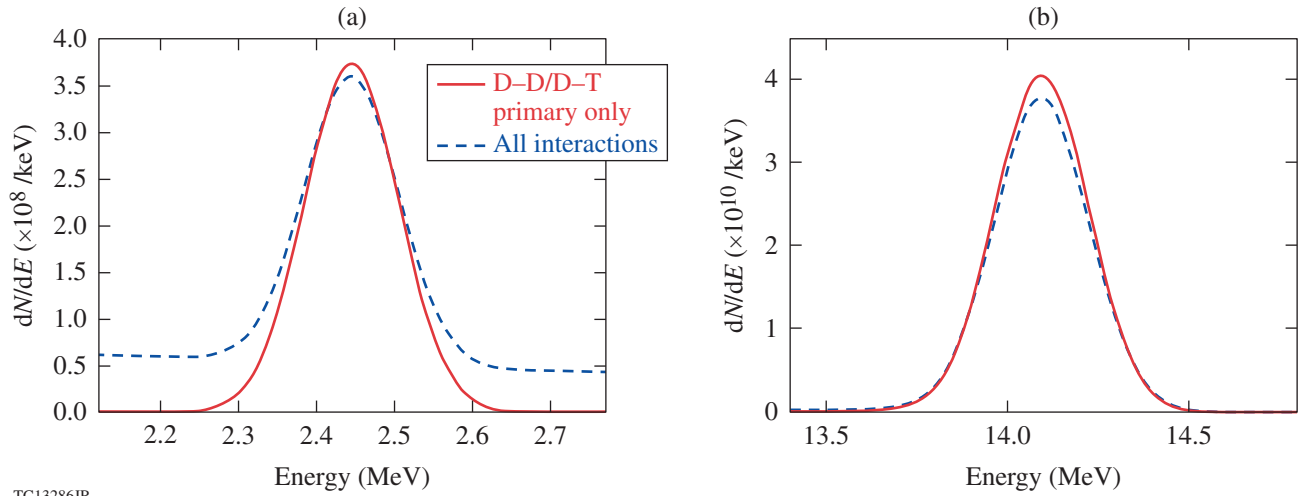
where  $m_n$  is the mass of a neutron,  $E_0$  is the mean energy of the primary neutron (14.1 MeV for D–T primaries and 2.45 MeV for D–D primaries),  $m_\alpha$  is the mass of the non-neutron product ( $^4\text{He}$  for D–T and  $^3\text{He}$  for D–D), and  $\sigma_v^2$  is the variance in the component of the fluid velocity along the direction of the detector; i.e.,

$$\sigma_v^2 = \text{Var}(\vec{v} \cdot \vec{d}). \quad (9)$$

The inferred temperature from the neutron spectrum is given by<sup>18</sup>

$$T_{\text{fit}} = \frac{\Delta E_{\text{fit}}^2}{E_0} \frac{m_n + m_\alpha}{16m_n \log 2}, \quad (10)$$

where  $\Delta E_{\text{fit}}$  is the full width at half maximum (FWHM) of the spectrum. Therefore, the ion temperature can be inferred by measuring the primary neutron spectra. Note that effects such as fluid velocity or background contributions to the neutron spectrum, which widen D–T or D–D primary spectra, will increase the apparent D–T or D–D ion temperatures as seen from that direction (Fig. 150.66 and Table 150.VII). The neutron spectrum around the D–D fusion neutron peak [Fig. 150.66(a)]



TC13286JR

Figure 150.66

(a) Spectra, near the D–D primary peak, generated by *IRIS3D* for the profile shown in Fig. 150.56 with and without other interactions included. Note that fluid flow is not accounted for in either case. (b) Same as (a), but for the D–T primary peak. The D–T and D–D temperatures inferred from each spectrum are shown in Table 150.VII.

Table 150.VII: Ion temperature values inferred from the neutron spectra shown in Fig. 150.66 from D–D and D–T reactions. These values should be compared to a thermal temperature of 3 keV.

Inferred ion temperature (keV)	D–D reaction	D–T reaction
D–T/D–D primaries only	2.97	2.9
All neutron interactions	3.89	3.0

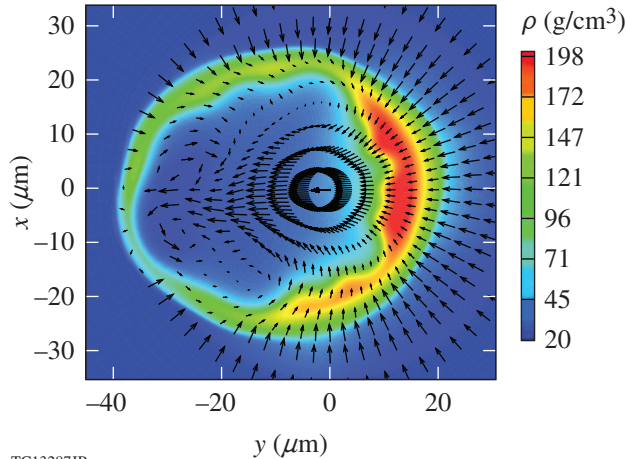
can be broadened because of these effects while only marginally influencing the width of the D–T fusion neutron. The two contributions to the spectra are low-energy backgrounds from other neutron processes in the target and the lowering of the height of the D–D neutron peak because of its higher scattering cross sections, which cause a significant increase in apparent ion temperature (Table 150.VII). The apparent temperature calculated from just the D–D primary spectra is 2.97 keV compared to the thermal value of 3 keV (see Fig. 150.56), while that calculated from the spectra including all contributions without any corrections to the background is 3.89 keV—a 31% increase.

These effects are relatively insignificant when inferred from the D–T neutron spectrum [Fig. 150.66(b)]. This is because (1) the scattering cross sections of 14.1-MeV neutrons are smaller compared to those of 2.45-MeV neutrons and (2) there is a lack of backgrounds above 12 MeV, including all the neutron interactions. As Table 150.VII indicates, the increase is less than 1%.

The second term in Eq. (8), corresponding to fluid flow, can significantly affect neutron spectral widths. To isolate the effect of fluid flow, the same hydrocode profile from Fig. 150.64 was used and only D–T and D–D primaries were tracked. Figure 150.67 shows that the profile contains a jet of fluid flow directed from the high-density region of the  $\ell = 1$  mode to the low-density side.

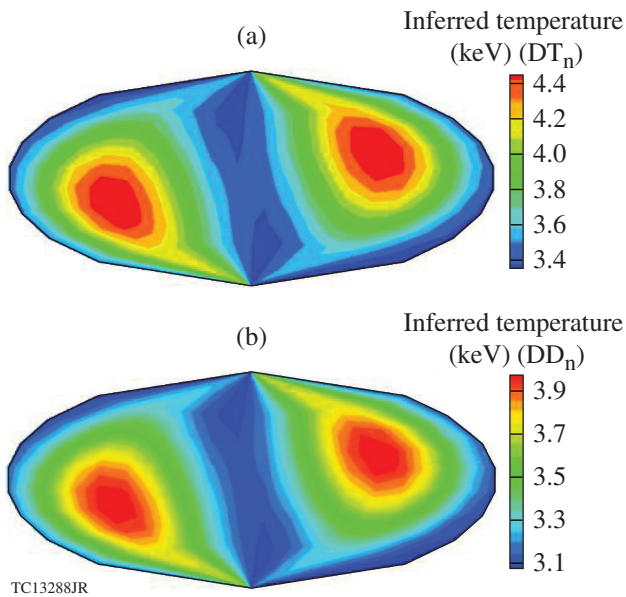
The inferred ion temperatures from D–T and D–D fusion neutron spectra (Fig. 150.68) correspond closely to this flow. Observed temperatures for both D–T and D–D neutrons are highest at the positions corresponding to the extremes in density shown in Fig. 150.64(b) and lowest in a ring at about  $90^\circ$  to these two points. For any direction in the ring around the  $\ell = 1$  mode, the jet seen in Fig. 150.67 points orthogonally to that direction, so it has a very small effect on the value of  $\sigma_v^2$  as seen from that direction as calculated in Eq. (9). For the directions that point along the  $\ell = 1$  mode, however, there is a large variation in  $\vec{v} \cdot \vec{d}$  [Eq. (9)], leading to a large  $\sigma_n^2$  [Eq. (8)]. As

as a result, the apparent temperature is much higher than it would be with no fluid flow in these directions. These results indicate that with multiple views of the primary neutron spectra, the relative ion temperature values inferred can provide an indication of low-order asymmetries in the hot spot.



TC13287JR

Figure 150.67 Same as Fig. 150.64(a), but with additional vectors representing fluid velocity direction and magnitude.



TC13288JR

Figure 150.68 (a) Hammer plot of apparent DT ion temperatures around the target for the profile shown at peak neutron production in Fig. 150.64, as calculated by *IRIS3D* considering DT neutrons only. As in previous figures, each point represents a direction in the target chamber, and the value at each point is the apparent temperature as measured from that direction. (b) Same as (a), but for apparent DD ion temperatures.

## Conclusions

Using a newly developed particle tracking code *IRIS3D* (see **Appendix**, below), neutron-based spectra are used to study signatures of asymmetry in OMEGA-scale cryogenic implosions. These include areal-density variations and neutron spectral-width variations around the compressed target. Background subtraction from observed neutron spectra is extremely important for the lower-energy range (1 to 6 MeV) to infer true areal densities. It is found that because of the finite area of the target viewed by detectors, a limited number of detectors that use a neutron spectrum up to 6 MeV can provide information on the underlying asymmetric structure of the compressed shell. Although not presented in this work, it has been found that the shape of the neutron spectrum changes from the spherically symmetric shape. This information will be used to isolate the effect of asymmetry and backgrounds in future work. Background subtraction from the lower-energy D–D fusion neutron peak is critical for reliably inferring neutron width. It is also shown that measurements of neutron width can be correlated with an overall direction of fluid flow from both DD and DT ion temperatures, provided background correction has been performed for the DD temperature. Detailed simulations and comparisons with experiment for a range of implosion parameters will be presented elsewhere. We will continue to use *IRIS3D* as a postprocessor for 3-D hydrodynamic codes and will pursue detailed comparisons with observations for OMEGA cryogenic implosions.

## ACKNOWLEDGMENT

The authors thank Dr. Ken Anderson for providing the profiles from *HYDRA* simulations used in this article. This material is based upon work supported by the Department of Energy National Nuclear Security Administration under Award Number DE-NA0001944, the University of Rochester, and the New York State Energy Research and Development Authority.

## Appendix: Structure and Methods of *IRIS3D*

*IRIS3D* is a parallel Monte Carlo–based neutron-tracking code with variable particle weights. Neutrons generated by a variety of interactions are tracked through a spherical grid made up of hexahedral cells such as those shown in Fig. 150.69. Note that in Fig. 150.69 and throughout this appendix,  $r$ ,  $\theta$ , and  $\phi$  refer to spherical coordinates with  $\theta$  denoting the polar angle and  $\phi$  denoting the azimuthal angle. Each cell is indexed as described in the figure and is characterized by a DT fuel density, an ion temperature, and a fluid vector velocity. To preserve the hexahedral structure of each cell, *IRIS3D* imposes exclusion zones within a small distance of the origin and within a small angle of each pole that are not occupied by cells. Therefore, each vertex with an  $i$ -index of zero is not at  $r =$

0 but at a very small distance from the origin, and each vertex with a  $j$ -index of zero or the maximum index is not at  $\theta = 0$  or  $\pi$ , respectively, but at 0 plus a small angle and  $\pi$  minus a small angle, respectively. These exclusion zones are small enough that a very limited number of particles can pass through them in a given simulation. They have an insignificant effect on results, and particles that do pass through them are simply propagated across them by a reflection, where they continue on through the remainder of the grid as usual.

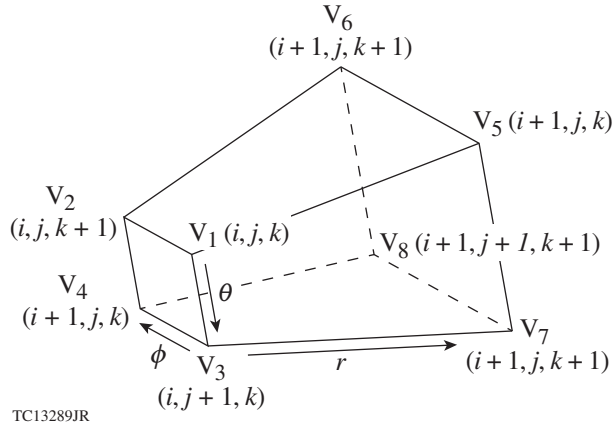


Figure 150.69  
Layout of a generic hexahedral cell in *IRIS3D*. Each vertex ( $V$ ) is represented by indices  $i, j$ , and  $k$ , which increase with  $r, \theta$ , and  $\phi$ , respectively, and each cell is bounded by eight vertices as shown.

*IRIS3D* currently models six neutron-emitting interactions. Spectra from these interactions are shown in Fig. 150.59: primary neutron-producing fusion reactions including  $d(t,n)^4\text{He}$ ,  $d(d,n)^3\text{He}$ , and  $t(t,2n)^4\text{He}$ ; and three secondary interactions including  $d(n,n')d'$ ,  $t(n,n')t'$ , and  $d(n,2n)p$ . The secondary interactions involve the interactions of primaries as they traverse the grid.

A trajectory in *IRIS3D* is generated in some cell,  $(i, j, k)$ , representing some number of neutrons  $y_n$ , all at some energy  $E$ , and moving in some direction  $\vec{d} = (u, v, w)$ , where  $\vec{d}$  is a unit vector and  $u, v$ , and  $w$  are the direction cosines. The initial position of the trajectory,  $P_0 = (x, y, z)$ , is set as the centroid of the cell in which it is generated. The trajectory is tracked in a straight line through the grid.

For each cell the trajectory enters, the following process is carried out: first, initial points  $Q$  and normal vectors for the six planes of the cell are calculated; next, for each plane, the following calculation is performed:

$$\Delta s = \frac{\vec{PQ} \cdot \vec{n}}{\vec{d} \cdot \vec{n}}, \quad (11)$$

where  $P$  denotes the initial position of the trajectory within the cell and  $\Delta s$  represents the (possibly negative) distance the trajectory must travel along its direction to intersect with that plane. The plane that yields the smallest positive value of  $\Delta s$  is the next plane with which the trajectory will intersect, so it corresponds to the face of the cell through which the trajectory will exit. Next, any secondary neutron interactions the user has specified to be considered are calculated based on the physical parameters of the cell and the neutrons represented by the trajectory along with the value of  $\Delta s$  corresponding to the chosen plane. Finally, the trajectory's position  $P$  is changed to the position of intersection with that face and then propagated a small distance along direction  $d$  determined by convergence studies, and the particle's current cell index  $(i, j, k)$  is updated based on the face through which it exited. For example, if the particle started in cell  $(i, j, k)$  and exited through the face lying in the plane  $V_1V_2V_3$ , its new cell index would be  $(i, j, k)$ , as is apparent from Fig. 150.69. If, at this point, the cell indices indicate that the trajectory has entered an exclusion zone, as described above, the particle is appropriately reflected to continue along the grid. For each trajectory, this process is carried out until the particle exits the grid. When this occurs, the trajectory is binned. Note that the target is assumed to be very small compared to the target chamber; therefore, the target is assumed to be essentially point-like from the view of any detectors, so trajectories are binned only according to their direction  $\vec{d}$ .

*IRIS3D* accounts for two different types of detectors that bin trajectories. First, a grid of detectors is placed around the target. The grid lines are at constant  $\theta$  or  $\phi$  values, so for each trajectory, its  $(\theta, \phi)$  direction is calculated according to  $d$ , and it is binned in whichever grid rectangle its  $(\theta, \phi)$  direction lies. In addition, detectors at specific  $(\theta, \phi)$  locations and with specific solid angles  $\Omega$  are specified by the user (for example, these would correspond to existing detector locations on OMEGA). For each of these detectors, a trajectory is binned in them if and only if

$$\vec{d} \cdot \vec{l} \geq 1 - \frac{\Omega}{2\pi}, \quad (12)$$

where  $\vec{l}$  is a unit vector in the direction of the detector. Detectors collect both time-integrated and time-resolved neutron spectra.

In what follows, we discuss in detail how trajectories are launched. First, the number of fusion reactions in each cell is calculated. To do this, a reactivity  $\langle \sigma v \rangle$  is calculated in each

cell based on cell ion temperatures using the analytic fit given in Ref. 19, and then the number of fusion reactions,  $y_{\text{cell}}$ , is calculated as

$$\begin{aligned} y_{\text{cell}} &= \frac{n_i n_j}{1 + \delta_{ij}} \langle \sigma v \rangle_{ij} V \Delta t \\ &= \frac{f_i f_j}{1 + \delta_{ij}} \left( \frac{\rho}{m} \right)^2 \langle \sigma v \rangle_{ij} V \Delta t, \end{aligned} \quad (13)$$

where  $n_i$  and  $n_j$  are ion densities for the two different ions,  $f_i$  and  $f_j$  are the ion fractions for the two ions characterized during the target-fabrication process,  $V$  is the cell volume,  $\Delta t$  is the duration of the time slice being processed for neutron spectra, and  $\delta_{ij}$  is the Kronecker delta ( $= 1$  if  $i = j$ , i.e., for D–D fusion). If  $N$  is the total number of trajectories that are to be launched across the entire grid for that time step (determined by requiring adequate statistics in the calculated spectra), then the number of trajectories launched per cell is  $(y_{\text{cell}} / \sum y_{\text{cell}}) \cdot N$ .

For each primary trajectory to be launched from a cell centroid,  $\vec{d}$  is chosen as a random unit vector (since the primary reactions considered in this work are isotropic) and  $E$  sampled from a normal distribution with mean  $\mu$  and standard deviation  $\sigma$  determined by<sup>17</sup>

$$\mu = E_0 + (\vec{v} \cdot \vec{d}) \sqrt{2 m_n E_0} \quad (14)$$

and

$$\sigma = \sqrt{\frac{2 m_n T_i E_0}{m_n + m_\alpha}}, \quad (15)$$

where, for example,  $E_0 = 14.1$  MeV is the mean neutron energy from the D–T fusion reaction;  $\vec{v}$  the cell fluid velocity;  $m_n$  and  $m_\alpha$  are the masses of the neutron and alpha particles, respectively; and  $T_i$  is the cell ion temperature. The second term in the expression for the mean of the energy distribution takes into account Doppler shifts in the energy of the neutron caused by the fluid velocity. The expression for the standard deviation takes into account the broadening of the neutron spectrum caused by the plasma temperature.<sup>18</sup>

T–T reactions are treated similarly. Reactivity for temperatures below 1 keV is calculated using the analytic fit given in Ref. 20, while reactivity for ion temperatures above or equal to 1 keV is calculated by linear interpolation using the look-up table given in Ref. 21. The initial neutron energy  $E_0$  is sampled

from a distribution obtained by an  $R$ -matrix calculation,<sup>22</sup> which agrees well with experimental measurements.<sup>22</sup> Note that the T–T primary neutrons are not launched in pairs that obey the conservation laws but instead are launched one at a time, independently. Momentum and energy are conserved only with adequate statistics.

Secondary reactions are considered next. *IRIS3D* starts by estimating a value of  $y'$ , the total number of deuteron-scattered neutrons:

$$y' = y_{\text{total}} \frac{f_D \sigma_{14.1}}{\bar{m}} \rho R, \quad (16)$$

where  $y_{\text{total}}$  is the total number of primary neutrons generated ( $= \sum y_{\text{cell}}$ ),  $\sigma_{14.1}$  is the cross section for deuteron elastic scattering for neutrons at 14.1 MeV, and  $\rho R$  is a directionally averaged lineout of the areal density. For multiple scattering, where energies other than 14.1 MeV can contribute to the spectrum, the scattering cross section is obtained from an energy-dependent look-up table given by Ref. 23. The number  $N_s$  of secondary trajectories launched from a given interaction location is a code input to obtain converged results; therefore the weight of each trajectory is  $y_0 = y'_{\text{total}} / N_s$ .

The number of deuteron (or triton)-scattering interactions,  $y'$ , is calculated as

$$y' = y \frac{f_{D/T} \sigma_{D/T}}{\bar{m}} \rho \Delta s, \quad (17)$$

where  $y$  is the number of neutrons represented by the trajectory,  $\sigma$  is the cross section for deuteron elastic scattering for neutrons with energy  $E$ , and  $\Delta s$  is the path length. At this point,  $y$  is replaced with  $y - y'$  since the primary trajectory loses any neutrons that scatter away. The weight of the trajectory is  $y_0$ , and a scattering angle  $\theta$  is sampled by interpolating between a set of energy-dependent angular cross sections from Ref. 15. An azimuthal scattering angle  $\phi$  is then picked randomly over the interval  $(0, 2\pi)$ , and the scattered neutron trajectory direction  $\vec{d}'$  is set as

$$\vec{d}' = \vec{a} \sin\theta \cos\phi + \vec{b} \sin\theta \sin\phi + \vec{d} \cos\theta, \quad (18)$$

where  $\vec{d}$  is the direction of the original trajectory and  $\vec{a}$  and  $\vec{b}$  are a set of unit vectors that are orthogonal to each other and to  $\vec{d}$ . Finally,  $E'$ , the energy of the scattered neutrons, is determined based on  $\theta$  using Eq. (7). Once generated, the scattered trajectory is again handled as described previously.

The deuteron-breakup interaction is modeled somewhat differently. A look-up table for angular distributions of emerging particles is available only for 14.1-MeV incident neutrons, so the interaction is considered only in the case where the original trajectory represents D–T primary neutrons. A constant value of  $\sigma = \sigma_{14.1} = 164.821$  mb is used for both Eqs. (16) and (17) (see Ref. 24). Two trajectories are launched for the product neutrons since two neutrons are produced in each break-up reaction. Since there is no deterministic relationship between the angle and energy of each emergent neutron, the scattering angle is sampled from a distribution calculated based on Ref. 25, and energy is sampled from a distribution based on that scattering angle. As was the case with the T–T primary reaction, the neutrons’ energies and scattering angles are both sampled independently, so momentum and energy are not necessarily conserved in any particular interaction but conservation improves with increasingly better statistics.

If a series of time slices from the same implosion are used instead, the process is repeated for each time step and the results are accumulated over time.

## REFERENCES

1. J. Nuckolls *et al.*, *Nature* **239**, 139 (1972).
2. T. R. Boehly, D. L. Brown, R. S. Craxton, R. L. Keck, J. P. Knauer, J. H. Kelly, T. J. Kessler, S. A. Kumpan, S. J. Loucks, S. A. Letzring, F. J. Marshall, R. L. McCrory, S. F. B. Morse, W. Seka, J. M. Soures, and C. P. Verdon, *Opt. Commun.* **133**, 495 (1997).
3. J. Delettrez, R. Epstein, M. C. Richardson, P. A. Jaanimagi, and B. L. Henke, *Phys. Rev. A* **36**, 3926 (1987).
4. M. M. Marinak *et al.*, *Phys. Plasmas* **8**, 2275 (2001).
5. Lord Rayleigh, *Proc. London Math Soc.* **XIV**, 170 (1883); G. Taylor, *Proc. R. Soc. London Ser. A* **201**, 192 (1950); R. Kishony and D. Shvarts, *Phys. Plasmas* **8**, 4925 (2001).
6. C. Stoeckl, R. Epstein, R. Betti, W. Bittle, J. A. Delettrez, C. J. Forrest, V. Yu. Glebov, V. N. Goncharov, D. R. Harding, I. V. Igumenshchev, D. W. Jacobs-Perkins, R. T. Janezic, J. H. Kelly, T. Z. Kosc, R. L. McCrory, D. T. Michel, C. Mileham, P. W. McKenty, F. J. Marshall, S. F. B. Morse, S. P. Regan, P. B. Radha, B. S. Rice, T. C. Sangster, M. J. Shoup III, W. T. Shmayda, C. Sorce, W. Theobald, J. Ulreich, M. D. Wittman, D. D. Meyerhofer, J. A. Frenje, M. Gatu Johnson, and R. D. Petrasso, *Phys. Plasmas* **24**, 056304 (2017).
7. F. J. Marshall, V. N. Goncharov, V. Yu. Glebov, B. Peng, S. P. Regan, T. C. Sangster, and C. Stoeckl, “A Framed, 16-Image Kirkpatrick–Baez X-Ray Microscope,” submitted to *Review of Scientific Instruments*.
8. R. Betti, P. Y. Chang, B. K. Spears, K. S. Anderson, J. Edwards, M. Fatenejad, J. D. Lindl, R. L. McCrory, R. Nora, and D. Shvarts, *Phys. Plasmas* **17**, 058102 (2010).
9. D. C. Wilson *et al.*, *Nucl. Instrum. Methods Phys. Res. A* **488**, 400 (2002).
10. J. A. Frenje, D. T. Casey, C. K. Li, J. R. Rygg, F. H. Séguin, R. D. Petrasso, V. Yu. Glebov, D. D. Meyerhofer, T. C. Sangster, S. Hatchett, S. Haan, C. Cerjan, O. Landen, M. Moran, P. Song, D. C. Wilson, and R. J. Leeper, *Rev. Sci. Instrum.* **79**, 10E502 (2008).
11. C. J. Forrest, P. B. Radha, V. Yu. Glebov, V. N. Goncharov, J. P. Knauer, A. Pruyne, M. Romanofsky, T. C. Sangster, M. J. Shoup III, C. Stoeckl, D. T. Casey, M. Gatu-Johnson, and S. Gardner, *Rev. Sci. Instrum.* **83**, 10D919 (2012).
12. T. J. Murphy, *Phys. Plasmas* **21**, 072701 (2014).
13. ENDF/B-N1.1, IAEA Nuclear Data Services.
14. S. Skupsky and S. Kacenjari, *J. Appl. Phys.* **52**, 2608 (1981).
15. J. A. Frenje, C. K. Li, F. H. Séguin, D. T. Casey, R. D. Petrasso, D. P. McNabb, P. Navratil, S. Quaglioni, T. C. Sangster, V. Yu. Glebov, and D. D. Meyerhofer, *Phys. Rev. Lett.* **107**, 122502 (2011).
16. C. K. Li, F. H. Séguin, D. G. Hicks, J. A. Frenje, K. M. Green, S. Kurebayashi, R. D. Petrasso, D. D. Meyerhofer, J. M. Soures, V. Yu. Glebov, R. L. Keck, P. B. Radha, S. Roberts, W. Seka, S. Skupsky, C. Stoeckl, and T. C. Sangster, *Phys. Plasmas* **8**, 4902 (2001).
17. V. N. Goncharov, T. C. Sangster, R. Betti, T. R. Boehly, M. J. Bonino, T. J. B. Collins, R. S. Craxton, J. A. Delettrez, D. H. Edgell, R. Epstein, R. K. Follet, C. J. Forrest, D. H. Froula, V. Yu. Glebov, D. R. Harding, R. J. Henchen, S. X. Hu, I. V. Igumenshchev, R. Janezic, J. H. Kelly, T. J. Kessler, T. Z. Kosc, S. J. Loucks, J. A. Marozas, F. J. Marshall, A. V. Maximov, R. L. McCrory, P. W. McKenty, D. D. Meyerhofer, D. T. Michel, J. F. Myatt, R. Nora, P. B. Radha, S. P. Regan, W. Seka, W. T. Shmayda, R. W. Short, A. Shvydky, S. Skupsky, C. Stoeckl, B. Yaakobi, J. A. Frenje, M. Gatu-Johnson, R. D. Petrasso, and D. T. Casey, *Phys. Plasmas* **21**, 056315 (2014).
18. H. Brysk, *Plasma Phys.* **15**, 611 (1973).
19. H. S. Bosch and G. M. Hale, *Nucl. Fusion* **32**, 611 (1992); **33**, 1919(E) (1993).
20. A. Peres, *J. Appl. Phys.* **50**, 5569 (1979).
21. J. R. McNally, Jr., K. E. Rothe, and R. D. Sharp, Oak Ridge National Laboratory, Oak Ridge, TN, Report ORNL/TM-6914 (1979).
22. D. B. Sayre, C. R. Brune, J. A. Caggiano, V. Y. Glebov, R. Hatarik, A. D. Bacher, D. L. Bleuel, D. T. Casey, C. J. Cerjan, M. J. Eckart, R. J. Fortner, J. A. Frenje, S. Friedrich, M. Gatu-Johnson, G. P. Grim, C. Hagmann, J. P. Knauer, J. L. Kline, D. P. McNabb, J. M. McNaney, J. M. Mintz, M. J. Moran, A. Nikroo, T. Phillips, J. E. Pino, B. A. Remington, D. P. Rowley, D. H. Schneider, V. A. Smalyuk, W. Stoeffl, R. E. Tipton, S. V. Weber, and C. B. Yeaman, *Phys. Rev. Lett.* **111**, 052501 (2013).
23. R. C. Shah, B. M. Haines, F. J. Wysocki, J. F. Benage, J. A. Fooks, V. Glebov, P. Hakel, M. Hoppe, I. V. Igumenshchev, G. Kagan, R. C. Mancini, F. J. Marshall, D. T. Michel, T. J. Murphy, M. E. Schoff, K. Silverstein, C. Stoeckl, and B. Yaakobi, *Phys. Rev. Lett.* **118**, 135001 (2017).
24. P. G. Young, G. M. Hale, and M. G. Chadwick, ENDF/B-VII.1, IAEA Nuclear Data Services, 22 December 2011.
25. A. Deltuva, Institute of Theoretical Physics and Astronomy, Vilnius University, Vilnius, Lithuania, private communication (2016).



---

## Publications and Conference Presentations

---

### Publications

---

- B. P. Chock, D. R. Harding, and T. B. Jones, “Dispensing Surfactant-Containing Water Droplets Using Electrowetting,” in the *2016 AIChE Meeting Proceedings* (American Institute of Chemical Engineers, New York, 2016), Paper 560d/461784.
- C. Dorrer, W. A. Bittle, R. Cuffney, M. Spilatro, E. M. Hill, T. Z. Kosc, J. H. Kelly, and J. D. Zuegel, “Characterization and Optimization of an Eight-Channel Time-Multiplexed Pulse Shaping System,” *J. Lightwave Technol.* **35**, 173 (2017).
- C. Dorrer and J. Hassett, “Model-Based Optimization of Near-Field Binary-Pixelated Beam Shapers,” *Appl. Opt.* **56**, 806 (2017).
- R. Epstein, S. P. Regan, B. A. Hammel, L. J. Suter, H. A. Scott, M. A. Barrios, D. K. Bradley, D. A. Callahan, C. Cerjan, G. W. Collins, S. N. Dixit, T. Döppner, M. J. Edwards, D. R. Farley, K. B. Fournier, S. Glenn, S. H. Glenzer, I. E. Golovkin, A. Hamza, D. G. Hicks, N. Izumi, O. S. Jones, M. H. Key, J. D. Kilkenny, J. L. Kline, G. A. Kyrala, O. L. Landen, T. Ma, J. J. MacFarlane, A. J. Mackinnon, R. C. Mancini, R. L. McCrory, D. D. Meyerhofer, N. B. Meezan, A. Nikroo, H.-S. Park, P. K. Patel, J. E. Ralph, B. A. Remington, T. C. Sangster, V. A. Smalyuk, P. T. Springer, R. P. J. Town, and J. L. Tucker, “Applications and Results of X-Ray Spectroscopy in Implosion Experiments at the National Ignition Facility,” *AIP Conf. Proc.* **1811**, 190004 (2017).
- J. R. Fein, J. P. Holloway, M. R. Trantham, P. A. Keiter, D. H. Edgell, D. H. Froula, D. Haberberger, Y. Frank, M. Fraenkel, E. Raicher, D. Shvarts, and R. P. Drake, “Mitigation of Hot Electrons from Laser-Plasma Instabilities in High-Z, Highly Ionized Plasmas,” *Phys. Plasmas* **24**, 032707 (2017).
- C. J. Forrest, P. B. Radha, J. P. Knauer, V. Yu. Glebov, V. N. Goncharov, S. P. Regan, M. J. Rosenberg, T. C. Sangster, W. T. Shmayda, C. Stoeckl, and M. Gatu Johnson, “First Measurements of Deuterium–Tritium and Deuterium–Deuterium Fusion-Reaction Yields in Ignition-Scalable Direct-Drive Implosions,” *Phys. Rev. Lett.* **118**, 095002 (2017).
- M. Gatu Johnson, A. B. Zylstra, A. Bacher, C. R. Brune, D. T. Casey, C. Forrest, H. W. Herrmann, M. Hohenberger, D. B. Sayre, R. M. Bionta, J.-L. Bourgade, J. A. Caggiano, C. Cerjan, R. S. Craxton, D. Dearborn, M. Farrell, J. A. Frenje, E. M. Garcia, V. Yu. Glebov, G. Hale, E. P. Hartouni, R. Hatarik, M. Hohensee, D. M. Holunga, M. Hoppe, R. Janezic, S. F. Khan, J. D. Kilkenny, Y. H. Kim, J. P. Knauer, T. R. Kohut, B. Lahmann, O. Landoas, C. K. Li, F. J. Marshall, L. Masse, A. McEvoy, P. McKenty, D. P. McNabb, A. Nikroo, T. G. Parham, M. Paris, R. D. Petrasso, J. Pino, P. B. Radha, B. Remington, H. G. Rinderknecht, H. Robey, M. J. Rosenberg, B. Rosse, M. Rubery, T. C. Sangster, J. Sanchez, M. Schmitt, M. Schoff, F. H. Séguin, W. Seka, H. Sio, C. Stoeckl, and R. E. Tipton, “Development of an Inertial Confinement Fusion Platform to Study Charged-Particle-Producing Nuclear Reactions Relevant to Nuclear Astrophysics,” *Phys. Plasmas* **24**, 041407 (2017).
- R. F. Heeter, J. E. Bailey, R. S. Craxton, B. G. DeVolder, E. S. Dodd, E. M. Garcia, E. J. Huffman, C. A. Iglesias, J. A. King, J. L. Kline, D. A. Liedahl, P. W. McKenty, Y. P. Opachich, G. A. Rochau, P. W. Ross, M. B. Schneider, M. E. Sherrill, B. G. Wilson, R. Zhang, and T. S. Perry, “Conceptual Design of Initial Opacity Experiments on the National Ignition Facility,” *J. Plasma Phys.* **83**, 595830103 (2017).
- I. V. Igumenshchev, D. T. Michel, R. C. Shah, E. M. Campbell, R. Epstein, C. J. Forrest, V. Yu. Glebov, V. N. Goncharov, J. P. Knauer, F. J. Marshall, R. L. McCrory, S. P. Regan, T. C. Sangster, C. Stoeckl, A. J. Schmitt, and S. Obenschain, “Three-Dimensional Hydrodynamic Simulations of OMEGA Implosions,” *Phys. Plasmas* **24**, 056307 (2017) (invited).
- J. Li, S. X. Hu, and C. Ren, “Effects of Laser–Plasma Instabilities on Hydro Evolution in an OMEGA-EP Long-Scale-Length Experiment,” *Phys. Plasmas* **24**, 022706 (2017).
- K. Mehrotra, B. N. Taylor, A. A. Kozlov, S. Papernov, and J. C. Lambropoulos, “Nano-Indentation and Laser-Induced Damage Testing in Optical Multilayer-Dielectric Gratings,” *Appl. Opt.* **56**, 2494 (2017).

J. B. Oliver, "Impact of Non-Integer Planetary Revolutions on the Distribution of Evaporated Optical Coatings," *Appl. Opt.* **56**, 1460 (2017).

C. Stoeckl, R. Epstein, R. Betti, W. Bittle, J. A. Delettrez, C. J. Forrest, V. Yu. Glebov, V. N. Goncharov, D. R. Harding, I. V. Igumenshchev, D. W. Jacobs-Perkins, R. T. Janezic, J. H. Kelly, T. Z. Kosc, R. L. McCrory, D. T. Michel, C. Mileham, P. W. McKenty, F. J. Marshall, S. F. B. Morse, S. P. Regan, P. B. Radha, B. Rice, T. C. Sangster, M. J. Shoup III, W. T.

Shmayda, C. Sorce, W. Theobald, J. Ulreich, M. D. Wittman, D. D. Meyerhofer, J. A. Frenje, M. Gatu Johnson, and R. D. Petrasso, "Monochromatic Backlighting of Direct-Drive Cryogenic DT Implosions on OMEGA," *Phys. Plasmas* **24**, 056304 (2017) (invited).

D. Turnbull, C. Goyon, G. E. Kemp, B. B. Pollock, D. Mariscal, L. Divol, J. S. Ross, S. Patankar, J. D. Moody, and P. Michel, "Refractive Index Seen by a Probe Beam Interacting with a Laser-Plasma System," *Phys. Rev. Lett.* **118**, 015001 (2017).

### Forthcoming Publications

D. H. Barnak, J. R. Davies, R. Betti, M. J. Bonino, E. M. Campbell, V. Yu. Glebov, D. R. Harding, J. P. Knauer, S. P. Regan, A. B. Sefkow, A. J. Harvey-Thompson, K. J. Peterson, D. B. Sinars, S. A. Slutz, M. R. Weis, and P.-Y. Chang, "Laser-Driven Magnetized Liner Inertial Fusion on OMEGA," to be published in *Physics of Plasmas* (invited).

E. M. Campbell, V. N. Goncharov, T. C. Sangster, S. P. Regan, P. B. Radha, R. Betti, J. F. Myatt, D. H. Froula, M. J. Rosenberg, I. V. Igumenshchev, W. Seka, A. A. Solodov, A. V. Maximov, J. A. Marozas, T. J. B. Collins, D. P. Turnbull, F. J. Marshall, A. Shvydky, J. P. Knauer, R. L. McCrory, A. B. Sefkow, M. Hohenberger, P. A. Michel, T. Chapman, L. Masse, C. Goyon, S. Ross, J. W. Bates, M. Karasik, J. Oh, J. Weaver, A. J. Schmitt, K. Obenschain, S. P. Obenschain, S. Reyes, and B. Van Wonterghem, "Laser-Direct-Drive Program: Promise, Challenge, and Path Forward," to be published in *Matter and Radiation at Extremes*.

J. R. Davies, D. H. Barnak, R. Betti, E. M. Campbell, P.-Y. Chang, K. J. Peterson, A. B. Sefkow, D. B. Sinars, and M. R. Weis, "Laser-Driven Magnetized Liner Inertial Fusion," to be published in *Physics of Plasmas*.

R. Epstein, C. Stoeckl, V. N. Goncharov, P. W. McKenty, F. J. Marshall, S. P. Regan, R. Betti, W. A. Bittle, D. R. Harding, S. X. Hu, I. V. Igumenshchev, D. W. Jacobs-Perkins, R. T. Janezic, J. H. Kelly, T. Z. Kosc, C. Mileham, S. F. B. Morse, P. B. Radha, B. S. Rice, T. C. Sangster, M. J. Shoup III, W. T. Shmayda, C. Sorce, J. Ulreich, and M. D. Wittman, "Simulation and Analysis of Time-Gated Monochromatic Radiographs of Cryogenic Implosions on OMEGA," to be published in *High Energy Density Physics*.

C. Fagan, M. Sharpe, W. T. Shmayda, and W. U. Schröder, "The Impact of Acid Treatments and Electropolishing Stainless-Steel Surfaces on Tritium Inventories," to be published in *Fusion Science and Technology*.

M. C. Gregor, D. E. Fratanduono, C. A. McCoy, D. N. Polsin, T. Braun, P. M. Celliers, J. H. Eggert, J. R. Rygg, G. W. Collins, D. D. Meyerhofer, and T. R. Boehly, "Hugoniot and Release Measurements in Diamond Shocked up to 25 Mbar," to be published in *Physical Review B*.

S. X. Hu, R. Gao, Y. Ding, L. A. Collins, and J. D. Kress, "First-Principles Equation-of-State Table of Silicon and Its Effects on High-Energy-Density Plasma Simulations," to be published in *Physical Review E*.

D. T. Michel, S. X. Hu, A. K. Davis, V. Yu. Glebov, V. N. Goncharov, I. V. Igumenshchev, P. B. Radha, C. Stoeckl, and D. H. Froula, "Measurement of the Shell Decompression in Direct-Drive Inertial-Confinement-Fusion Implosions," to be published in *Physical Review E*.

J. F. Myatt, R. K. Follett, J. G. Shaw, D. H. Edgell, D. H. Froula, I. V. Igumenshchev, and V. N. Goncharov, "A Wave-Based Model for Cross-Beam Energy Transfer in Direct-Drive Inertial Confinement Fusion," to be published in *Physics of Plasmas* (invited).

T. Petersen, J. Bromage, and J. D. Zuegel, "High-Average-Power, 2- $\mu$ m Femtosecond Optical Parametric Oscillator Synchronously Pumped by a Thin-Disk, Mode-Locked Laser," to be published in *Optics Express*.

B. S. Rice, J. Ulreich, C. Fella, J. Crippen, P. Fitzsimmons, and A. Nikroo, "Permeation Fill-Tube Design for Inertial Confinement Fusion Target Capsules," to be published in *High Power Laser Science and Engineering*.

J. Serafini, A. Hossain, R. B. James, M. Guziewicz, A. Kruszka, W. Słysz, and R. Sobolewski, "Photoconductive and Electro-Optic Effects in (Cd,Mg)Te Single Crystals Measured in an Experiment-on-Chip Configuration," to be published in *Applied Physics Letters*.

P. Tzeferacos, A. Rigby, A. Bott, A. R. Bell, R. Bingham, A. Casner, F. Cattaneo, E. M. Churazov, J. Emig, N. Flocke, F. Fiuza, C. B. Forest, J. Foster, C. Graziani, J. Katz, M. Koenig, C.-K. Li, J. Meinecke, R. Petrasso, H.-S. Park, B. A. Remington, J. S. Ross, D. Ryu, D. Ryutov, K. Weide, T. G. White, B. Reville, F. Miniati, A. A. Schekochihin, D. H. Froula, G. Gregori, and D. Q. Lamb, "Numerical Modeling of Laser-Driven Experiments Aiming to Demonstrate Magnetic Field Amplification via Turbulent Dynamo," to be published in *Physics of Plasmas*.

---

### Conference Presentations

---

S. G. Demos and R. W. Wood, "Simultaneous White-Light and Protoporphyrin-IX Fluorescence Imaging for Optimized Cystoscopic Detection of Non-Muscle-Invasive Bladder Cancer," SPIE Photonics West, San Francisco, CA, 28 January–2 February 2017.

The following presentations were made at the NIF and JLF User Group Meeting, Livermore, CA, 6–8 February 2017:

L. A. Ceurvorst, N. Ratan, M. F. Kasim, J. Sadler, P. A. Norreys, H. Habara, K. A. Tanaka, S. Zhang, M. S. Wei, S. Ivancic, D. H. Froula, and W. Theobald, "Channeling Optimization of High-Intensity Laser Beams in Millimeter-Scale Plasmas."

M. J. Rosenberg, A. A. Solodov, W. Seka, J. F. Myatt, S. P. Regan, M. Hohenberger, A. V. Maximov, T. J. B. Collins, V. N. Goncharov, R. Epstein, R. W. Short, D. P. Turnbull, D. H. Froula, P. B. Radha, P. Michel, T. Chapman, J. D. Moody, L. Masse, C. Goyon, J. E. Ralph, M. A. Barrios, J. W. Bates, and A. J. Schmitt, "Planar Laser-Plasma Interaction Experiments at Direct-Drive Ignition-Relevant Scale Lengths at the National Ignition Facility."

D. Turnbull, P. Michel, C. Goyon, G. E. Kemp, B. B. Pollock, T. Chapman, D. Mariscal, L. Divol, J. S. Ross, S. Patankar, J. D. Moody, D. H. Froula, D. H. Edgell, R. K. Follett, J. F. Myatt, and E. M. Campbell, "Refractive Index Seen by a Probe Beam Interacting with a Laser-Plasma System."

The following presentations were made at the IAEC–NNSA Meeting on Hydrodynamic Instabilities in HED Systems, Livermore, CA, 8–10 February 2017:

R. Betti, "Deceleration Phase Hydrodynamic Instabilities, Pressure Degradation from Low to High (Mid) Modes."

R. Betti, D. Barnak, J. Davies, M. J. Bonino, V. Glebov, and M. Campbell, "Magnetized Liner Inertial Fusion."

A. Shvydky, M. Hohenberger, P. B. Radha, M. J. Rosenberg, K. S. Anderson, V. N. Goncharov, J. A. Marozas, F. J. Marshall, P. W. McKenty, S. P. Regan, T. C. Sangster, J. M. DiNicola, J. M. Koning, M. M. Marinak, and L. Masse, "Hydrodynamic Instability Growth and Imprint Experiments at the National Ignition Facility."

D. R. Harding, B. P. Chock, N. D. Viza, T. B. Jones, Z. Bei, W. Wang, and M. Moynihan, "Next-Generation Lab-on-Chip Methods for Making Plastic Targets for Inertial Confinement Fusion Experiments," NNSA Technical Seminars, Washington, DC, 14 February 2017.

J. F. Myatt, "The Laser-Plasma Simulation Environment (*LPSE*): A Flexible Tool for the ICF and HEDP Communities," NNSA Technical Seminars, Washington, DC, 28 February 2017.

The following presentations were made at the 22nd Target Fabrication Meeting, Las Vegas, NV, 12–16 March 2017:

M. J. Bonino, M. D. Wittman, D. R. Harding, N. Satoh, and M. Takagi, “Characterization of Polystyrene Shells.”

B. P. Chock, D. R. Harding, and T. B. Jones, “Extending the Digital Microfluidics Process to Form Emulsions Using Low-Surface-Energy Fluids.”

J. M. García Figueroa and D. R. Harding, “Effect of High Ion and Electron Densities, and Substrate Temperature on the Properties of Glow-Discharge Polymer Films.”

D. R. Harding, J. Ulreich, R. Chapman, M. D. Wittman, R. Taylor, C. Taylor, M. J. Bonino, R. Q. Gram, and N. P. Redden, “Improvements to the Target and Cryogenic Equipment to Increase the Hot-Spot Pressure in Implosions on OMEGA.”

N. P. Redden, W. T. Shmayda, M. D. Wittman, J. L. Reid, R. F. Earley, J. Magoon, K. Heung, S. Xiao, T. Sessions, and S. Redd, “The Laboratory for Laser Energetics’ Hydrogen Isotope Separation System.”

S. P. Regan, V. N. Goncharov, T. C. Sangster, E. M. Campbell, R. Betti, T. Bernat, A. Bose, T. R. Boehly, M. J. Bonino, D. Cao, R. Chapman, T. J. B. Collins, R. S. Craxton, A. K. Davis, J. A. Delettrez, D. H. Edgell, R. Epstein, M. Farrell, C. J. Forrest, J. A. Frenje, D. H. Froula, M. Gatu Johnson, C. Gibson, V. Yu. Glebov, A. Greenwood, D. R. Harding, M. Hohenberger, S. X. Hu, H. Huang, J. Hund, I. V. Igumenshchev, D. W. Jacobs-Perkins, R. T. Janezic, M. Karasik, R. L. Keck, J. H. Kelly, T. J. Kessler, J. P. Knauer, T. Z. Kosci, S. J. Loucks, J. A. Marozas, F. J. Marshall, R. L. McCrory, P. W. McKenty, D. D. Meyerhofer, D. T. Michel, J. F. Myatt, S. P. Obenshain, R. D. Petrasso, N. Petta, P. B. Radha, M. J. Rosenberg, A. J. Schmitt, M. J. Schmitt, M. Schoff, W. Seka, W. T. Shmayda, M. J. Shoup III, A. Shvydky, A. A. Solodov, C. Stoeckl, W. Sweet, C. Taylor, R. Taylor, W. Theobald, J. Ulreich, M. D. Wittman, K. M. Woo, and J. D. Zuegel, “The National Direct-Drive Program: OMEGA to the National Ignition Facility.”

N. D. Viza and D. R. Harding, “Performance of Different ‘Lab-on-Chip’ Geometries for Making Double Emulsions for Polystyrene Shells.”

M. D. Wittman, M. J. Bonino, C. Fella, and D. R. Harding, “Effect of Tritium-Induced Damage to Plastic Targets from High-Density D-T Permeation.”

D. N. Polsin, T. R. Boehly, J. A. Delettrez, G. W. Collins, J. R. Rygg, M. C. Gregor, B. J. Henderson, C. A. McCoy, D. E. Fratanduono, R. F. Smith, R. G. Kraus, J. H. Eggert, F. Coppari, A. Jenei, D. C. Swift, and P. M. Celliers, “The First Observation of the bcc Phase in Compressed Aluminum,” March APS Annual Meeting, New Orleans, LA, 13–17 March 2017.

The following presentations were made at the 13th Direct Drive and Fast Ignition Workshop, Salamanca, Spain, 22–24 March 2017:

S. P. Regan, V. N. Goncharov, T. C. Sangster, E. M. Campbell, R. Betti, T. Bernat, A. Bose, T. R. Boehly, M. J. Bonino, D. Cao, R. Chapman, T. J. B. Collins, R. S. Craxton, A. K. Davis, J. A. Delettrez, D. H. Edgell, R. Epstein, M. Farrell, C. J. Forrest, J. A. Frenje, D. H. Froula, M. Gatu Johnson, C. Gibson, V. Yu. Glebov, A. Greenwood, D. R. Harding, M. Hohenberger, S. X. Hu, H. Huang, J. Hund, I. V. Igumenshchev, D. W. Jacobs-Perkins, R. T. Janezic, M. Karasik, R. L. Keck, J. H. Kelly, T. J. Kessler, J. P. Knauer, T. Z. Kosci, S. J. Loucks, J. A. Marozas, F. J. Marshall, R. L. McCrory, P. W. McKenty, D. D. Meyerhofer, D. T. Michel, J. F. Myatt, S. P. Obenshain, R. D. Petrasso, N. Petta, P. B. Radha, M. J. Rosenberg, A. J. Schmitt, M. J. Schmitt, M. Schoff, W. Seka, W. T. Shmayda, M. J. Shoup III, A. Shvydky, A. A. Solodov, C. Stoeckl, W. Sweet, C. Taylor, R. Taylor, W. Theobald, J. Ulreich, M. D. Wittman, K. M. Woo, and J. D. Zuegel, “The National Direct-Drive Program: OMEGA to the National Ignition Facility.”

M. J. Rosenberg, A. A. Solodov, W. Seka, J. F. Myatt, S. P. Regan, A. V. Maximov, R. Epstein, T. J. B. Collins, V. N. Goncharov, R. W. Short, D. P. Turnbull, D. H. Froula, P. B. Radha, R. K. Follett, P. A. Michel, M. Hohenberger, T. Chapman, J. D. Moody, L. Masse, C. Goyon, M. A. Barrios, J. W. Bates, A. J. Schmitt, “Planar Laser-Plasma Interaction Experiments at Direct-Drive Ignition-Relevant Scale Lengths at the National Ignition Facility.”



